University of Bergen

Department of Chemistry

Masters Thesis

Investigating Ice Formation with NMR and Contact Angle Goniometry

Author: Anita Isabell Lien
Supervisor: Bodil Holst
Co-supervisor: Willy Nerdal, John Georg Seland and Espen Werdal Selfors

September 15, 2022

Abstract

Ice formation on surfaces imposes numerous challenges in the industry and everyday life, ranging from icy windshields to airplanes needing de-icing before take-off. Today, the main methods to mitigate these issues revolve around removing already formed surface ice, using heating, chemicals, mechanical removal or a combination of these. However, these methods are often costly, energy-consuming and hazardous. Thus, this has become a growing field of interest in science, with numerous studies on potential anti-icing surfaces and coatings.

However, ice formation is a complex phenomenon still not fully understood and with no complete theory to predict ice formation on different surfaces. The most commonly used theory, the classical nucleation theory (CNT), fails to predict the ice nucleation in some cases, especially concerning textured surfaces. Hence, a modified nucleation theory has been proposed in recent studies, in which the existence of a quasi-liquid layer (QLL) in the ice embryo-surface interface might explain deviations from the CNT.

The aim of this thesis is thus to investigate and increase our understanding of ice formation on sapphire surfaces with the basis of the newly proposed modified nucleation theory. Sapphire has been chosen for its excellent durability and usability in optical applications and lenses, making it a relevant material for the fluorinated graphene coating under development at UiB. Two different surface finishes are investigated and compared, micro-scaled rough and smooth epipolished and an additional smooth silica surface as a comparable reference. The investigations are performed macroscopically with contact angle and freezing onset measurements and microscopically with atomic force microscopy (AFM) and freezing out layer-by-layer nuclear magnetic resonance (NMR) spectroscopy, using the more rare flat coil probe head.

The freezing onset measurements showed a promoting freezing effect for sessile droplets on rough sapphire (RMS 120-180nm) versus the smooth sapphire (RMS 0.13-4.3) and smooth silica (RMS 0.59-4.3), at a relative humidity of 20-60 % and with different washing procedures. The results show that roughness impacts the freezing temperatures while the surface wetting properties were more inconclusive. However, based on uncertainties in the curvature analysis, it cannot be concluded if this is in line with CNT.

The flat coil ^{1}H-NMR measurements performed on double-plated sapphire samples were inconclusive in detecting a QLL, due to the interference of background noise signals. This, together with freezing temperature differences, means that the thesis did not find results that substantiate the modified nucleation theory. However, the NMR experiments did show interesting results of gradual freezing of water near the freezing temperature for rough sapphire and smooth silica samples.

Acknowledgements

I would like to give my greatest appreciation to my main supervisor Bodil Holst for making this master thesis possible. Thank you for all the valuable help, guidance and patience you have given me throughout this process. Thank to my co-supervisor, Espen Werdal Selfors, for being very helpful, for your guidance at the laboratory and for taking extra time for discussions. And thank you for the weekly meetings with you and Bodil, which have been very valuable to me. Your engagements in this field of science are really inspiring. I would also like to thank my co-suporvisors Willy Nerdal and John Georg Seland, for your contribution to the NMR spectroscopy experiments and analysis. I am very grateful for all contributions and help you have given me. And thank you to Josè C.R. Guerrero and Sabrina D. Eder for your technical assistance with the NMR spectrometer and 3D printing. And thanks to Randveig for taking the time for valuable discussions and help with the curvature analysis.

And at last, a very special thanks to my fiancé Henrik André Larsen for being there in the darkest days, both figuratively and quite literary speaking. This would not have been possible without your unconditional motivation and support. Thank you very much for showing and teaching me valuable drawing and excel skills, which have been tremendously time-saving.

Abbreviations

ACA Advancing Contact Angle

AFM Atomic Force Microscopy

BF Bright Field

CNT Classical Nucleation Theory

DSC Differential Scanning Calorimetry

FID Free Induction Decay

HDW High Denisty Water

LDW Low Density Water

LW Loosly Washed

MAS Magic Angle Spinning

MRI Magnetic Resonance Imaging

NMR Nuclear Magnetic Resonance

PAS Principal Axis System

QLL Quasi Liquid Layer

$\mathbf{r_c}$ Critical radius

RCA Receding Contact Angle

RH Relative Humidity

RMS Root Mean Square

TIR Total Internal Reflection

TMS Tetramethylsiliane

W Washed

WE Washed and Etched

WHH Width at Half Height

Contents

Chapter 1

Introduction

1.1 Background

Ice has the potential to form and aggregate anywhere, given the right conditions. What may seem like an elementary natural phenomenon is, in reality, a complex and not yet fully understood process. To this date, there is still no theory that by itself can comprehensively explain the how and why ice formation occurs on different types of surfaces [1]. Ice formation on surfaces has thus been a field of interest in science for many years, with numerous studies attempting to increase the understanding in this area. However, it is not only an intriguing subject for scientists but also imposes real-life challenges both in the industry and everyday life with regards to both safety, environment, and economy [2].

For instance, ice formation on airplanes can reduce their performance by up to 50%, thus imposing a safety risk if not removed [3]. De-icing of wings and fuselage is required to mitigate this risk, which leads to costly air traffic delays. Another example is ice aggregation on electric power lines that can lead to failures and shutdowns in electric supply and telecommunication, affecting a wide range of infrastructures and industries. Heavy ice formation on ships and platforms operating in cold and harsh environments may cause hazardous slippery decks and, in the worst case, affect the vessel stability [2]. Perhaps a more familiar example in everyday life is the ice-covered windshield on cars causing delays, energy consumption for heating, irritation, and in the worst case, a safety hazard in traffic if not removed.

Despite all the great technological advancements throughout the years, the methods for handling ice formation on surfaces have not changed much. The de-icing strategies used today are still mainly based on the same old principles involving heating, chemicals and mechanical removal. However, all of these solutions could potentially be detrimental to the environment, safety and economy [3–5].

Heating is one of the most common de-icing strategies used today. Examples include windshields on cars, heating elements on vessel decks, and heating for outdoor electrical equipment. The problem with heating as a de-icing strategy is that it requires a significant amount of energy to melt the ice, often with energy spills, e.g., heating cables that stay on after ice has melted [6, 7]. Additionally, if the energy consumption derives from non-renewable energy sources, as it will for diesel-driven ships and cars, it will contribute to more greenhouse gas emissions.

Another conventional de-icing strategy is the use of chemicals such as ethylene, propylene, glycols, and other chemicals with de-icing properties [7]. Perhaps the most known example of this may be the application of de-icing chemicals on airplanes before take-off, used to remove ice formation on wings and fuselage that may affect performance, lift and steering [2]. Chemical de-icing is also commonly used on car windshields and in industrial production. Unfortunately, using chemicals as a de-icing strategy also has its drawbacks. The chemicals used are toxic and potentially harmful to the workers handling them. Additionally, because de-icing chemicals are often used outside, there is a significant risk of leakage into nature. Leaked chemicals may reach and pollute groundwater and impose disease risk in drinking water or drain into the soil where it can be absorbed by plants and become an unwanted part of the ecosystem [3, 5]. Subsequently, an agreement has been made in the EU to reduce and phase out harmful chemicals, including de-icing chemical [8].

In many cases, ice formation on surfaces requires mechanical or manual removal. Manual removal of ice can be a demanding and dangerous task, thus imposing a potential safety risk for workers. This is especially the case in harsh and inaccessible environments, such as ships operating in arctic environments, windmills and power lines (e.g., after freezing rain) [3, 6].

1.2 State of the art

1.2.1 Anti-Icing Surfaces

The challenges imposed by ice formation and current de-icing strategies have led to high interest in developing more advantageous anti-icing methods. The ever-increasing knowledge of material surfaces, especially within nanotechnology, has given rise to numerous studies and advancements on surfaces and coatings with potentially icephobic properties [9]. Anti-icing surfaces and coatings are characterized by low freezing onset temperature, prolonged ice nucleation time (ice delay), or low ice adhesion strength that allows ice to be easily removed from the surface. Examples include superhydrophobic surfaces [10] that aim to prevent ice formation with water repellent properties and surface materials that use anti-freezing proteins [11] that strongly bond to water, preventing ice from forming. Other examples are slippery liquid infused porous surfaces (SLIPS) [12], and slippery liquid water layer (SLWL) [13] that both utilize a lubrication effect to achieve low ice adhesion. Additionally, a new fluorinated graphene coating is currently under research and development at UiB, showing promising results, with ice delay up to 6 hours and 45 minutes at temperature minus 5 °C in a high humidity environment ($50 - 55\%$) [4].

Even though there have been many attempts at developing efficient anti-icing surfaces and coatings, some challenges remain to be solved, such as changes in surface properties in humid conditions, surface robustness, and limitations in durability after numerous freezing cycles [10, 14]. Expanding the fundamental knowledge on ice formation on surfaces can potentially lead to enhancements in the development of new and better anti-icing surfaces and coatings, which form the basis of this thesis.

1.2.2 Understanding Ice Formation

There are still questions yet to be unraveled around the freezing process, especially regarding surface ice formation. The effect of external factors and different surface properties on ice formation, such as chemical composition, crystal orientations, curvature, and wettability, are still highly debated and not fully understood.

As there is no theory to accurately predict ice formation and freezing temperature points for a given surface, predictions are thus far mainly based on general crystallization and nucleation theory. According to nucleation theory, surface roughness should promote freezing and thus enable ice formation at higher temperatures than for smooth surfaces. However, several studies have shown experimental results inconsistent with the theoretically predicted values [15, 16]. The latter has especially been the case for surfaces with nano-scaled roughness, where some studies have shown no significant difference [16, 17] and some even suppression of freezing temperature contradictory to expectations [4, 15].

A study from 2014 [16] suggests that the explanation for the deviating results, especially for nanotextured surfaces, lies in the existence of a long-speculated quasi-liquid layer (QLL) between the ice and substrate [18]. The quasi-liquid layer differs from regular bulk water with a more rigid molecular structure. However, the existence of such a layer and its properties are still debated. The number of studies on QLL is still limited, but some studies have experimentally found traces of small amounts of unfrozen water between ice and substrate [19–22]. Among these, a study by Chen et al. found non-frozen water bound to a self-lubricating icephobic coating below freezing temperature [23]. Another study by Totland et al. also found small amounts of water at the interface between ice and SiO_2 particles [24].

A few studies suggest that the potential presence of a QLL can have a significant effect on surface freezing properties, namely ice adhesion, ice formation delay, and freezing onset temperature [16, 23, 25–27]. Hence the question of interest is if the existence of QLL can increase our understanding of ice formation on surfaces with different surface roughness and if this can be utilized in developing new solutions for anti-icing surfaces and coatings. These questions have become relevant for the Physics group at UiB, who has shown promising results in ice delay with a fluorinated graphene coating [4]. Could the presence of a QLL have caused these favorable results? The above-mentioned questions and related studies, together with a general motivation to expand the knowledge on ice formation on surfaces, form the foundation for the focus of this thesis.

Several studies that have found traces of a QLL used a method of freezing out layer by layer with solid-state nuclear magnetic resonance spectroscopy (NMR) [23, 24]. NMR is a suitable method for investigating QLL because of its ability to detect and trace amounts of water in the liquid phase, whereas ice remains invisible to the probe. Additionally, NMR can provide useful information about molecular structure and dynamics, such as diffusion and mobility. [23]. Most NMR studies investigate bulk water or just a few mono-layers of water absorbed on the surface with Magic Angle Spinning (MAS)-NMR. However, interfacial water has been found to extend beyond first water mono-layers and can be difficult to distinguish from bulk water experimentally [28]. Consequently, a study on water dynamics by Totland et al. [28] instead used a different method with a unique flat-coil probe head that allows for bigger samples in a horizontal position. This method thus makes it possible to investigate interfacial water between sample plates, which makes it a suitable method for this thesis.

1.3 Thesis Objective

The motivation for this thesis is to investigate the mechanisms of ice formation on sapphire surfaces, according to recently proposed theories, suggesting ice formation will occur at higher temperatures on rough surfaces than on smooth surfaces, with a quasi-liquid layer as a predominant role in this effect [16]. This is done by investigating the potential temperature difference and presence of a quasi-liquid layer on bare sapphire with two different surface finishes, one with roughness at microscale and one with a smooth epipolished surface.

Sapphire is chosen as it is widely used in lenses and other optical applications, thus making it a relevant material for the fluorinated graphene coating currently under development at UiB [4]. Additionally, a silica surface was introduced to resolve certain challenges with the experimental NMR setup. These materials are investigated mainly as a pre-study for future experiments on surfaces applied with a fluorinated graphene coating, which did not fit into this thesis.

The following experiments were done to investigate the thesis objectives:

- Freezing onset measurements to test nucleation theory and determine any difference in freezing temperatures for rough and smooth sapphire.
- Freezing out layer by layer NMR experiment to detect a potential presence of quasi-liquid layer. The method is inspired by the water dynamics study by Totland et al. [28], using a unique flat-coil probe head ideal for larger samples in a horizontal position, as the material surface samples in this thesis.

1.4 Thesis Outline

Chapter 2 presents the theory, including water properties related to surface ice formation, heterogeneous ice nucleation and quasi-liquid layer theory. Chapter 3 focuses on the principles of NMR spectroscopy. Chapter 4 introduces the equipment and experimental procedures used for investigating ice formation on sapphire and silica surfaces. Chapter 5 presents and analyses the results required from the experiments, followed by a discussion of the results in Chapter 6. Chapter 7 encloses the conclusion and suggestions for further work.

Chapter 2

Theory of Water and Ice

This chapter will present the essential concepts to understand the properties of water and ice formation on a solid surface. The fundamentals of water structure and wetting properties will be explained, which will be linked to freezing properties later. Secondly, the chapter will describe ice formation on surfaces based on the classical nucleation theory before finishing by describing a modified nucleation theory based on the presence of a quasi-liquid layer (QLL).

2.1 Water Structure and Properties

To understand the intricate process of wetting and ice formation on surfaces, it is beneficial to first have a grasp of the properties of water itself. Regular bulk water, but especially interfacial water, has complex and unusual properties that depend heavily on conditions such as temperature, pressure, structure, and surface chemistry [29]. Some of the abnormal properties of water include its surface tension, high heat capacity, viscosity, higher boiling temperature, and faster freezing of hot water than cold water [29, 30]. Water's complex and intricate properties originate from the water molecules' ability to form hydrogen bondings with other water molecules. The dipolar hydrogen bondings are the strongest of intermolecular forces and cause the water molecules to orient to the surrounding water molecules and thus form a particular water structure. However, even though water is one of the most common compounds on earth and has been widely researched, there are still many unknowns regarding the water's structure and complex properties.

Water, in liquid form, can be described by using a model with high-density water (HDW) and low-density water (LDW). LDW is defined as the water structure with the highest amount of hydrogen bondings between the water molecules, with an almost ice-like structure. HDW, on the other hand, has fewer hydrogen bondings that are more fluctuating and thus has very mobile water molecules [31]. Pure bulk water structure is described as a balance between HDW and LDW [31]. For interfacial water, the presence of a solid surface will impact and shift the balance of HDW and LDW due to the intermolecular interactions with the surface. For hydrophilic surfaces, a layer of HDW will form at the interface with a more distant LDW layer, whereas the opposite holds for hydrophobic surfaces [29]. While the knowledge of interfacial water dynamics is still limited, it is commonly accepted that the structured interfacial water molecules have a cascade effect, reorienting the successive water

layers towards the bulk water [24].

Interfacial water can be described by how bound the water is to the surface, termed as unbound, bound, or tightly bound. Adsorption interactions with a solid surface will reduce the Gibbs's free energy of bound water, changing the chemical potential and reducing the freezing temperature and mobility [29]. The degree of binding and mobility for interfacial water can be determined using thermal and spectroscopy techniques such as NMR [32].

2.2 Wettability

The complex intermolecular forces between interfacial water and a solid surface also affect the water's ability to maintain contact with the surface; a phenomenon called wetting. The cohesive forces are the attracting internal forces within a liquid that cause surface tension, which in the absence of gravity naturally gives the liquid a spherical shape. Whereas adhesive forces act between the liquid and the surface, causing the liquid to increase contact and thus spread across the surface. The balance between the cohesive and adhesive forces determines the wettability, which can be found by measuring or predicting the contact angle θ, as will now be explained.

2.2.1 Contact Angle

For water droplets, the contact angle is the angle in the boundary of the three involved phases of vapor, liquid, and solid, as shown in Figure 2.1. A low contact angle of 90° or less indicates a high- to perfect surface wettability, while a higher contact angle between 90° and 180° indicates a low- to non-wettability of the surface. A low wettability surface is regarded as hydrophobic, whereas a high wettability surface is hydrophilic. If the contact angle is higher than 150° it is termed as a superhydrophobic surface [33].

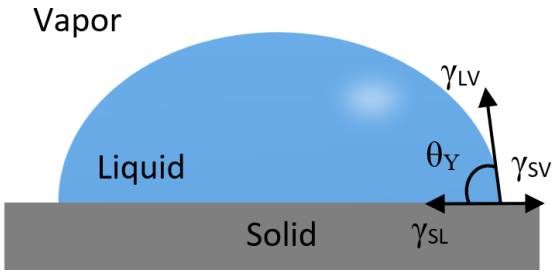

Figure 2.1: Schematic drawing of static contact angle θ_Y of a droplet on surface. γ_{SV}, γ_{SL}, γ_{LV} denotes the surface energy of the solid-vapor, solid-liquid and liquid-vapor interface, respectively.

For an ideal smooth solid surface that is chemically homogeneous, only one thermodynamic stable static contact angle can exist. Using trigonometry and mechanical equilibrium of the surface tension energy for each phase boundaries, the net forces can be transformed and expressed by Young's equation 2.1 [34]:

$$\gamma_{SV} = \gamma_{SL} + \gamma_{LV} \cos\theta_Y \tag{2.1}$$

Where γ_{SV} is the surface tension for solid-vapor, γ_{SL} is the surface tension for solid-liquid, and γ_{LV} for liquid-vapor, and θ_Y is the static contact angle at equilibrium.

However, surfaces will rarely have the ideal properties according to the assumptions used in Young's equation with a presumed stable global energy minimum. The non-ideal surface may have imperfections, roughness, or chemical heterogeneity that impact the contact angle, creating local meta-stable energy minimums [35]. This implies that a static contact angle is not necessarily reproducible. These deviations from the ideal contact angle are termed contact angle hysteresis, given as the difference between the advancing angle θ_A (ACA) and receding angle θ_R (RCA) as seen in Figure 2.2. The contact angle hysteris is thus expressed as Equation 2.2 [36].

$$H = \theta_A - \theta_R \tag{2.2}$$

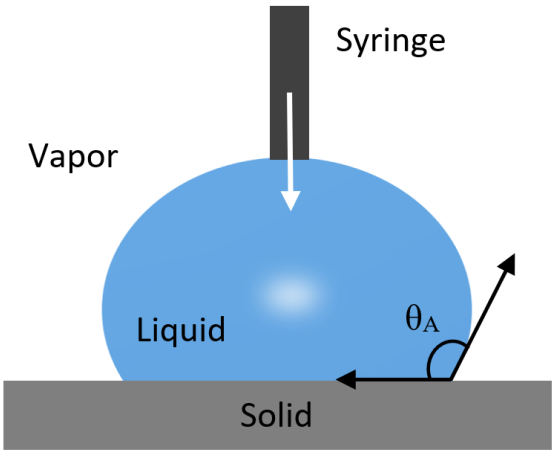

(a) Advancing contact angle θ_A

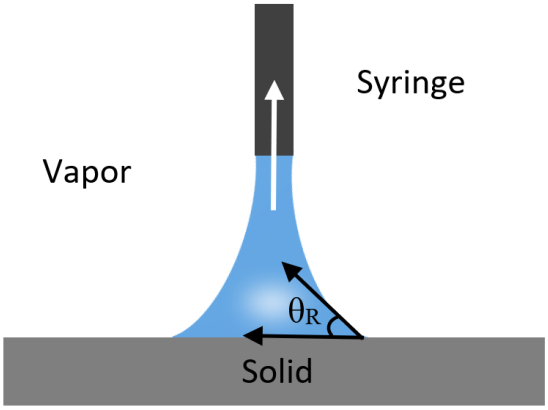

(b) Receding contact angle θ_R

Figure 2.2: Schematic drawing of a droplet on surface with expanding (a) and contracting (b) volume, resulting in advancing θ_A and receding θ_R contact angle.

There will be many different meta-stable static contact angles θ_Y for any given liquid-solid system, found as a range between the advancing angle θ_A and receding angle θ_R. These angles can be measured experimentally by adding and subtracting water and tracking the RCA and ACA.

2.2.2 Wenzel and Cassie-Baxter Wetting Regimes

Actual non-ideal surfaces with rough textures require more complex models to describe the liquid-solid wetting interaction and find contact angles. The two main models used for this matter are the Wenzel [37] and Cassie-Baxter [38] wetting regimes.

Both the Wenzel and Cassie-Baxter model require the droplet size to be significantly larger than the surface roughness to be applied.

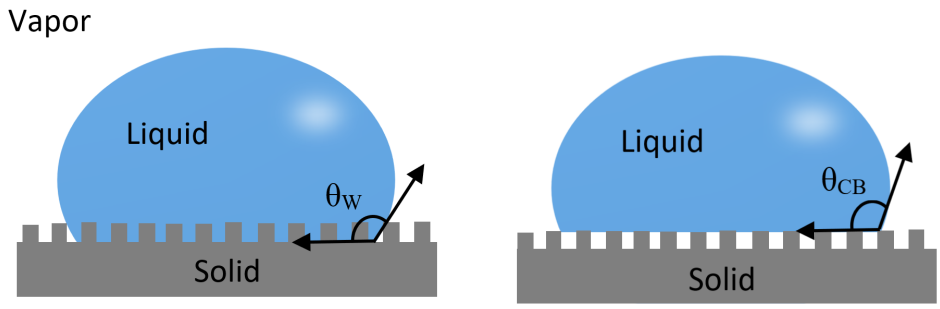

(a) Wenzel state (b) Cassie-Baxter state

Figure 2.3: Schematic drawing of wetting regimes of a droplet according to Wenzel model (θ_W) and Cassie-Baxter model (θ_{CB}) respectively.

The Wenzel model is used to describe the wetting regime for rough surface textures, where the liquid is assumed to fill all the surface curvatures as shown in Figure 2.3. According to this model, the increase in surface area, due to the curvatures, will enhance wettability when wetting is favorable, and the opposite for low wettability. The contact angle for this model is defined by the Wenzel equation 2.3 [37]

$$\cos\theta_W = r\cos\theta_Y \tag{2.3}$$

Where θ_W is Wenzel angle, r is the roughness factor given as actual surface area divided by ideal surface area, and θ_Y is Young's contact angle for an ideal surface of the same material.

The Wenzel model becomes inadequate for heterogeneous surfaces with various materials, and the more extensive Cassie-Baxter model has to be used. This model assumes that the liquid does not fill the curvatures in the surface and thus leaves small pockets of air in the interface, as shown in Figure 2.3. This liquid-air combination on surfaces promotes hydrophobic properties and can thus be used to make hydrophobic and superhydrophobic surfaces. In nature, the Cassie-Baxter wetting regime can be observed on the characteristic lotus leaves that have a rough surface structure with low contact angle hysteresis. This result is superhydrophobicity and water droplets rolling off the leaves. The contact angle for this model is defined by the Cassie-Baxter equation 2.4 [38]

$$\cos\theta_{CB} = rfcos\theta_Y + (f-1) \tag{2.4}$$

Where θ_{CB} is the Cassie-Baxter angle, r is the roughness factor, f is the solid-area fraction, and θ_Y is Young's contact angle for an ideal surface of the same material.

Note that when the solid-area fraction $f = 1$, the Cassie-Baxter equation becomes the Wenzel equation. This is reflected in reality as the wetting regime is primarily in between these two models with partially filled curvatures and dynamic transition from Cassie-Baxter to Wenzel state [33]. An external force, such as gravity or vibration, is necessary to exceed the energy barrier, attain the critical angle θ_C and thus initiate the transition. The liquid will then gradually fill the air pockets starting from the center of the droplet. The conditions of the Cassie-Baxter to Wenzel state transition are given by Equation 2.5 [39]

$$\cos\theta_C = \frac{\phi - 1}{r - \phi} \tag{2.5}$$

Where θ_C is the critical contact angle, ϕ fraction of drop contact with solid, and r is the roughness factor. The transition reaches the Wenzel state when the liquid has filled all air pockets to the droplet's edges.

2.3 Ice Formation Theory

Ice formation, in its simplest term, is a phase transition from water (vapor or liquid) to ice (solid), which occurs at temperatures below 273.15 K. However, the underlying mechanisms of the ice formation process are complex due to water molecules' unique and intricate behavior [29]. Ice formation is impacted by a variety of factors, including environmental conditions such as temperature, humidity, gas flow, droplet impurities, and mechanical disturbance (e.g., droplet vibration) [9, 29, 40]. It is also impacted by the chemical properties of the solid surface, essentially the surface wettability and curvatures. Some recent studies suggest that the classical nucleation theory, commonly used to describe ice nucleation, failed to predict nucleation temperature for surfaces with nanostructures [9, 16]. In the context of anti-freezing coatings and surfaces, it is of high interest to gain a greater understanding of the ice formation process and the still unanswered questions around this complex subject.

As with other thermodynamic phase transitions, ice formation happens through a process of crystallisation consisting of nucleation and growth phase. The nucleation starts with a small group of water molecules merging into small ice-like clusters, continuously forming and unforming meta-stable ice embryos, also known as ice nuclei. As shown in Figure 2.4, the nucleation will happen either in the interface between liquid and air (homogeneous nucleation) or in the interface between the liquid and a solid compound, such as a solid surface or impurities (heterogeneous nucleation). Stable ice embryos are formed after reaching a critical size and thus exceeding the energy barrier, followed by spontaneous crystallisation and further ice growth as seen in Figure 2.5.

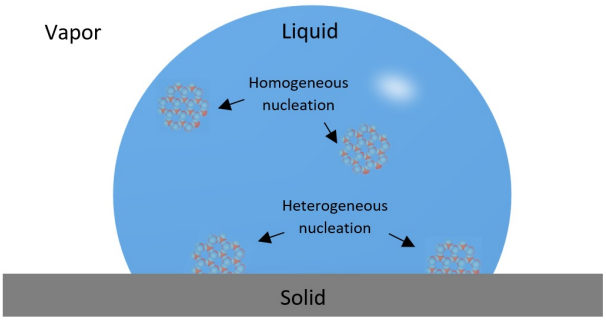

Figure 2.4: Schematic drawing of heterogeneous and homogeneous ice nucleation in a droplet. Figure redrawn and adapted from [41]

2.3.1 Classical Nucleation Theory

The classical nucleation theory is commonly used to describe the kinetics and thermodynamics of nucleation in a phase transition, thus also ice nucleation. This theory describes the conditions that have to be met for stable ice nucleation to occur, expressed in terms of nucleation rate as in equation [42–44]:

$$J = Ke^{-\Delta GkT} \tag{2.6}$$

Here, J is the nucleation rate as ice embryos per volume time, k is the Boltzmann constant, and T is the freezing temperature. ΔG is the Gibbs free energy barrier, which can be regarded as the work W_c required to overcome the energy barrier for a stable embryo to form [41] as seen in Figure 2.5. The Gibbs free energy barrier is thus central in the classical nucleation theory and in determining the nucleation rate. K is a kinetic prefactor for the diffusion of free water molecules in the water-ice interface. The kinetic prefactor includes the diffusion activation energy for the molecules to cross the interface and the molecule number density [43, 45], given as:

$$K = Z(\nu A^*)N \tag{2.7}$$

Where N is the number of atomic nucleation sites per volume unit, νA^* is the rate at the molecules form stable ice embryos with ν termed as the impingement rate and A^* the surface area of critical ice embryo. Z is a probability factor of ice embryos exceeding the energy barrier. In terms of ice formation delay, according to the classical nucleation theory, it would thus be beneficial to minimise the prefactor K and maximise the Gibbs free energy barrier ΔG.

For an assumed spherical nucleus with radius r, Gibbs free energy will have both a volumetric and a surface component expressed as following [43]:

$$\Delta G = n\Delta\mu + A\gamma_{IW} = \frac{4}{3}\pi r^3\rho_c\Delta\mu + 4\pi r^2\gamma_{IW} \tag{2.8}$$

Where n is the number of particles in an ice embryo given as $\frac{4}{3}\pi r^3\rho_c$ for a sphere with ρ_c as particle density. $\Delta\mu$ is the difference in chemical potential in a phase transition, A the surface area given as $4\pi r^2$ for a sphere, and γ_{IW} is the ice-water interfacial tension.

The volumetric free energy difference, expressed as ΔG_v, is the energy difference per unit volume of ice and water given by the Gibbs-Helmholtz equation (listed in Appendix B.3.2), corresponding to $\Delta\mu$ in equation 2.8 [41].

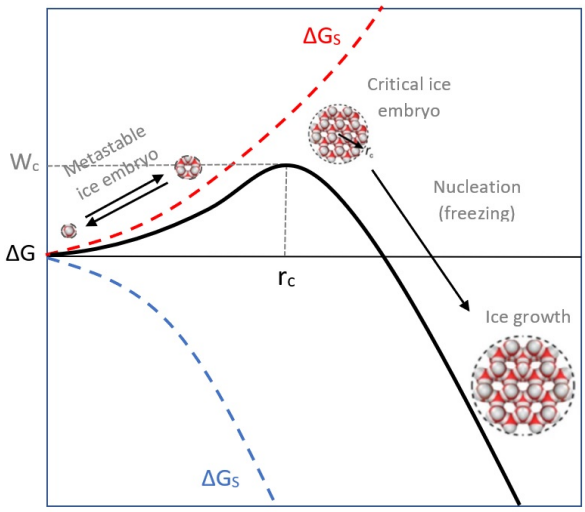

Figure 2.5: Gibbs free energy barrier, with its volumetric component ΔG_v and surface component ΔG_s, plotted against the ice embryo radius. r_c is the critical radius and W_c is the required work to overcome the energy barrier. Figure inspired by [41] and [46]. Image of ice embryo structure copied from [41]

Figure 2.5 shows how the surface free energy component will dominate for ice embryos with a small radius, whereas the volumetric free energy component dominates at a larger radius. A critical radius corresponds to the Gibbs free energy barrier necessary to overcome for stable ice nucleation to occur and grow further. After the nuclei reach critical radius, the Gibbs free energy will decrease and eventually become negative, where ice embryo growth becomes highly favorable. The critical radius is found at the maximum Gibbs free energy barrier. Thus, the derivative of equation 2.8 becomes:

$$[\frac{dG}{dr}] = 0, \rightarrow r_c = \frac{2\gamma_{IW}}{\Delta G_v} \tag{2.9}$$

The Gibbs free energy barrier ΔG that a spherical ice embryo must overcome to initiate stable homogeneous nucleation is obtained by inserting the equation for critical radius 2.9 into equation 2.8

$$\Delta G_{hom} = \frac{16\pi\gamma_{IW}^3}{3(\Delta G_v)^2} \tag{2.10}$$

This equation is valid for homogeneous nucleation for ice embryos with an assumed spherical form. However, this will not be the case for heterogeneous nucleation, where part of the nucleus interfaces with another compound, e.g., solid surface and dust particles. The surface area and thus also the surface component of the free energy barrier will always be smaller for heterogeneous nucleation, making it the most dominant of the processes. Water in pure vapor without any impurities can exist at temperatures as low as 233 K before homogeneous nucleation takes place [40]. Naturally, heterogeneous nucleation is also the most relevant in this thesis when studying the freezing of water on different surfaces.

To take into account the reduction in Gibbs free energy barrier impacted by a solid compound in heterogeneous nucleation, a geometrical factor f between 0 and 1 is added

to 2.10. The geometrical factor f relates to the homogeneous nucleation as $f = \Delta G_{het}$ / ΔG_{hom} [42, 47], resulting in equation 2.11. Note that when the geometrical factor $f = 1$, equation 2.11 becomes similar to ΔG_{hom} in equation 2.10.

$$\Delta G_{het} = \frac{16\pi\gamma_{IW}^3}{3(\Delta G_v)^2} f(\theta_{IW}, R) \tag{2.11}$$

The geometrical factor f is expressed as a function in terms of static contact angle θ_{IW} for ice-water interface and the curvature radius R, given in equation 2.12 for convex surfaces and in equation 2.13 for concave surfaces [42, 44]

$$f_v(\theta_{IW}, R) = \frac{1}{2}\left\{1 + \left(\frac{1-mx}{g_v}\right)^3 + x^3\left[2 - 3\left(\frac{x-m}{g_v}\right) + \left(\frac{x-m}{g_v}\right)^3\right] + 3mx^2\left(\frac{x-m}{g_v} - 1\right)\right\}$$
$$g_v = (1 - 2xm + x^2)^{\frac{1}{2}}, x = R/r_c, m = cos(\theta_{IW}) \tag{2.12}$$

$$f_c(\theta_{IW}, R) = \frac{1}{2}\left\{1 - \left(\frac{1+mx}{g_c}\right)^3 + x^3\left[2 - 3\left(\frac{x+m}{g_c}\right) + \left(\frac{x+m}{g_c}\right)^3\right] + 3mx^2\left(\frac{x+m}{g_c} - 1\right)\right\}$$
$$g_c = (1 + 2xm + x^2)^{\frac{1}{2}}, x = R/r_c, m = cos(\theta_{IW}) = \frac{\gamma_{SW} - \gamma_{SI}}{\gamma_{WI}} \tag{2.13}$$

Real surfaces consist of both convex bumps and concave pits that will affect the geometrical factor simultaneously. Note that the curvature radius R in $f(\theta_{IW}, R)$ is for a singular pit or bump, in reality a surface consists of a wide variety of pits and bumps across the surface. The curvature radius expresses the choppiness of the curvature as defined in Figure 2.6. Surface roughness is normally measured by root mean square (RMS), which must not be confused with curvature radius. Roughness RMS is measured as the average height deviations from the middle line (see equation B.13 in Appendix B.3).

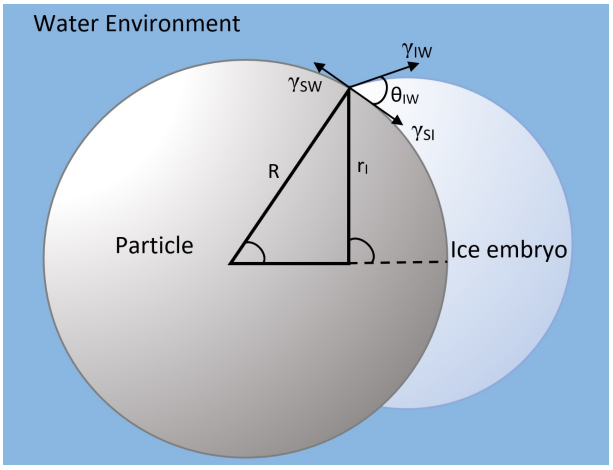

Figure 2.6: Schematic drawing of ice embryo with radius r_I on a solid particle with radius R. θ_{IW} is the contact angle of the ice embryo on the particle, and γ_{SW},γ_{IW} and γ_{SI} denotes the solid-water, ice-water and solid-ice interfacial tension. Figure inspired by [42].

In figure 2.7 the geometrical factor f is plotted versus $x = R/r_c$ for convex surface roughness and concave surface roughness respectively, with a variety of different contact angles.

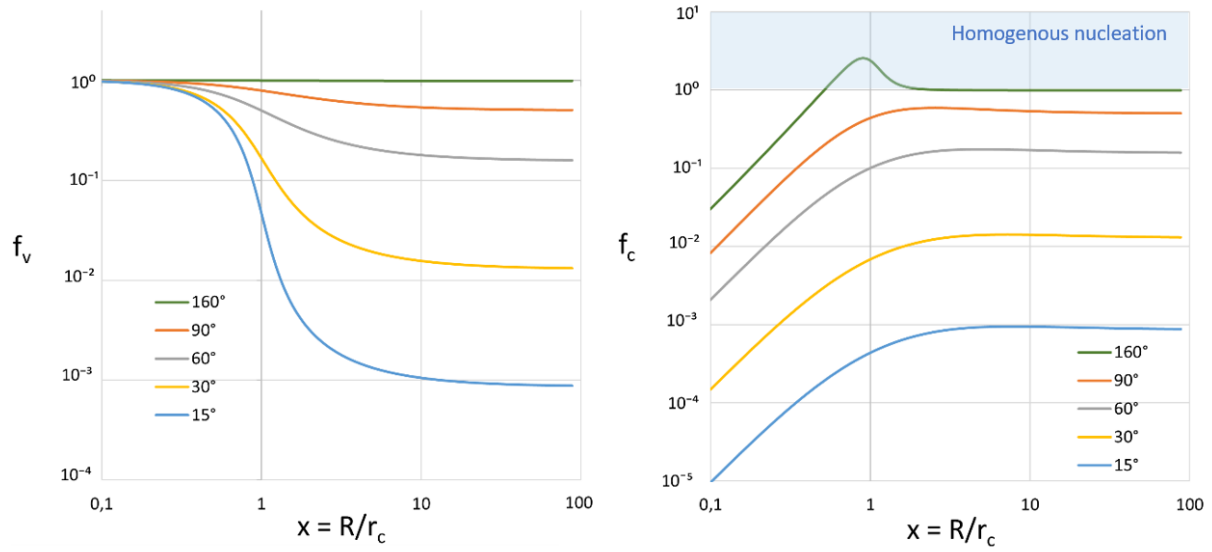

Figure 2.7: In figure 2.7 the geometrical factor f is plotted versus $x = R/r_c$ for convex f_v surface roughness and concave f_c surface roughness respectively, with a variety of different contact angles θ, (160°, 90°, 60°, 30° and 15°). When $f \geq 1$ homogeneous nucleation will dominate (blue shaded area).

In figure 2.7 the geometrical factor f is plotted versus $x = R/r_c$ for both convex and concave surface roughness. The plots show that the geometrical factor f is only affected by the given curvature roughness when $x < 10$. Hence, the ice nucleation rate will only be affected by the surface roughness when $R < 10r_c$. When the curvature $R > 10r_c$, the area is regarded as flat with no expected difference in ice nucleation from a flat surface, and thus the geometrical factor is only affected by the contact angle [17]. For convex surface curvature (bumps), the geometrical factor f will approach 1 with increasing ΔG and thus suppress ice nucleation. On the other hand, the concave surface curvature (pits) will reduce f significantly, decreasing ΔG and thus promoting ice nucleation. Due to the very low ΔG, the pits will dominate the ice nucleation on nanotextured surfaces containing both bumps and pits. Hence, according to the classical nucleation theory, practical nanotextured surfaces promote ice nucleation.

However, several recent studies have shown results that are inconsistent with predictions from the classical nucleation theory, this has especially been the case for nanoscaled surfaces [15, 16]. Some of these studies have shown experimentally a suppressing effect on ice nucleation for materials with roughness $R < 10r_c$ [4, 15]. Other studies have found that various hydrophilic and hydrophobic surfaces with different roughness, including $R < 10r_c$ and $R > 10r_c$, had a negligible effect on freezing temperature [17, 48]. The impact surface curvature and wettability have on ice nucleation are still debated, but there are indications

pointing towards surface roughness having a greater impact than surface wettability [49,50]. It has been proposed that the inconsistencies with the classical nucleation theory observed in several studies might be explained by the presence of a quasi-liquid-layer (QLL) between the solid surface and the ice-embryo [16]. This will be discussed in the next section.

2.3.2 Quasi-Liquid Layer Theory

The quasi-liquid layer is suggested to be a thin layer of non-frozen water, below freezing temperature, in the interface between an ice embryo and a solid surface, as shown in Figure 2.8. The existence of such a layer has been debated for many years [18]. The first theory of a liquid-like layer at the phase interface of ice and vapor was postulated by Faraday in 1850 [51]. This postulation was later developed to also apply to the interface between solid and ice by Weyl [18,52]. A more recent study by Eberle et al. [16] argued that if a quasi liquid layer exists in the interface between ice and a solid, it also has to exist between ice-embryo and solid. Several recent studies have found traces of non-freezable water below freezing temperature, in the interface between ice and several hydrophilic and hydrophobic surfaces, with different textures [20, 21, 23, 24, 29, 53].

The QLL is strongly bound/bound interfacial water with a suggested thickness from one to several monolayers [25, 29]. However, the knowledge of the QLL properties are still limited [23–25, 29]. Emelyanenko et al. [27] suggest that the structure of the confined QLL is affected by the interfacial surface forces. These forces can change the density and pressure in the liquid layer, leading to a shift in the thermodynamic phase triple point, which again can, e.g., change the freezing temperature [27]. Even though the properties and potential impact of QLL are still unknown, several studies suggest that it might impact surface freezing properties. Studies have shown a significant reduction in ice-adhesion strength with the presence of QLL [26, 27]. Other studies have shown increased ice delay [16] and lowered freezing temperature [23, 24]. Taking the presence of QLL into account, a modification of the classical nucleation theory can be derived to explain results deviating from predicted values from classical nucleation theory [16, 27]

Modified Classical Nucleation Theory

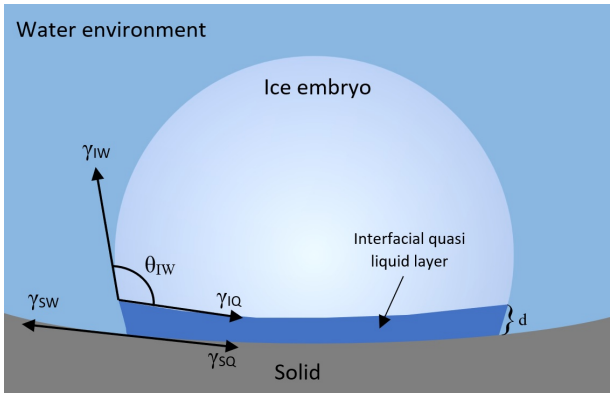

Figure 2.8: Schematic drawing of quasi liquid layer existing at the interface between an ice embryo and solid surface. γ_{SW}, γ_{IW}, γ_{IQ} and γ_{SQ} denoted the surface energies at the interface of surface-water, ice-water, ice-QLL and surface-QLL respectively, and θ_{IW} is the contact angle of the ice-embryo and water. Figure copied from [16]

Figure 2.8 shows a schematic drawing of a quasi-liquid layer formed in a nanoscaled pit on the solid surface in the interface with an ice embryo. The study by Eberle et al. [16] showed that the effect of the QLL on ice embryos in nanopits led to a significant change of contact angle θ_{IW}, depending on the curvature radius R, thus a difference in the nucleation characteristics. The study refers to this effect as the nanoscale interface confinement effect. Taking the effect of the QLL into account, a modification of the Young's equation 2.1 can be derived from balancing the interfacial forces, as shown in Figure 2.8, leading to Equation 2.14 [16]

$$\begin{aligned} \cos(\theta_{IW})\frac{\gamma_{IW}}{\beta} = \gamma_{SW} - \gamma_{SQ} - \frac{\gamma_{IQ}}{\beta} = \left(\gamma_{SW} - \frac{\gamma_{IW}}{\beta} - \gamma_{SI}\right) e^{\frac{-d}{\xi}} - \frac{\gamma_{IW}}{\beta} \\ \beta = \frac{R}{R-d}^{2}, \gamma_{IQ} = \gamma_{IW}\left(1 - e^{\frac{-d}{\xi}}\right), \gamma_{SQ} = \gamma_{SI}e^{\frac{-d}{\xi}} + \gamma_{SW}\left(1 - e^{\frac{-d}{\xi}}\right) \end{aligned} \tag{2.14}$$

Here the surface energies are denoted as γ_{ILL} between the ice and QLL, γ_{SLL} between ice and surface, γ_{SI} between surface and QLL, and γ_{SW} between surface and liquid. d and ξ represent the thickness of QLL and the characteristic decay length of interaction with bulk. Equation 2.14 can be transformed into:

$$\cos\left(\theta_{IW}\right) = \left(\cos\left(\theta_{IW}^{*}\right) + 1\right)\beta e^{\frac{-(d-d^{*})}{\xi}} + (1-\beta)e^{\frac{-d}{\xi}} - 1 \tag{2.15}$$

Here the $*$ represent a flat surface where $R \to \infty$. Thus, when the curvature radius $R >> d$, Equation 2.15 can be written as:

$$\cos\left(\theta_{IW}\right) \approx \left(\cos\left(\theta_{IW}\right)^{*} + 1\right)e^{\frac{-(d(R)-d^{*})}{\xi}} - 1 \tag{2.16}$$

This equation is plotted in Figure 2.9 (green dotted line), showing the dependence between θ_{IW} and the roughness curvature radius R (from 1 to 100 nm). The figure further shows the

median freezing temperature T_N for a surface covered with 15 % nanopits, calculated based on the classical nucleation theory (blue dotted line) and with a modified nucleation theory with QLL taken into account (black solid line). Hence, comparing these two demonstrates how the presence of QLL counteracts the ice-promoting effect of nanopits, as expected from CNT. This is also aligned with the experimental results from the Eberle et al. study [16] showing that a surface with roughness $R < r_c$ had as much as ten times as freezing delay compared to surfaces with $R > r_c$ [16]. Since the interface confinement effect counteracts the ice-promoting effects of nanopits, the rest of the surface texture, including nanobumps and flat areas, will dominate the ice nucleation process.

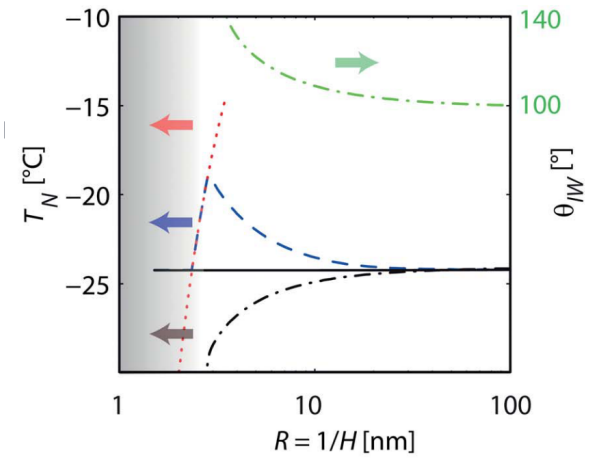

Figure 2.9: The green line shows how θ_{IW} varies with R due to the confinement effect based on Equation 2.16. The blue line shows the median nucleation temperature T_N for a surface with 15 %nanopits and constant $\theta_{IW} = 100°$, calculated based on the classical nucleation theory. Thus this line demonstrates the expected ice promoting effect for the surface with a given roughness curvature radius R. The black solid line shows the same surface with a QLL taken into account, where the confinement effect will progressively increase θ_{IW} with decreasing R. This demonstrates how the presence of QLL counteracts ice promoting effects and keep the freezing temperature T_N is constant. The dashed black line is the same calculations but for a hypothetical surface with 100 % nanopits. The melting point depression curve based on Gibbs-Thomson relation is plotted as the red dotted line. Figure copied from [16]

The research of Akhar et al. [4] showed a significant difference in freezing temperature for nearly flat surfaces with nanoscaled roughness (RMS< 2.5nm) of sapphire, graphene, and fluorinated graphene. Thus, these results imply that the surface's chemical composition also significantly impacts the surface freezing properties. As mentioned in the introduction 1.3, this thesis will investigate the freezing temperature and diffusivity of interfacial water on flat and rough sapphire and the potential presence of a quasi-liquid layer using NMR spectroscopy. The thesis may be regarded as a pre-study for further studies on the potential presence of QLL on fluorinated graphene coating and if the existence of such a layer could explain the favorable results. The proposed modified nucleation theory is a step closer to increasing the knowledge of QLL and its potential impact on surface freezing properties.

However, there are still questions to be unraveled and studies showing contradicting results; thus, further research is required.

Chapter 3

Principle behind NMR-Spectroscopy

This chapter introduces the general principles and concepts for understanding NMR-spectroscopy.

3.1 Nuclear Magnetic Resonance Spectroscopy

Nuclear magnetic resonance (NMR) spectroscopy is a widely used method to measure and analyze the structure and bonds in molecules. The basis for this method is the interactions between weak magnetic forces of a nucleus of one species and an applied static magnetic field. Differences in the chemical and molecular environment give rise to differences in absorbed frequencies presented in NMR-spectrum and signal intensity.

A central concept to understanding NMR spectroscopy is spin's intrinsic property, which most nuclei possess. For an atomic nucleus with either odd numbers of protons and/or neutrons, the spin in combination with the charge of protons results in a weak magnetic field and thus an angular momentum P [54]. Quantified angular momentum is given by the following equation:

$$P = \sqrt{I(I+1)}\hbar \tag{3.1}$$

Here I represents the spin quantum number and $\hbar$ is defined as $\hbar = \frac{h}{2\pi}$, where h is Planck's constant. Thus, only nucleus with $I > 0$ will have an angular momentum. A magnetic momentum μ, is found proportional to the angular momentum $\vec{P}$ given by:

$$\vec{\mu} = \gamma \vec{P} \tag{3.2}$$

Here γ is the magnetogyric ratio specific for different nuclei. The magnetogyric constant of a nucleus also affects its detectability. A higher value of γ will make it more sensitive and easier to observe in NMR spectroscopy [54].

If an external static magnetic field, $\vec{B_0}$ is applied for a nucleus with $I > 0$, the angular momentum will start to precess around the direction of the magnetic field. The z-component of the angular momentum is described as:

$$P_z = m\hbar \tag{3.3}$$

Here m is the magnetic quantum number which can have the values I, I-1, ..., -I. For ^{1}H nucleus which has the spin quantum number $I = \frac{1}{2}$, there exist two values for m, $\frac{1}{2}$ and $-\frac{1}{2}$.

These two values correspond to the orientations or directions aligned with or against the applied magnetic field. A nucleus can also have more than two orientations, depending on its quantum number [54].

The two orientations for ^{1}H give rise to two distinct energy states, also called Zeeman levels, where the energy E is quantified by the following equation [55] [54]:

$$E = -\mu_z B_0 = -m\gamma\hbar B_0 \tag{3.4}$$

Here, B_0 is the magnetic flux density. Nucleus spinning in alignment with the applied magnetic field possesses the lowest energy level, denoted as α-state with $m = \frac{1}{2}$. In the case where the nucleus is spinning with momentum against the applied magnetic field, thus having the highest energy level denoted as β-state with $m = -\frac{1}{2}$ [55]. The Boltzmann's distribution determines the distribution of which state the spins are in:

$$\frac{N_\beta}{N_\alpha} = e^{-\frac{\Delta E}{K_B T}} \tag{3.5}$$

Here N_β and N_α are the number of nuclei in the two different energy states, ΔE is the energy difference between β- and α-state, T is the temperature, and k_B is Boltzmann's constant. As $E_\beta > E_\alpha$, more nuclei tend to exist in the α-state, but as the energy difference of protons and most nuclei are very small compared with $K_B T$, the distribution will be close to equal in thermal equilibrium [54].

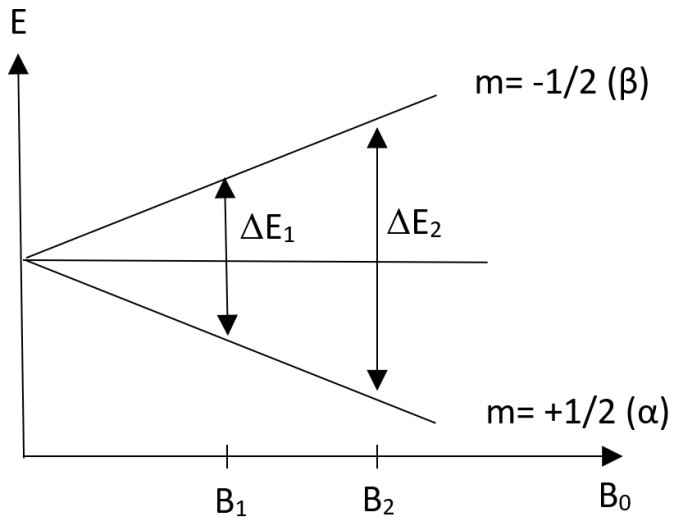

Figure 3.1: Shows how the energy gap ΔE between α- to β-state is effected by the magnetic field B. Illustration redrawn from [54]

The energy gap between these two energy levels is proportional to the applied magnetic field, as defined in equation 3.6. If this exact energy amount is added to the nucleus, the nucleus spin can be flipped and thus transitioned between the β and α -energy levels. The transitions between energy levels will go both ways, but since there is naturally more nucleus

in the α-state the dominating process will be the transition from α- to β-state. This results in either absorption or emission of energy, depending on the direction of the transition [54].

$$\Delta E = \gamma \hbar B_0 = h\nu \tag{3.6}$$

Here v corresponds to the frequency of the transition. In an NMR experiment, the nuclei are placed in a static magnetic field and irradiated with radio frequency waves of ν_1. The frequency must correspond precisely to match the energy required to induce transitions, the same frequency in which the nucleus is spinning around its own axis. The distribution between energy levels will be equal at a particular frequency, and thus no signal will longer appear. This specific frequency is often referred to as the Larmor frequency (ν_L) [54].

$$\nu_1 = \nu_L = \left| \frac{\gamma}{2\pi} \right| B_0 \tag{3.7}$$

Here, B_0 is the magnetic flux density, and γ is the magnetogyric ratio for the specific nucleus. The magnetogyric ratios for different nuclei vary significantly because of different chemical environments, limiting the NMR method to only process one type of nucleus at a time [54].

3.1.1 The Pulse NMR Method

The most commonly used method for NMR spectroscopy today is the pulse NMR method [56]. This method differs from earlier used NMR methods as it uses pulses of radio frequency waves in a static magnetic field instead of a continuous radio frequency in a dynamic magnetic field. While the traditional method directly measures the absorption and emission to create an NMR spectrum, the pulse method instead measures a free induction decay (FID) after a radio frequency pulse, that is Fourier transformed into an NMR spectrum.

Since all nuclei in a sample are precessing around the axis of the applied field B_0, but in different phases, the magnetization components in the x- and y-direction will be canceled out. The result is a net bulk magnetization (denoted M_0) along the direction of the external field, as shown in Figure 3.2

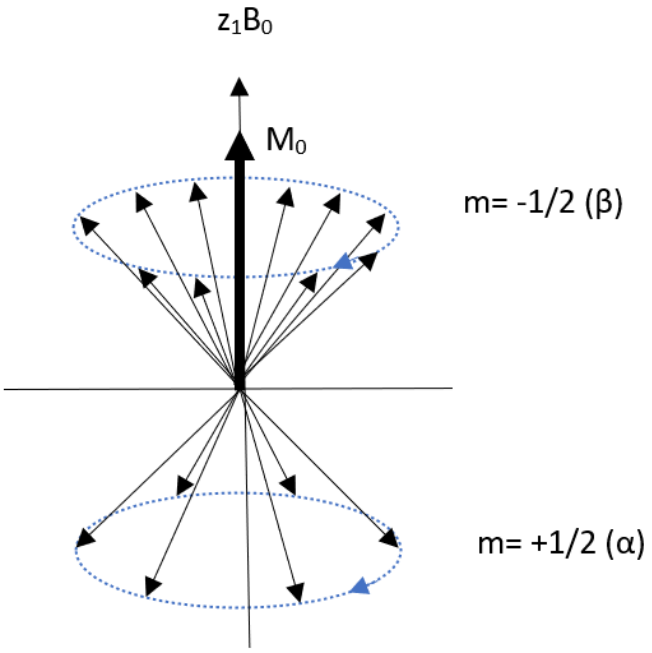

Figure 3.2: Schematic drawing of magnetization (M_0) of a sample in a static field (z_1B_0). Illustration redrawn from [54]

Sending a radio frequency pulse along the x-axis will affect the net bulk magnetization. The nuclei in the sample will start precessing around the z-axis aligned in the same phase, also called phase coherence. The net bulk magnetization will thus be tilted and precess in the x-y plane as shown in figure 3.3. The tilting angle depends on the pulse duration, where the most common angles are 90^o and 180^o. An NMR experiment may consist of one pulse or several pulses in a pulse sequence. Since the magnetization components are still rotating in the x-y plane, a rotating plane x'-y'-plane is used, rotating at Larmor frequency. When the radio frequency pulse is switched off, the nuclei will gradually transition back to normal disordered condition, a process called relaxation. This will gradually tilt the net bulk magnetization back to the z-axis.

A coil placed around the sample will induce an oscillating electric field due to the rotation of the magnetization in the x-y plane, denoted M_{xy}. Detectors measure this oscillating electric field in the x-y plane, where the signal is determined by M_{xy}. The amplitude will decay over time, as the system relax back to it's original state. The detected signal is called free induction decay (FID). By applying Fourier transformation (Equation 3.8), an NMR-spectrum can be generated. This spectrum will show the same as for conventional NMR methods with frequencies on the x-axis and intensity of absorption on the y-axis with resonance spikes at Larmor frequencies.

$$g(\omega) = \int_{-\infty}^{\infty} f(t)e^{-i\omega t}dt \tag{3.8}$$

Here g(w) is a complex function which corresponds to the spectrum in the frequency domain

and $f(w)$ to that in time domain [54].

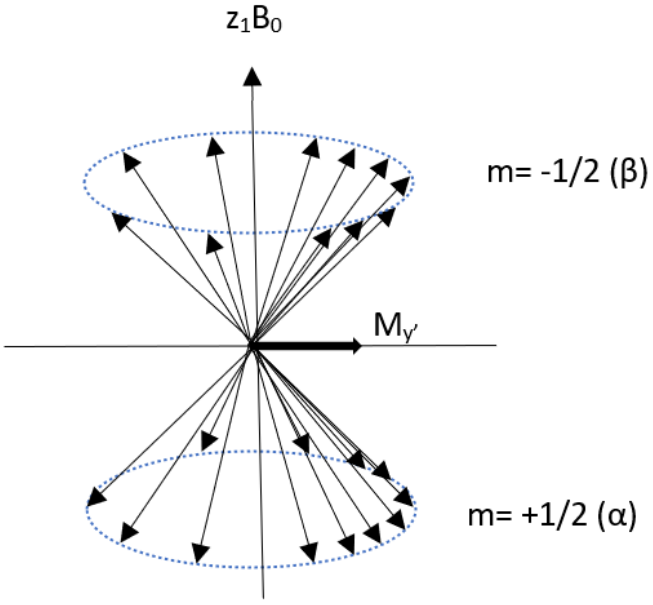

Figure 3.3: Shows magnetization M_y after 90° pulse. Illustration redrawn from [54]

3.1.2 Relaxation

The relaxation process described in the NMR pulse method consists of two types of relaxation processes, the spin-lattice relaxation T_1 and the spin-spin relaxation T_2 [54]. After perturbation, the Boltzmann-distributed populations of energy levels are disturbed. When the pulse is switched off, the system will start the relaxation phase and transition back to equilibrium. The spin-lattice relaxation process happens through spin flipping from the excited state to the ground state, thus emitting energy to the surroundings and lattice. A change in the bulk magnetization in the z-axis can also be observed. The time it takes before the net bulk magnetization of the nuclei is back to its original state at the z-axis is defined by equation 3.9. For ^{1}H-NMR there are generally minor variations in T_1 values [57].

$$\frac{M_z}{M_{eq}} = -1 - Ae^{-\frac{t}{T_1}} \tag{3.9}$$

Here M_z is the z-component of the magnetization, M_eq is the magnetization at equilibrium and A is a constant which is dependent on the boundary condition for the experiments, which is 1 for 90-pulse and 2 for 180-pulse [57].

The other relaxation mechanism is the spin-spin relaxation, also called a transverse relaxation. This is more of an entropy process with the loss of phase coherence for the precessing nuclear spins. The main contributor to this relaxation process is the inhomogeneity in the magnetic field throughout the volume of the sample [58]. The time this process takes is defined as the time it takes for the spin to get back to its original phase:

$$\frac{M_x y'}{M_0} = e^{-\frac{t}{T_2}} \tag{3.10}$$

Here M_{xy} is the component of magnetization in the x-y-plane, M_0 is the magnetization right after the pulse at $t = 0$ [58]

The Impact of Relaxation Time on Line Broadening

The time of relaxation has a significant impact on the line width of the signal, where line width broadens as T shortens [58]. For liquid with low viscosity, T_1 and T_2 are both quite similar and relatively long, which shortens the width significantly. For high viscose liquids and solids (for which molecules have low mobility) T_1 tends to be very long and T_2 relatively short, caused by the large magnetic coupling to the spins nearby. The result is a broad signal. The relation between the half-height width of the peak and T_2 is described by:

$$\Delta\nu_{\frac{1}{2}} = \frac{1}{\pi T_2} \tag{3.11}$$

As mentioned in the introduction 1.2.2, NMR spectroscopy is a suitable method to use in the experiments in this thesis because ice is virtually invisible to the detector. Water, on the other hand, will be easily detectable. This is due to the ice signals' extremely long T_1 and very short T_2 [23]. This difference between water and ice signal has made it possible for NMR studies [23, 24, 32, 53] to detect traces of non-frozen water layers nearby the surface and in confined pores. It has also been found that the tightness of the bounding to the surfaces suppresses the freezing points as mentioned in 2.1. The T_2 values determine the tightness of associated water. Studies have found that for water, the presence of a surface will induce water molecules to exist in different states, thus showing different freezing behaviors [29, 32, 59].

3.1.3 The Spin-Echo Experiment

As mention in 3.1.2, the static magnetic field B_0 has an inherent inhomogeneity, contributing to a more rapid decay in FID signal and the nuclei to start precessing at different frequencies with a phase difference [60]. However, it is possible to recover and refocus the decayed FID signal and determine the T_2 values with the use of the spin-echo experiment [61], which has the pulse sequence:

$$90^\circ_{x'} - \tau - 180^\circ_{x'} - \tau\,(1st\,echo) - \tau - 180^\circ_{x'} - \tau\,(2st\,echo)....$$

First, a 90° excitation pulse shifts the magnetization from the z- to y-axis followed by a time period τ where the nuclei will start precessing at different frequencies due to the inhomogeneities in the magnetic field. A 180° pulse is then applied which inverts the phase differences resulting in a refocused echo with maximum signal intensity after the time τ, as seen in Figure 3.4. It is possible to induce several echo signals by repeating the spin-echo pulse sequence. However, the signal intensity of the echo will decrease for each spin-echo iteration due to the irreversible spin-spin relaxation [60].

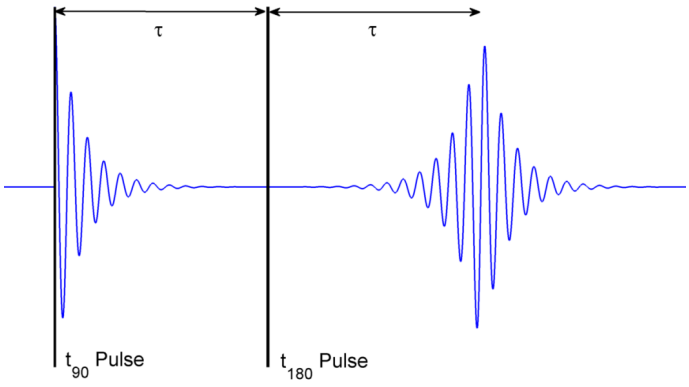

Figure 3.4: FID (blue line) in a spin-echo sequence. As seen FID decay with time τ, and refocuses at $2\tau.t_{90}$ and t_{180} (black lines) is the radio frequency pulse. Figure copied from [60]

3.1.4 Chemical Shift

The difference in frequency signals happens due to the variations of Larmor frequencies caused by the distinct chemical environment around each nucleus. This is called the shielding effect, which causes the nuclei to experience a weaker magnetic field than the externally applied field, measured and expressed as:

$$B_{eff} = B_0 - \sigma B_0 = (1 - \sigma)B_0 \tag{3.12}$$

Here B_{eff} is the effective magnetic field strength the nuclei are exposed to, B_0 is the actual field strength, and σ is the shielding constant. This shielding effect is highly dependent on the electron density distribution in the molecule affected by the chemical bindings, interactions within the molecule and the chemical surroundings [54].

As the magnetic field widely affects the Larmor frequencies, there is no given absolute x-axis across NMR instruments with different magnetic field strengths. Hence, the x-axis is given as a relative to a reference compound. The most commonly used reference compound for ^{1}H and ^{13}C is tetramethylsilane (TMS) which has twelve equivalent highly shielded protons. The reference compound is set to zero, whereas the sample values are relative to this point with a scale from right to left. The relative difference is minimal, measured in part per million (ppm) and usually termed as the chemical shift value. On this axis, signals with low chemical shift refer to signals of a nucleus with a higher shielding effect, whereas signals with higher chemical shift represent nuclei with more deshielding [62]. The chemical shift is given as [63, 64]:

$$\delta_{sample} = \frac{\nu_{sample} - \nu_{reference}}{\nu_{reference}} = 10^6(\sigma_{ref} - \sigma_{sample}) \tag{3.13}$$

The chemical shift is highly dependent on temperature, density, pressure, and concentration. For proton NMR, the appearance of hydrogen bondings is also a factor that impacts the chemical shift. This is because of the significant deshielding effect of hydrogen bondings, resulting in an upfield shift to high frequencies. The deshielding effect is due to the electrical

dipole field of the bonding, which is a more significant contribution than the enhanced density of electrons, having the opposite effect [65]. The relation between the amount of hydrogen bonding per molecule and the strength of the bondings to chemical shift was first worked out by Schneider and Pople [66]. Pure bulk water at 298K and 1 atm have a chemical shift (with HDW/LWD structure) at 4.60 ppm (relative to TMS) [67]. LDW, with an almost ice-like structure, has an ideal chemical shift at 7ppm and 1.1-1.7 ppm for water which mainly consist of HDW [29]. Temperature also changes significantly, affecting the number of hydrogen bonds and thus the chemical shift. Several studies have well documented the relation between chemical shift and temperature of pure bulk water to be 0.01 ppm/K [67] [68]. Higher temperatures favor the HDW with a highly mobile water structure, and thus more LDW at lower temperatures [29].

Chemical Shift Anisotropy

The distribution of electrons in molecules or through bondings is rarely distributed isotropically around the nucleus. Thus the shielding constant σ is impacted by the molecule's orientation relative to the external field and can be described as a tensor [69, 70]:

$$\sigma = \begin{pmatrix} \sigma_{xx} & \sigma_{xy} & \sigma_{xz} \\ \sigma_{yx} & \sigma_{yy} & \sigma_{yz} \\ \sigma_{zx} & \sigma_{zy} & \sigma_{zz} \end{pmatrix} \tag{3.14}$$

By the principal axis system (PAS), which is fixed on the molecule, this can be denoted as [69, 70];

$$\sigma_{PAS} = \begin{pmatrix} \sigma_{XX} & 0 & 0 \\ 0 & \sigma_{YY} & 0 \\ 0 & 0 & \sigma_{ZZ} \end{pmatrix} \tag{3.15}$$

The isotropic value of the isotropic shielding tensor, the anisotropy Δ, and asymmetry η can be given by [64, 69, 70]:

$$\begin{aligned} \sigma_{iso} &= \frac{\sigma_{XX} + \sigma_{YY} + \sigma_{ZZ}}{3} \\ \Delta &= \sigma_{ZZ} - \sigma_{iso} \\ \eta &= \frac{\sigma_{YY} - \delta_{XX}}{\Delta} \end{aligned} \tag{3.16}$$

Here, the shielding tensor σ_{iso} determines the center position of electron density, while the anisotropy Δ and asymmetry η determine the width and shape of the NMR spectrum [70].

The effect of different values of the principal components σ_{XX},σ_{YY} and σ_{ZZ} on line width can be seen in Figure 3.5 and 3.6.

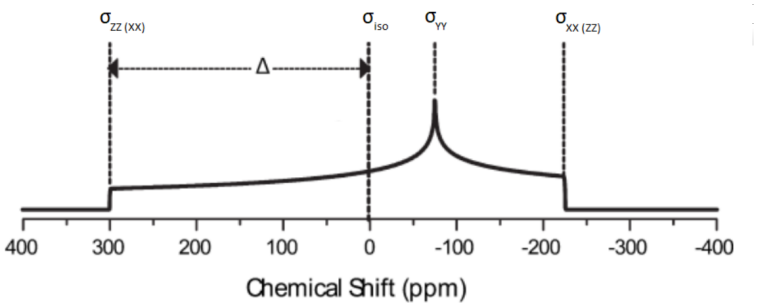

Figure 3.5: Shows the principal components (σ_{XX},σ_{YY},σ_{ZZ}) of the chemical shift tensor σ_{iso} and the anisotropic factor Δ on a chemical shift axis. Figure copied from [63]

When the electron density is equal in all directions, called spherical symmetry, the spectrum will shape as a narrow peak, as seen in Figure 3.6. This is the case for isotropic or anisotropic molecules with rapid tumbling motion, also termed Brownian motion. In samples containing solids or slow-moving molecules with anisotropic electron density, the different orientations of the molecules will result in a range of chemical shifts and thus a broader signal with axial symmetry or asymmetry [71, 72].

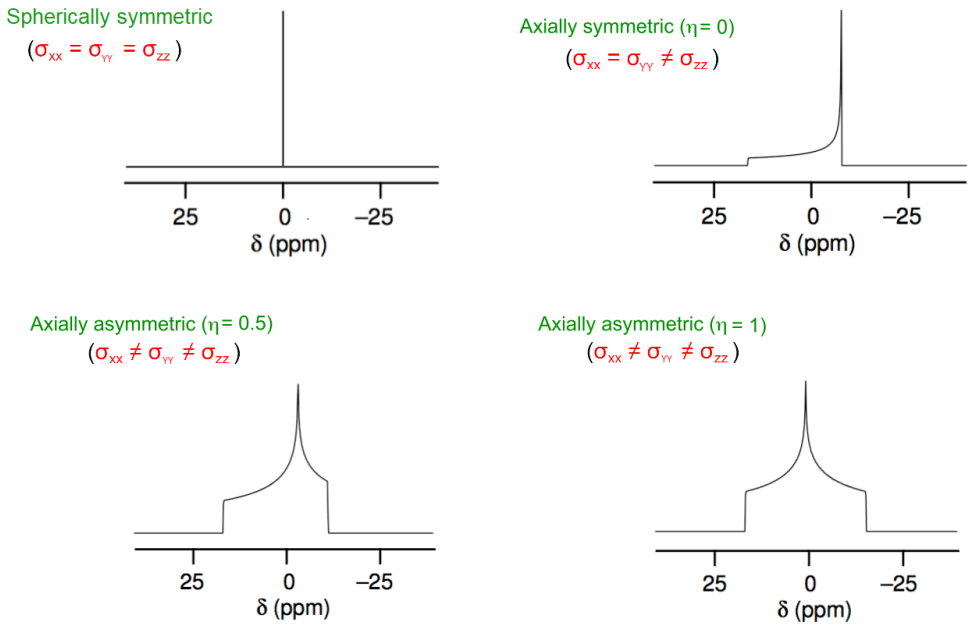

Figure 3.6: Shows the different shapes and symmetries of a signal in NMR spectra. Figure adapted from [73].

Chapter 4

Experimental Methods

This chapter describes the experimental equipment and procedure used in this thesis. This includes sections of sample preparation and washing procedures, procedures and equipment for investigating ice formation and wetting properties (including NMR-spectroscopy, freezing onset and contact angle measurements), and techniques used for roughness characterization (AFM and Bright-field microscopy).

4.1 Samples

4.1.1 Sapphire Samples

The experiments in this thesis were done on sapphire surfaces (Al_2O_3) supplied by MTI Corporation with following dimensions; thickness 0.5 mm, width 5.0 mm and length 10 mm. The sapphire samples have a crystal orientation (1-102), where Figure 4.1 shows the different orientations for sapphire. Each sample consists of two different surface finishes, one smooth epipolished side and one very rough side with no specifics provided by the manufacturer but appearing opaque. Figure 4.2 shows a picture of the samples used (middle and right).

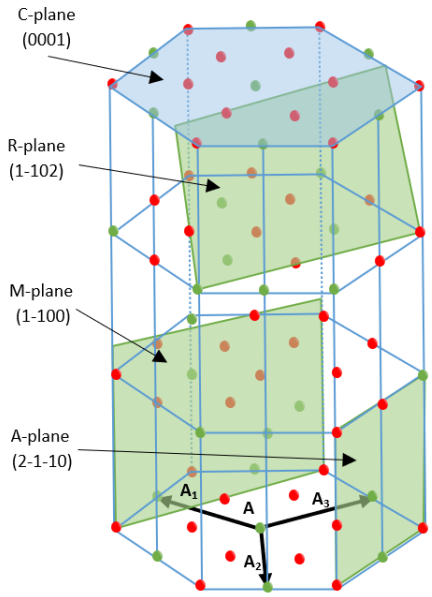

Figure 4.1: Figure shows the unit cell of hexagonal sapphire crystal structure. The red dots indicate oxygen atoms and green aluminium. The different crystal planes are pointed out, where the C-plan orientation is the most common for sapphire. The samples used in this thesis is cut through R-plane. Redrawn from [74]

4.1.2 Silica Samples

Amorphous silica (SiO_2) glass plates with smooth surface finish were added as samples in this thesis, as a reference, due to the challenges with the NMR setup as described in section 4.3. Figure 4.2 show a picture of such a silica plate (left). The silica plate had the following dimensions; thickness 0.1 mm, width 5.0 mm and length 12.0 mm

Figure 4.2: Picture of the different sample surfaces used for measurements in this thesis. Smooth silica (left) with thickness 0.1 mm, width 5.0 mm and length 12.0 mm. Smooth sapphire (middle) and rough sapphire (right) with thickness 0.5 mm, width 5.0 mm and length 10 mm.

4.2 Sample Preparation

4.2.1 Washing procedure

Three different washing regimes have been used throughout this project. They will be referred to as: Loosely washed, washed, and washed and etched. Loosely washed means that the samples have not been washed directly before every measurement. Instead, the samples have been washed with isopropanol and stored in a plastic holster between measurements. Samples were always handled with gloves and tweezers. Washed samples have been cleaned with isopropanol and dried with N_2 directly before measurements. The procedure for washed and etched samples are described in the section below.

Washed and Etched Samples

The following procedure for washing and etching samples was used for some freezing onset measurements in addition to the AFM measurements and performed with guidance from Espen Werdal Selfors:

- Samples were soaked in 2M HCl solution in a beaker and placed in an Ultrasonic Cleanser 180W for 10 minutes. Samples were then rinsed with water and dried with N_2.
- Samples soaked a second time, this time with acetone, and placed in the Ultrasonic Cleanser for 10 minutes. Samples were then dried with N_2.
- Samples were dry-etched using the Plasmatherm 790+ instrument, applying reactive ions of O_2 to remove impurities.

4.2.2 Double plate samples preparation

In this thesis, two different sample plate arrangements were used: water droplets on a single sample plate and water in between a double set of sample plates. The double sample plate arrangement was prepared as follows:

Two droplets of deionized water were placed on the surface of one sample plate using a syringe or 1-10 µL Eppendorf micro-pipette with Finntip 10 (0.2-10 µL). The total water volume between the plates was 1.2 ± 0.4µL measured by using an analytical balance scale based on the average of 20 measurements. Another sample plate with the same surface material and structure was placed on top of the humidified sample using tweezers. This so that the water was in between two surfaces with the same roughness. A double sample plate can be seen in the Figure 4.3.

(a) Two Sapphire Samples (b) Sample with droplets (c) Dobble Plate Sample

Figure 4.3: Procedure of making the double plate samples

4.3 NMR Setup and Procedure

4.3.1 NMR-Setup

NMR-spectrometer

The spectrometer used for recording NMR-spectra was a Bruker BioSpin 500 MHz wide-bore spectrometer installed in 2015 and located at the chemistry department at Realfagsbygget. Figure 4.4a shows a picture of the spectrometer. This spectrometer is used for solid-state NMR, micro imaging and diffusion. For the solid-state NMR the spectrometer has both a magic angle spin (MAS) probe head and a flat-coil probe head; the latter is used in this thesis. The spectrometer is connected to a console, amplifier and chiller, and uses the software TopSpin 3.6.2 to control the instrument and to process and analyse the measurements. A schematic drawing of the setup can be seen in Figure 4.4b

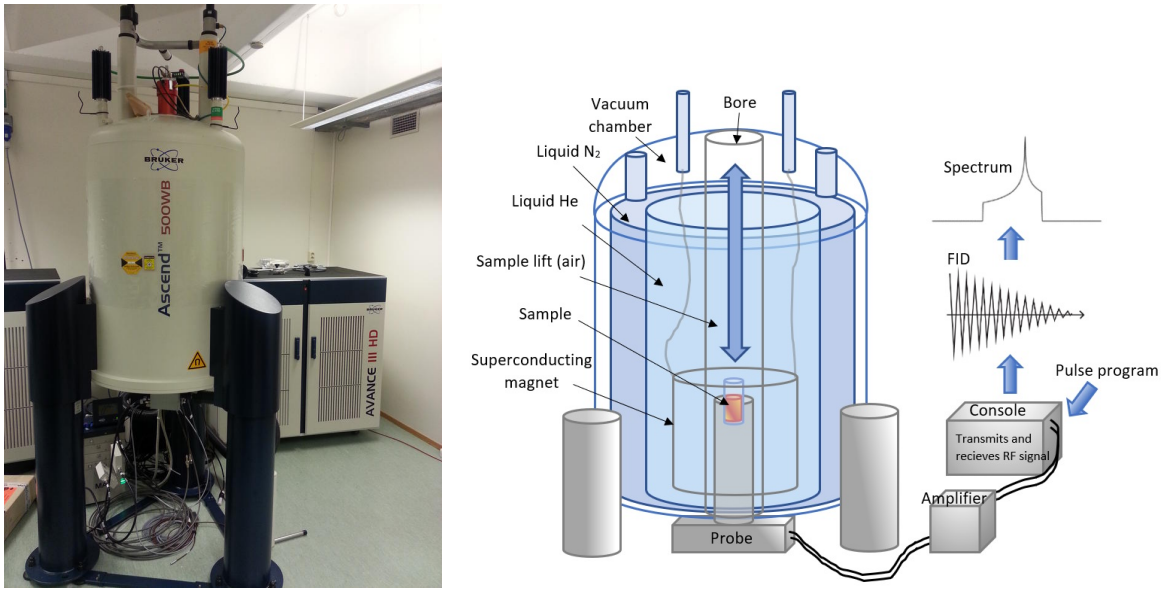

(a) NMR-spectrometer

(b) NMR set-up

Figure 4.4: a) Picture of Bruker BioSpin 500 MHz Wide Bore spectrometer used in this thesis. Picture copied from [75] b) Schematic drawing with the main parts of the NMR-spectrometer setup. The sample is placed in the probe, which is inserted into the spectrometer. The superconductive magnet surrounds the probe located in a chamber of liquid Helium. Outside the Liquid helium is the liquid nitrogen, followed by the vacuum chamber. The spectrometer is connected to an amplifier and console, transmitting and receiving signals. Figure inspired by [76]

Flat-coil Probe Head

The flat-coil probe head is rare and custom-made, where the design of the coil is rectangular shaped rather than the standard spiral, as can be seen in Figure 4.5b. This unique coil design allows it to contain larger horizontally positioned samples, thus making it a good candidate for the silica and sapphire samples in this thesis that would not fit in other sample holders. This probe head provides three resonances and can be used for ^{1}H, ^{13}C and ^{15}N with a ^{31}P switch.

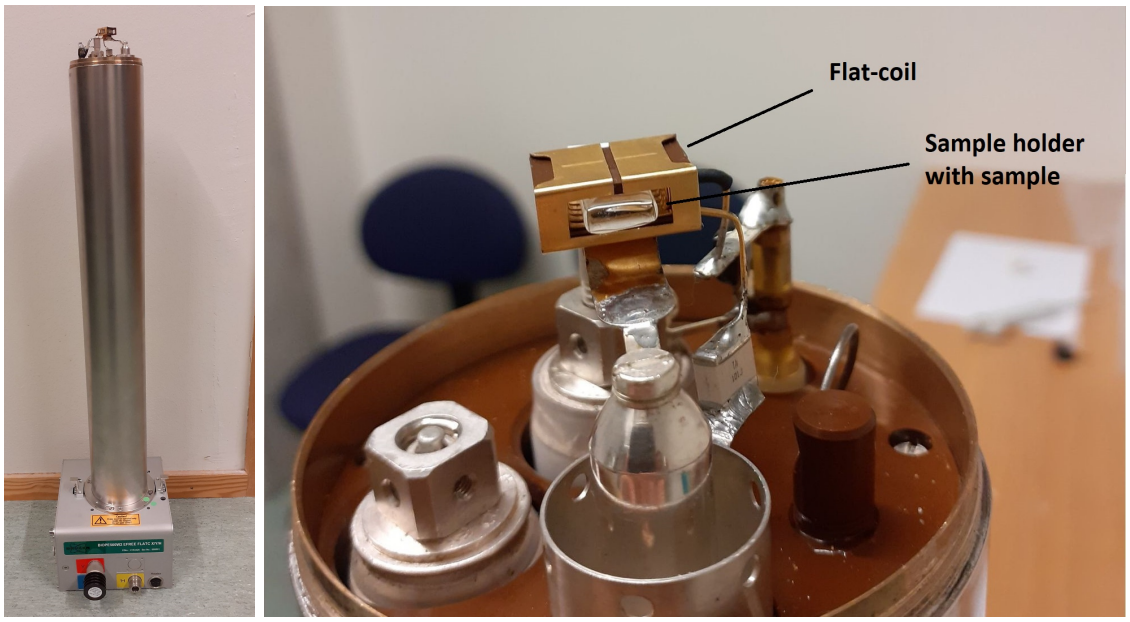

(a) Full size (b) Close-up

Figure 4.5: a) Picture of the flat-coil probe head. Additionally it has a cover to the sample stage top b) Close up picture of the flat-coil and sample holder.

Sample Holder

The sample holders used to fit the flat-coil probe head were made of quartz (SiO_2) and can be seen in Figure 4.6. These were plugged using parafilm or 3D printed corks made at UiB, as described in section 4.17b.

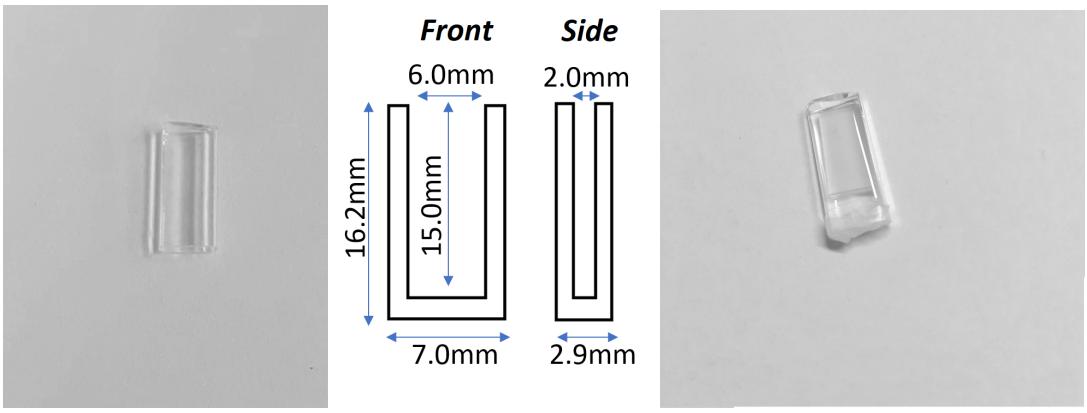

(a) Sample holder (b) Dimensions (c) With sample

Figure 4.6: a) Picture of a quartz sample holder, with one closed and one open end. b) Schematic drawing of the sample holder with dimensions c) Quartz sample holder with a double plate sample with water and covered with parafilm

VTU- Temperature Controller

The spectrometer is connected to a chiller and a temperature sensor in the probe head near the sample holder, making it possible to regulate the temperature around the sample with the VTU temperature controller. The sample temperature is regulated by the system using a temperature-controlled airflow blown through a hose to the probe head, which is located directly beneath the flat-coil containing the sample. A temperature sensor is located near the coil as either the brown or metallic part seen in Figure 4.5b.

4.3.2 Procedure for Recording Spectra

The sample holder with a sample, prepared as described in Section 4.2.2, was positioned in the flat-coil probe head and then placed in the NMR spectrometer. The shimming coils near the sample were then adjusted to ensure homogeneous magnetic irradiation on the sample, resulting in a shimming file containing the optimised shimming parameters, which is applied for all the samples. The temperature regulator was turned on, followed by an up to 20-minute wait for temperature and wobble to stabilise. To optimise the efficiency of the radio frequency pulses and to maximise sensitivity, a matching and tuning process was done by manually adjusting two tuning wheels on the spectrometer and using the wobble functionality in TopSpin. The recording of the signal was then initiated with a command using Topspin. This results in a recorded FID signal, which is converted to a spectrum using Fourier transformation (see Equation 3.8).

4.3.3 Choosing pulse program and Optimizing Parameters

The first spectra were recorded at room temperature using a regular one-pulse 90 pulse program to test the system. A schematic drawing of this pulse program can be seen in Figure 4.7a. However, these spectra revealed a significant amount of background noise combined with a weak water signal, as seen in Figure A.1 in Appendix A.1. Several hypotheses were investigated to locate and thus remove the noise and to enhance the signal intensity. This included changing the metal syringe to a micro-pipette with a plastic tip and filling the sample holder with bulk water samples, with and without plates and with different shimming parameters. At some point silica plates were introduced as a more known material for comparison. The eventual solution to filter out the broad signal from background noise was to shift to a spin-echo program shown in Figure 4.7b and use a T_2-filter. The T_2-filter remove signals with line-widths according to Equation 3.11 and Equation 3.10, as seen in Figure A.2. This pulse program and T_2-filter were used for all the results presented in this thesis.

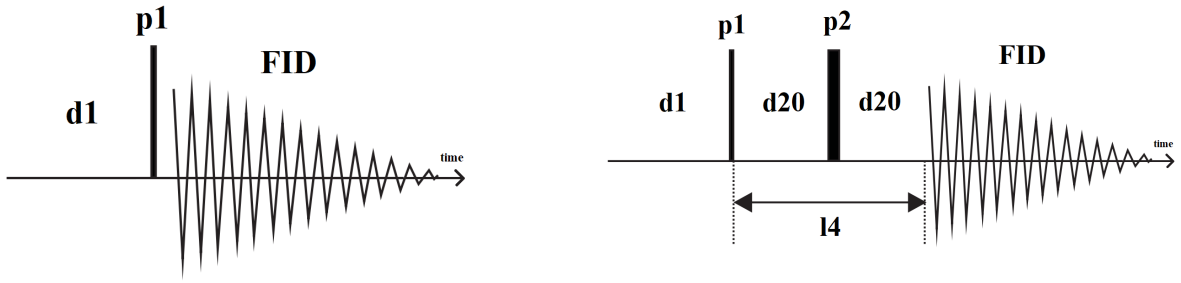

(a) One-pulse program

(b) Spin-echo pulse program (cmpg1d)

Figure 4.7: Schematic drawing of one-pulse (a) and cmpg1d (b) pulse program. Here p1 is pulse length (90°), p2 pulse length (180°) d1 relaxation delay time, d20 fixed echo time, L4 a loop. Figures copied from [77]

To optimise the parameters used in the spin-echo program and to ensure reproducibility and control over the system, a number of preparatory recordings were performed. Ten recordings were done over time at room temperature for each of three samples per surface, half of the recordings using the spin-echo pulse program and the other half using the one-pulse program for comparison. The parameters were optimised using recommended values given by the Topspin software. Table 4.1 presents the final spin-echo parameters used for the results presented in this thesis.

Table 4.1: Parameters used for cmpg1 pulseprogram

Parameter	Explantion	Value
l4	loop counter	4
D1	Relaxation delay	6
D11	Delay of disk	$3 \cdot 10^{-3}$
D20	Fixed delay	$1.25 \cdot 10^{-4}$
DS	dummy scans	16
ns	number of scans	64
rg	receiver gain	203
TD	size of FID	16K

4.3.4 Freezing out layer by layer measurements

Freezing out layer by layer measurements were performed on the samples by decreasing the temperature step-wise until freezing occurred, observed by the absence of a water signal in the spectrum, as mentioned in Section 3.1.2. A waiting period of approximately 20 minutes was introduced at each temperature step to ensure that the sample temperature had stabilised, followed by the matching and tuning process and recording of the signal. However, the 20-minute waiting period for each temperature step made each sample recording very time-consuming. A temperature calibration 4.3.6 was performed later, showing that the waiting time could be reduced to 10 minutes without any significant impact on the recorded spectra.

The initial plan was to come as close to the freezing point as possible to investigate the freezing process with incremental decreases in temperature. Starting with a significant temperature drop near the expected freezing range and continuing with small intervals until freezing. The lowest temperature interval possible with the NMR spectrometer was $0.5K$, with a possible interval overlap due to the calibration uncertainty of $\pm 1K$. However, the combination of the substantial time consumption of each temperature step and the challenge of predicting the actual freezing ranges resulted in differences in temperature intervals and the number of recordings for each sample. The exact intervals and temperature steps used for the recorded spectra can be seen in Appendix A.2 Figure A.4.

Flushing

After performing many sequences of freezing out layer-by-layer experiments, the temperature sensor started showing minor fluctuations of around $\pm 1K$. It was suspected that this could result from condensing in the piping or chamber caused by the numerous cooling and heating cycles. The mitigating measure for this matter was to run a flushing process to dry the pipes and chamber.

4.3.5 Bulk Water Measurements

Several recordings were made of bulk water samples, initially concerning the investigation of background noise mentioned in Section 4.3.3. Later recordings of bulk water samples were used as a known reference and for calibration of the chemical shift axis due to the drift in the magnetic field occurring in solid-state spectrometer experiments.

The water samples were made by filling the quartz sample holder with deionised water using an Eppendorf micro-pipette. The sample holder was sealed using the 3D printed corks described in section 4.17b and with parafilm to fasten the cork to the sample holder to avoid leakage and evaporation.

For the samples used as a reference for calibration, the same spin-echo parameters shown in table 4.1 were used, but with fewer number of scans than the rest of the recorded spectra. A new shimming file specifically made for the bulk water samples was used in addition to the regular shimming file.

4.3.6 Temperature Calibrations

During the project, it became evident that a temperature calibration of the flat-coil probe head was necessary, initially presumed done by the manufacturer. The calibration can be done by measuring the chemical temperature of a medium inside the probe head, thus obtaining a more realistic temperature measurement than from the sensor, which only measures outside the coil as described in 4.3.1. Pure methanol was considered a suitable calibration medium based on the temperature ranges used in this thesis.

A sample holder was filled with pure methanol using an Eppendorf micro-pipette and sealed with a 3D printed cork (4.17b) and parafilm. Spectra were recorded at various airflow temperatures as measured by the sensor, given in Table 4.2. Recordings for each temperature point were done after a stabilisation period of 10 minutes but deliberately increased to 20

minutes for a few recordings to check if an increased duration had an effect. The temperature measurements on pure methanol were performed several times on two different samples to ensure accurate calibration, whereas one of the spectra is shown in Figure 4.8. The temperature calibration was done with the guidance of Josè C. R. Guerrero.

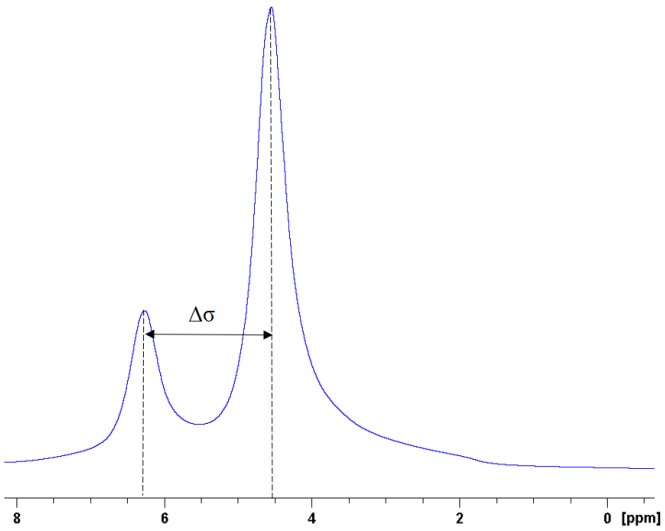

Figure 4.8: ^{1}H-NMR spectrum of pure methanol recorded at 275K measured by the temperature sensor. As the $(\Delta\sigma)^2$ is very small, the temperature is approximated to be linear between the points.

Based on the recorded spectra, the exact temperature of the methanol at a given sensor temperature can be obtained by measuring the chemical shift distance between the peaks in the methanol spectrum, as seen in Figure 4.8. The relation between the chemical shift distance of the methanol peak ($\Delta\sigma$) and the temperature of pure methanol is described as:

$$T(K)(Methanol) = 409.0 - 36.54\Delta\sigma - 21.85(\Delta\sigma)^2 \tag{4.1}$$

Table 4.2: Results of temperature calibration of flat-coil probe head using pure methanol, based on equation 4.1. The uncertainties come from manually measured distances.

Temperature	Calibrated temperature
298 K	295 ± 1K
275 K	286 ± 1K
265 K	275 ± 1K
255 K	267 ± 1K
245 K	261 ± 1K
235 K	252 ± 1K
220 K	239 ± 1K

4.3.7 Recording of Background Signal

As mentioned in Section 4.3.3 the first one-pulse experiments revealed a significant background signal, as seen in Appendix A Figure A.1. The proposed solution was to switch to a spin-echo pulse program with a T_2-filter that removes the broader signal. However, even with the T_2-filter, the background signal did not disappear entirely in the spectra. Several experiments and tests were done to locate the source of the background signal.

Initially, three tests were performed; One on dry silica plates, one with the probe and sample holder and one with only the probe. The findings from these recordings were that the primary background signal seemingly came from the probe head itself.

Another experiment was performed to check if the background signal could have a temperature component. A sample of dry sapphire plates was recorded with a gradually lower temperature. These recordings showed some temperature dependencies from room temperature until 273 K, otherwise insignificant changes to the background signal. However, some minor changes in phase and chemical shifts could be observed.

When proceeding with the NMR recordings in the project, there were indications of the background noise showing a slight change over time. Further investigations were initiated to find other factors potentially contributing to the background noise, including the cork and parafilm. A number of recordings were made with a wide variety of set-ups and temperatures:

- Probe, holder filled with parafilm
- Temperature dependence of the same sample
- Probe with holder and dry plates and parafilm on edge
- Temperature dependence of parafilm on edge
- Probe with holder and parafilm on edge
- Temperature dependence of the same sample
- Probe with holder
- Temperature dependence of the same sample
- Probe with holder and cork
- Temperature dependence of the same sample
- Probe with holder, cork and dry plates
- Temperature dependence of the same sample

After these tests, it was decided to record background spectra with temperature variations on the same days as the primary spectra recordings using the same amount of parafilm, and carefully position the sample holder in the flat coil to ensure similar conditions. These spectra were used to subtract the background noise from the NMR spectra using the Topspin software, as described in Appendix B.1.2.

4.4 Freezing Onset and Contact Angle Measurements

4.4.1 Contact Angle Goniometer: Dataphysics OCA 20L

A contact angle goniometer, Dataphysics OCA (Optical contact angle) 20L, was used to measure contact angle and freezing onset. The goniometer consists of a CCD camera, a sample stage with an adjustable temperature plate, a light source, and an adjustable syringe, as shown schematically in Figure 4.9a. A temperature chiller and heater are connected to the instrument, making it possible to adjust the plate temperature. Figure 4.9a shows the actual instrument used in this thesis, which was moved from a standard lab room to a semi-clean room located at the NANOLab at UiB during the project to prevent potential sample impurities and ensure better humidity control. The instrument and measurements are controlled and analyzed by the Dataphysics SCA 20 OCA Control Software.

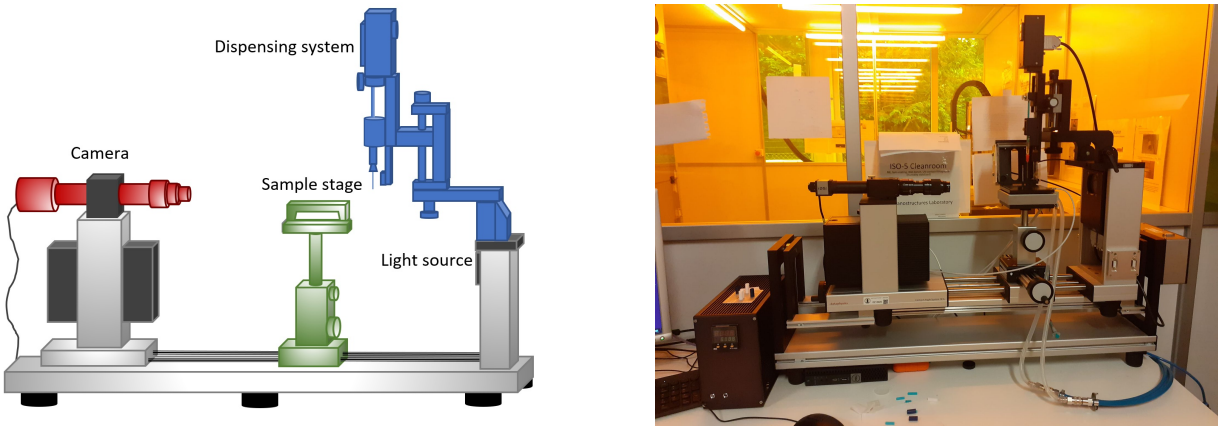

(a) OCA-setup

(b) Contact angle goniometer

Figure 4.9: a) Schematic illustration of OCA setup redrawn and adapted from [78], b)picture of the Dataphysics OCA 20L instrument used in this thesis

4.4.2 Freezing Onset Measurements

The freezing onset temperatures were measured by lowering the temperature for the droplets on the sample surfaces until freezing occurred. The sample was placed on the sample stage, followed by adding a 2 µL droplet of super distilled water. The CCD Camera was manually adjusted with focus, zoom, and light settings before recording a video with tracking of contact angle and temperature measurements. The temperature started at 20 °C s^{-1} and was gradually reduced with 0.16 °C s^{-1} until observed freezing of droplet. The freezing point could be easily observed due to changes in optical transparency, contact angle, and droplet shape. Before freezing, the droplet will appear transparent. As ice embryos start to form, the droplet is heated adiabatically, resulting in a mixture of water and ice in the droplet, thus reducing its transparency [4], as seen in Figure 4.10. This first stage of the freezing process, the freezing onset, only lasts a few milliseconds before the second stage of complete freezing. In this last stage, the rest of the water freezes in an isothermal process [4]. The droplet loses the rest of its optical transparency and changes form into a tip point shape,

as seen in the Figure 4.10. The complete freezing can also be observed in the contact angle measurements with a sudden increase in contact angle, followed by a substantial drop.

The freezing onset measurements in this thesis were performed on samples with different preparation regimes, humidity conditions, and environmental exposure (semi-clean lab/standard lab). There were three preparation regimes; unwashed, washed with isopropanol and dried with N_2, and washed with included etching as described in section 4.2.1.

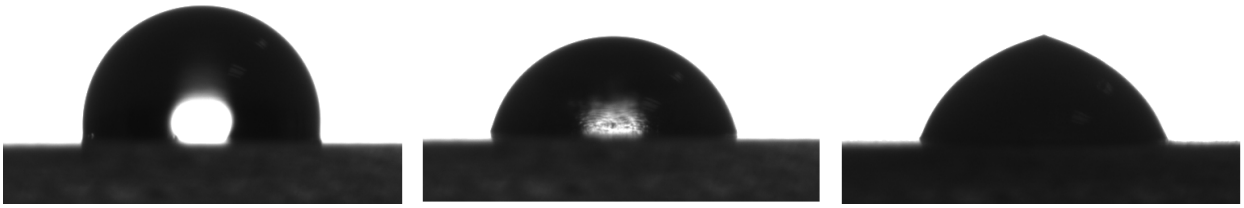

(a) Before freezing (b) Freezing onset (c) After freezing

Figure 4.10: Example of freezing prosess of a 2 µL droplet on surface

Freezing Onset on Double Plate Samples

Freezing onset measurements were also performed on the double plate samples as described in section 4.2.2. The temperature was then gradually lowered, following a similar procedure as for the single droplet freezing measurements. As there is no contact angle with this sample set-up, only the temperature was measured until freezing was observed through the CCD camera. The freezing point was observed by the sudden loss of optical transparency and water spilling out on the sample edges due to volume expansion.

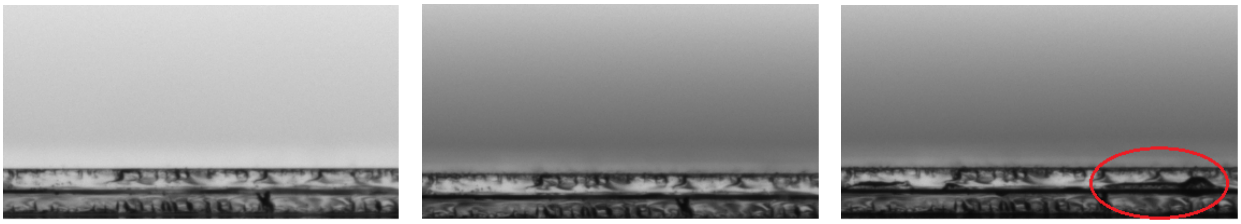

(a) Before freezing (b) Freezing onset (c) After freezing

Figure 4.11: Example of freezing prosess of 1.2 µL water on double plate samples

4.4.3 Contact Angle Measurements

Static Sessile

The water droplet's static contact angle was measured before each freezing onset experiment. A droplet of 2 µL was added to the sample as described in section 4.4.2. The baseline and curvatures were adjusted accordingly before the SCA 20 software calculated the contact angle. This method presumes a stable deposition of the droplet. In reality, local and global energy differences will cause it to be meta-stable [35], as described in section 2.2.1. Hence the static contact angles are not necessarily reproducible.

Advancing and Receding Contact Angle

The contact angle hysteresis of water on different surfaces is found by measuring the receding (RCA) and advancing (ACA) contact angle. As described in section 2.2.1, this is the highest and lowest contact angle within the hysteresis and is reproducible. These two contact angles can be found by measuring contact angles while increasing and reducing the droplet volume on the surface, as illustrated in Figure 4.12. To be able to reach the contact angle hysteresis' maxima and minima, the baseline must extend and retract according to the change in volume [35], as seen in the figure.

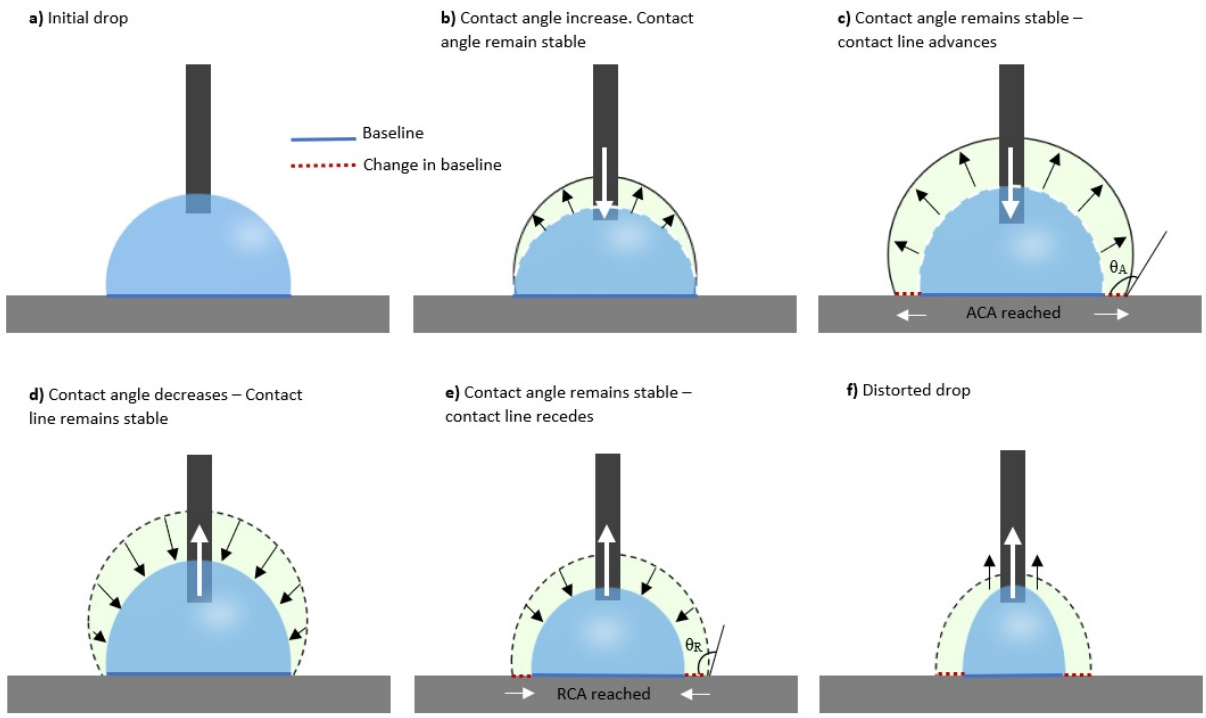

Figure 4.12: The measuring process for advancing (ACA) and receding angle (RCA). a) Initial drop with syringe inside b) Adding water to the droplet increases the contact angle while the baseline remains stable. c) As ACA is reached, the contact angle remains stable while the baseline extends. d) Removing water from initial drop before conducting RCA measurements. The baseline remains stable. e) Contact angle remains stable, and the baseline is shortened as more water is removed from the droplet. The RCA can be measured. f) Further removal of water from the droplet distorts the droplet shape. Figure redrawn from [35]

The following procedure, from the article by Huhtamäki et al. [79], was used to measure the advancing contact angle of the water droplet:

- A 2 µL droplet was lowered to the stage, with the needle left halfway into the droplet. The needle was positioned in the center of the droplet, secured by camera in x-direction and on eye-sight in y-direction.

- 1 µL of water was dispensed with flow rate 0.10 µL/s until reaching 3 µL. The flow rate was 0.05 µL/s in the study, but 0.10 µL/s was applied due to the minimal flow rate limitations of the apparatus. The low flow rate was to prevent potential dynamic effects of the liquid.
- Waited for 30 seconds to secure equilibrium before starting the video recording.
- Dispensed 8 µL with flow rate 0.10 µL/s.
- Stopped the video recording before analyzing the data.

The following procedure, from the same article [35], was used for measuring the receding contact angle:

- A droplet of 30 µL was dispensed onto the sample with a flow rate of 2 µL/s. In the article procedure, the start volume should be a minimum of the decided volume from the figure. However, the samples could not contain more than 30 µL due to the sample size limitation. The needle is positioned in the middle of the droplet and left inside, as close to the solid surface as possible.
- Removed water with flow rate 2 µL/s until the droplet was 13 µL of size. Checked and adjusted needle position if necessary.
- Additional 2 µL was removed with a flow rate of 0.10 µL/s
- Waited for 30 seconds to secure equilibrium before starting the video recording.
- Withdraw water with a flow rate of 0.05 µL/s, until completely removed.
- Stopped the video recording before analyzing the data.

For the measurements to reach the minimized contact angle of the hysteresis, it is crucial to start with a large enough water volume. The size of the droplet is determined by the advancing and receding contact angle as found in figure 4.13

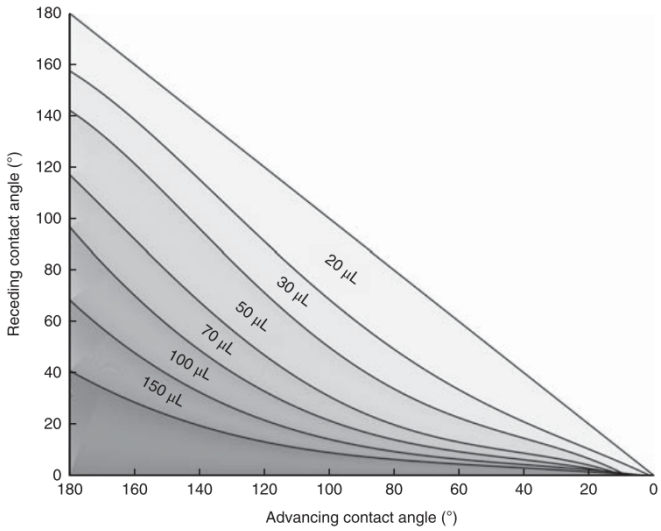

Figure 4.13: Recommended values for droplet starting volume for the RCA measurements. Volume was decided based on estimated ACA and RCA values. Figure copied from [35]

The measuring of advancing and receding contact angles were performed three times for each sample in different areas on the sample surface, all washed with isopropanol and dried with N_2.

4.5 Atomic Force Microscopy

An Atomic Force Microscopy (AFM), shown in Figure 4.14, was used to study and measure the topography of the surface samples in this thesis. This microscopy method can determine the roughness characterisations and provide a high-resolution three-dimensional image of the surface topology.

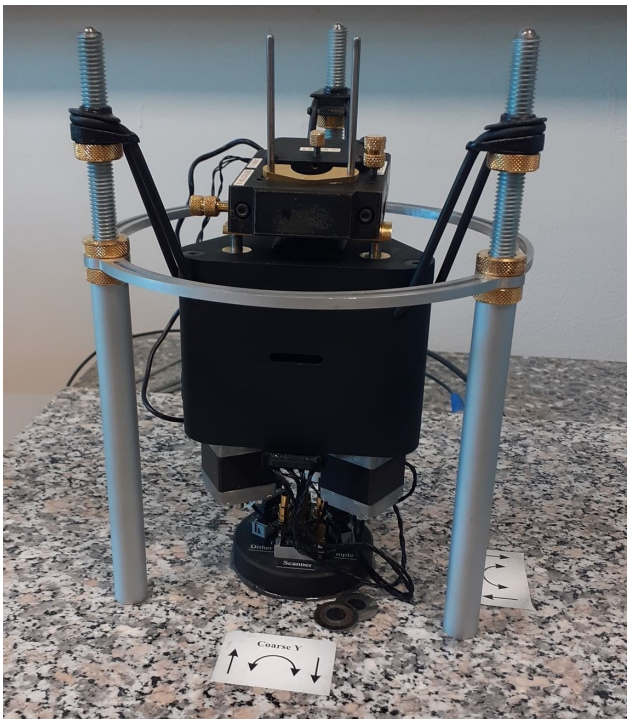

Figure 4.14: Picture of the AFM instrument "Eddy" from Anfatec, used in this thesis

A schematic drawing of the basic principles is shown in Figure 4.15. The sample surface is scanned using a very sharp probe tip (approx. 10-20 nm in diameter), either in contact (static mode) or close to the surface (dynamic mode), that is moved systematically across the surface topology [80]. The probe tip is attached to a cantilever with a given stiffness which will elastically bend when the probe tip encounters surface height variations (z-axis) due to the near-field forces interacting between the tip and the surface. When the cantilever bends, a laser beam pointed at a reflecting area on the cantilever will deflect accordingly and be recorded by a photodiode sensor. A feedback loop uses the detected z-axis position to continuously adjust the probe tip to maintain the correct distance to the sample surface. A three-dimensional image of the surface topology can thus be obtained by combining the z-axis displacement with the given y- and x-axis positions from the AFM scanner [81].

The AFM in this thesis was performed with the guidance of Espen Werdal Selfors, using a dynamic tapping mode with a CSC17 probe tip. In this tapping mode, an oscillating cantilever vibrates the probe tip near the surface, slightly making contact before rising again. When the probe tip encounters surface height variations, the near-field forces between the tip and the surface will shift the cantilever's oscillation frequency. This frequency shift is then used in the feedback loop to adjust the distance between the probe tip and sample surface and maintain the oscillation frequency. The surface topology is analysed using the detected amplitude loss, equivalent to the energy loss caused by the forces between the surface and probe tip. The data retrieved from the AFM were then analysed using the AFM software Gwyddion.

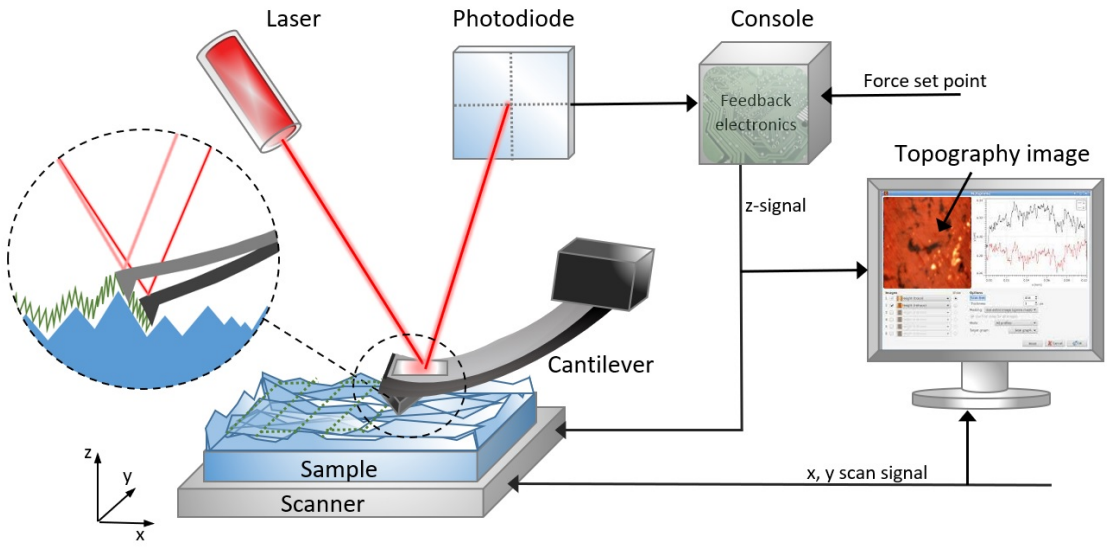

Figure 4.15: A schematic drawing showing the basic principles for Atomic Force Microscopy. The sample surface is scanned systematically in a given x- and y-direction using a sharp probe tip on a cantilever. The cantilever moves in z-directions according to the mode (static or dynamic) given as input from the feedback electronics. The cantilever bends according to the surface topography and deflects a laser beam detected by a photodiode and translated to a z-signal. The Gwyddion software combines the x-, y-, and z-signals to generate a topography image. Figure inspired by [81]

.

4.6 Bright-field Microscopy

Bright-field microscopy is a quick and straightforward method to investigate samples. A Nikon Eclipse LV100ND microscope was used in this thesis to examine the samples for potential impurities and effects of the cleaning procedure before conducting the freezing experiments in the cleanroom. The microscope has two objective lenses, whereas the LU Plan Flour 20x/0.45 was used in this thesis. It is possible to retrieve high-resolution surface images using the Nikon camera head (DS-Fi2) and stand-alone control unit (DS-L3) connected to the microscope. Figure 4.16a shows a picture of the microscope with descriptions of the different components, and Figure 4.16b shows a schematic drawing of the basic principles of bright-field microscopy.

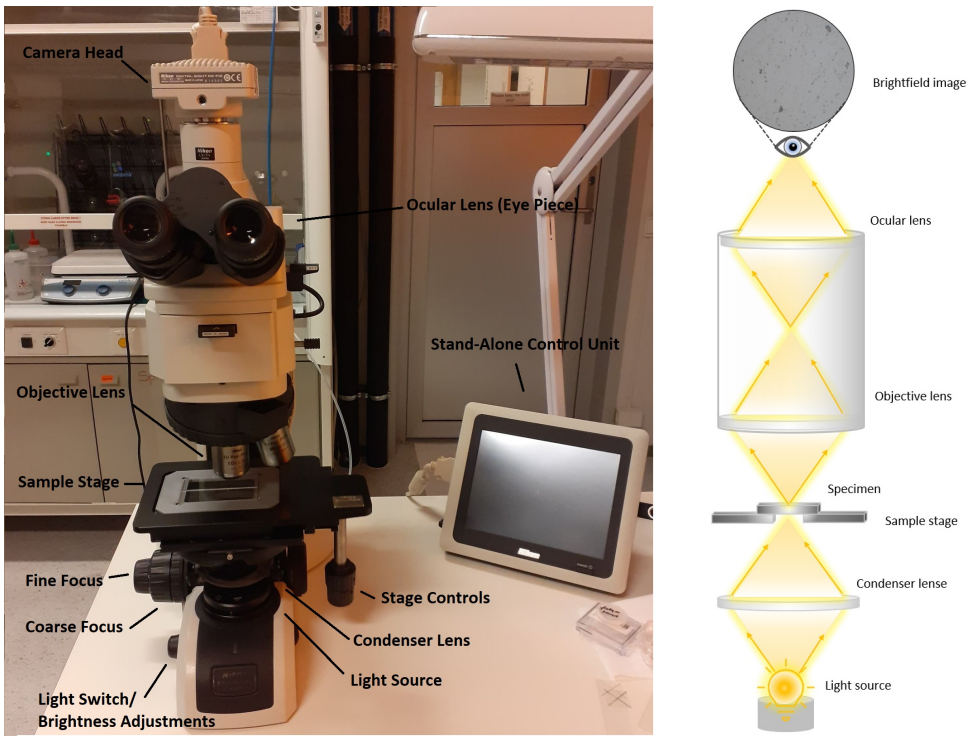

(a) Bright-field Microscope (b) Basic Principle

Figure 4.16: a) Picture of the Nikon Eclipse LV100ND microscope used in this thesis, with the connected DS-Fi2 camera head and DS-L3 Stand-alone control unit. b) is a schematic drawing of the basic principle behind the bright-field microscopy. The light path starts at the light source travelling through the conductor lens, focusing the light onto the sample. The objective lens collects and magnifies the transmitted light from the sample, while the ocular lens focuses the light so it can be observed with the eyes. The contract in the observed image is generated by the absorption of light in dense areas in the sample.

4.7 3D Printer

The corks used in some of the NMR experiments (described in subsection 4.3.5 and 4.3.6) were designed in Creo software and printed in plastic material with the 3D printer seen in Figure 4.17, performed with guidance of Sabrina Daniela Eder. Three cork sizes were made with a difference in height on inner part (2mm, 1.5 mm, and 1 mm). The corks were finished by manual filing of the inner parts.

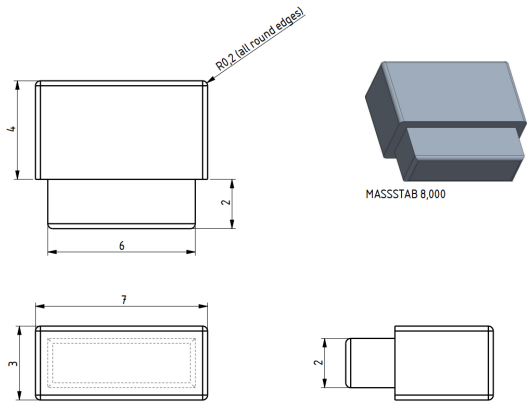

(a) Design and dimensions (units in mm)

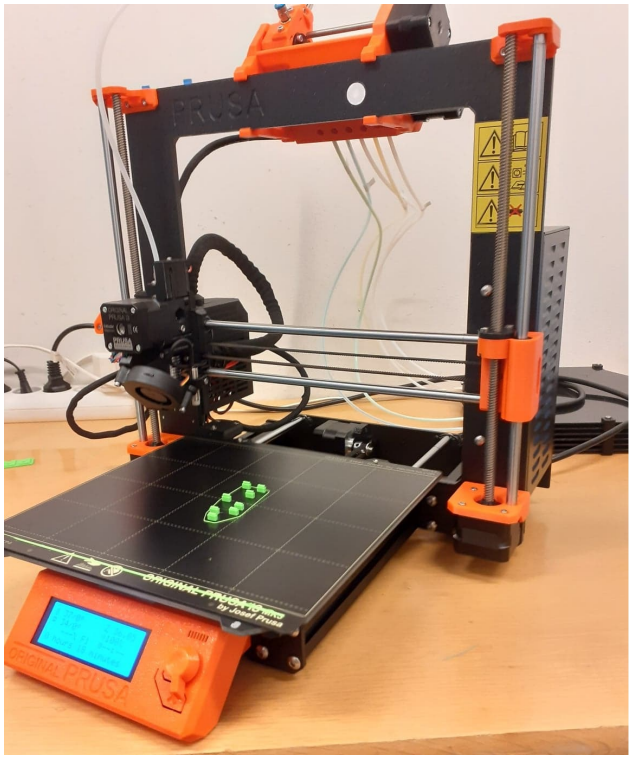

(b) 3D-printer

Figure 4.17: a) shows a schematic drawing of the designed cork with dimensions (units in mm). This Figure show the longest cork, the two others have the same dimensions besides the height of the inner part which where 1.5 and 1 mm. Drawing is design by Sabrina Daniela Eder. b) picture of the 3D-printer, while printing the corks.

Chapter 5

Results and Analysis

This chapter presents and analyses the results of the measurements and experiments performed in this thesis. The results include the surface characterisation using AFM and BF microscopy, wetting experiments using NMR and contact angle measurements, and freezing experiments with NMR and freezing onset measurements.

5.1 Surface characterization

The topography for the three surfaces in this thesis has been investigated using AFM to define the roughness and curvature radiuses as described in section 4.5. These results are essential in the widely debated matter of roughness impact of the surface freezing properties. Thus, important when interpreting the freezing temperature measurements. The surfaces have been measured for both loosely washed (LW) and washed and etched (WE) samples, and the results are presented in Figures 5.1-5.3 and roughness parameters in Table 5.1.

Figure 5.1a and 5.1b show the topography of the rough sapphire samples, which have an overall roughness RMS of 120 nm (LW) and 180 nm (WE), as presented in Table 5.1. The roughness RMS, measured on a small surface area on the AFM images, thus show a higher roughness for the WE sample than for the LW sample. This could be due to local texture differences or larger pits introduced in the etching procedure. The amplitude plots in Figure 5.1c, and 5.1d show the complexity of the surface texture with high- (roughness) and low-frequency (waviness) components, as opposed to an ideal fabricated surface, having structured pits and bumps of the same size.

The smooth sapphire and silica surfaces have very small RMS values with nanoscale roughness and are significantly flatter than the rough sapphire. Thus the impact of the low- and high-frequency texture components is not as significant for these surfaces. However, the AFM images and amplitude values show that cleanliness impacts both the overall and local roughness, as can be observed especially in Figure 5.2 a-d.

Figure 5.4 shows the proportion of positive curvature (indication of pits), negative (bumps) and neutral (flat) based on the curvature analysis of the AFM images. The smooth silica shows the smallest proportion of pits, while both sapphire samples show a similar distribution. Meaning that the areas covered with pits and bumps are nearly identical for rough and smooth sapphire but with a much smaller amplitude for smooth sapphire, as seen in Figure

5.2 (c-d) and 5.1 (c-d). Rough sapphire (WE) has a slightly smaller proportion of pits, which could be local differences or a result of etching, as mentioned above. Figure 5.1e-f,5.2e-f and 5.3e-f show the proportion of curvature radius of the pits.

According to CNT, only curvature radius below $10r_c$ affects the freezing temperature. The critical radius of an ice embryo is calculated to 2.2 nm at (253 K) and 4.5 nm at (263 K) (see calculations in Appendix B.3.2), corresponding to a $10r_c$ of 22-45 nm. However, as may be observed for all the surfaces (except smooth silica (WE)), most of the positive curvature radii far exceed this radius. Smooth silica (WE) shows a higher proportion of smaller curvatures, but as seen in 5.4 the proportion of pits is much lower. In table 5.2, the percentage of radius curvatures $< 10r_c$ at 263 K is listed as the proportion of pits of the total measurements. The percentage proportion is very low for all the samples, with smooth silica (WE) and rough sapphire (LW and WE) having the highest percentage. These results are further discussed with the freezing temperature results in section 5.4.

Table 5.1: Roughness parameters in RMS for rough sapphire, smooth sapphire and smooth silica. Results are based on AFM images and calculated using the Gwwydion software. See Equation B.13 for definition of RMS.

	Rough sapphire		Smooth sapphire		Smooth silica	
	LW	WE	LW	WE	LW	WE
RMS (nm)	121	180	0.57	0.13	4.3	0.59

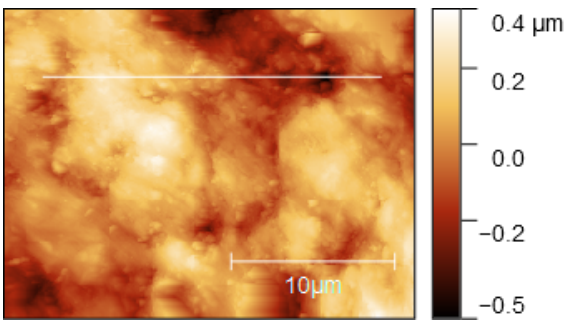

(a) AFM-image (LW)

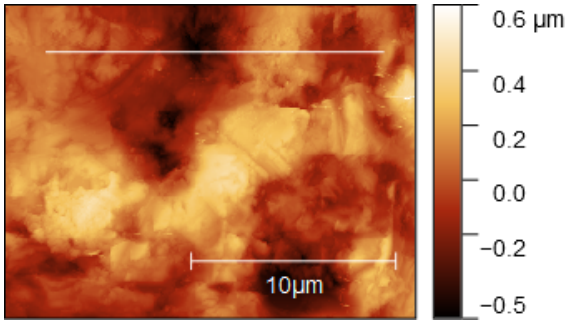

(b) AFM-image (WE)

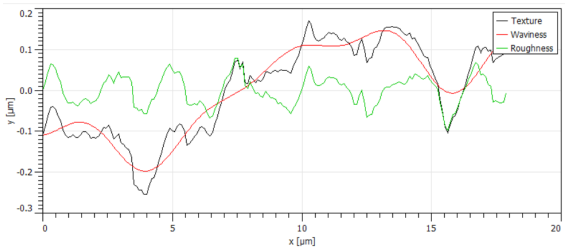

(c) Amplitude (LW)

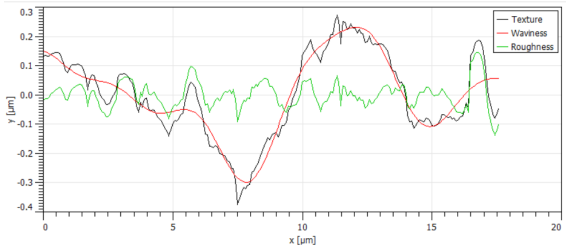

(d) Amplitude (WE)

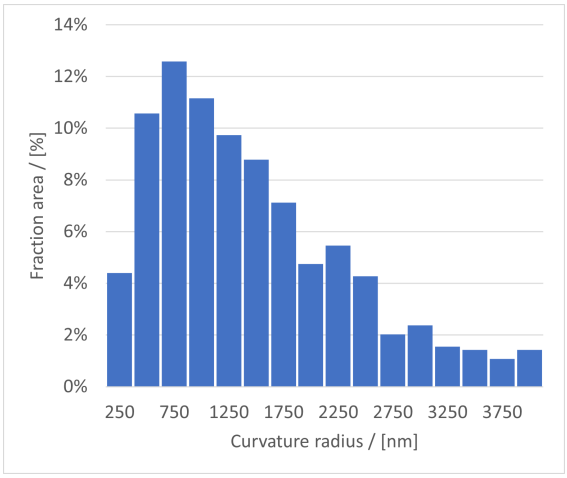

(e) Curvature Radius (LW)

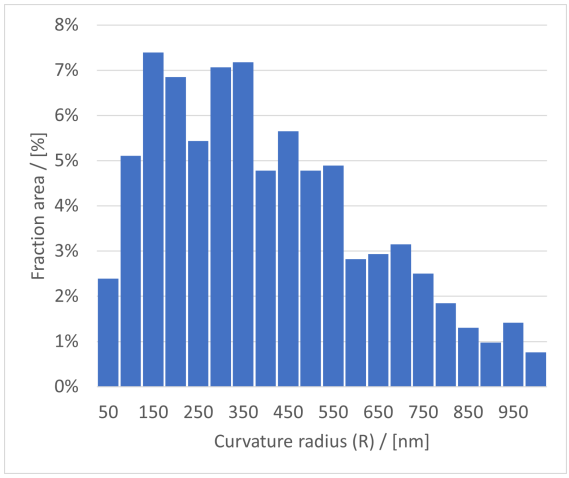

(f) Curvature Radius (WE)

Figure 5.1: Rough sapphire: (a) and (b) show topography AFM images of loosely washed (LW) and washed and etched (WE) rough sapphire. (c) and (d) show the amplitude of surface texture, measured at the white line in (a) and (b). The cut-off frequency is 0.0500 f_s (Nyquist frequency Hz). For c), the RMS roughness (high frequency) is 36.5nm, and RMS waveness (low frequency) is 106 nm at this line. For (d), RMS roughness is 45.5 nm, and RMS waveness is 136 nm. The proportion of curvature radius for pits is found in (e) and (f). The fraction area is the percentage of measurements with positive curvature radius, 18 % and 21 %, respectively. Figure 5.4 shows the distribution of all measured data. Details for the image processing and finding radius curvature can be found in Appendix B.1.1

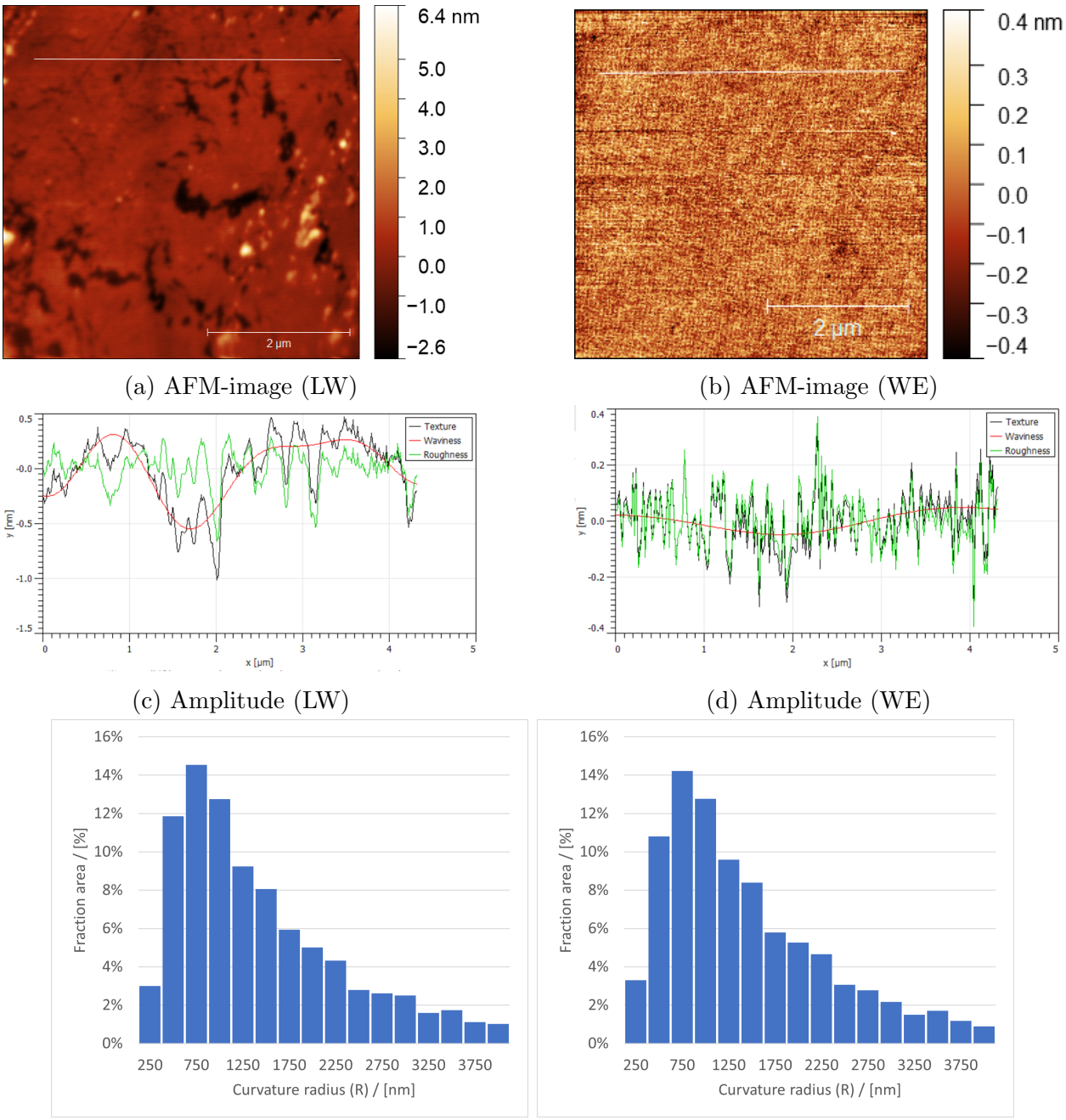

(a) AFM-image (LW)

(b) AFM-image (WE)

(c) Amplitude (LW)

(d) Amplitude (WE)

(e) Curvature radius (LW)

(f) Curvature radius (WE)

Figure 5.2: Smooth sapphire: (a) and (b) show topography AFM images of loosely washed (LW) and washed and etched (WE) smooth sapphire. (c) and (d) show the amplitude of surface texture, measured at the white line in (a) and (b). The cut-off frequency is 0.0140 f_s (Nyquist frequency Hz). For c), the RMS roughness (high frequency) is 0.17 nm, and RMS waveness (low frequency) is 0.26 nm at this line. For (d), RMS roughness is 0.10 nm, and RMS waveness is 0.03 nm. The proportion of curvature radius for pits is found in (e) and (f). The fraction area is the percentage of measurements with positive curvature radius, 20% and 20 %, respectively. Figure 5.4 shows the distribution of all measured data. Details for the image processing and finding radius curvature can be found in Appendix B.1.1

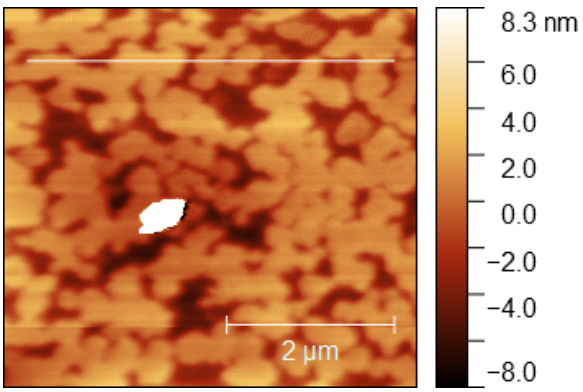

(a) AFM-image (LW)

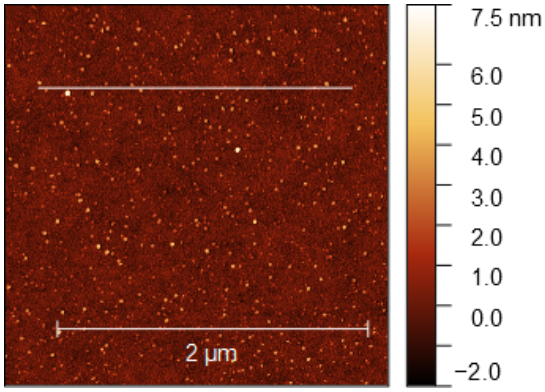

(b) AFM-image (WE)

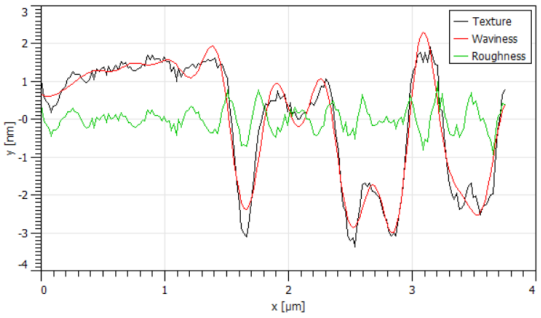

(c) Amplitude (LW)

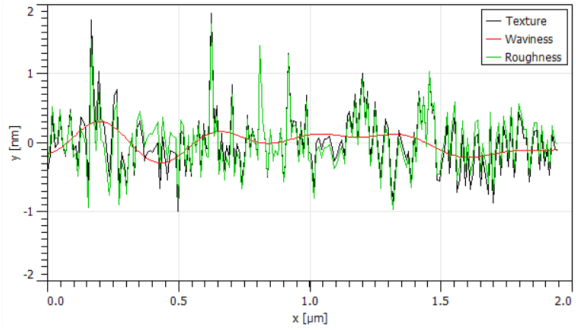

(d) Amplitude (WE)

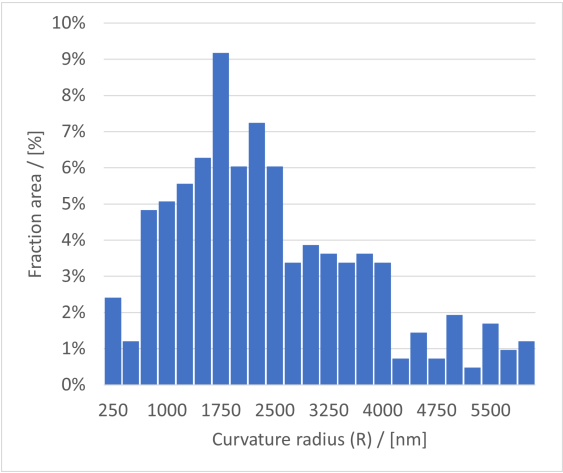

(e) Curvature radius (LW)

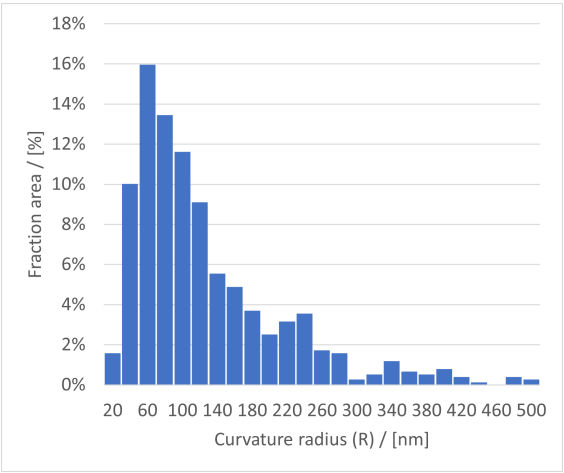

(f) Curvature radius (WE)

Figure 5.3: Silica: (a) and (b) show topography AFM images of loosely washed (LW) and washed and etched (WE) silica. (c) and (d) show the amplitude of surface texture, measured at the white line in (a) and (b). For c), cut-off frequency is 0.1200 f_s, the RMS roughness (high frequency) is 0.32 nm, and RMS waveness (low frequency) is 1.54 nm at this line. For (d), cut-off frequency is 0.0500 f_s, RMS roughness is 0.43 nm, and RMS waveness is 0.15 nm. The proportion of curvature radius for pits is found in (e) and (f). The fraction area is the percentage of measurements with positive curvature radius, 12 % and 6 %, respectively. Figure 5.4 shows the distribution of all measured data. Details for the image processing and finding radius curvature can be found in Appendix B.1.1

Table 5.2: Proportion of curvature radiuses $< 10r_c$ of ice embryo at 263K, as a percentage of the positive curvatures and of the total measurements. Critical radius is calculated by equation 2.9 and equations and values listed in Appendix (B.3.2.

	Rough sapphire		Smooth sapphire		Smooth silica	
	LW	WE	LW	WE	LW	WE
R $< 10r_{c,263K}$ (% positive)	2.4 %	1%	0.5%	0.6%	0.5%	15.6%
R $< 10r_{c,263K}$ (% total)	0.4 %	0.2%	0.1%	0.1%	0.1%	0.9%

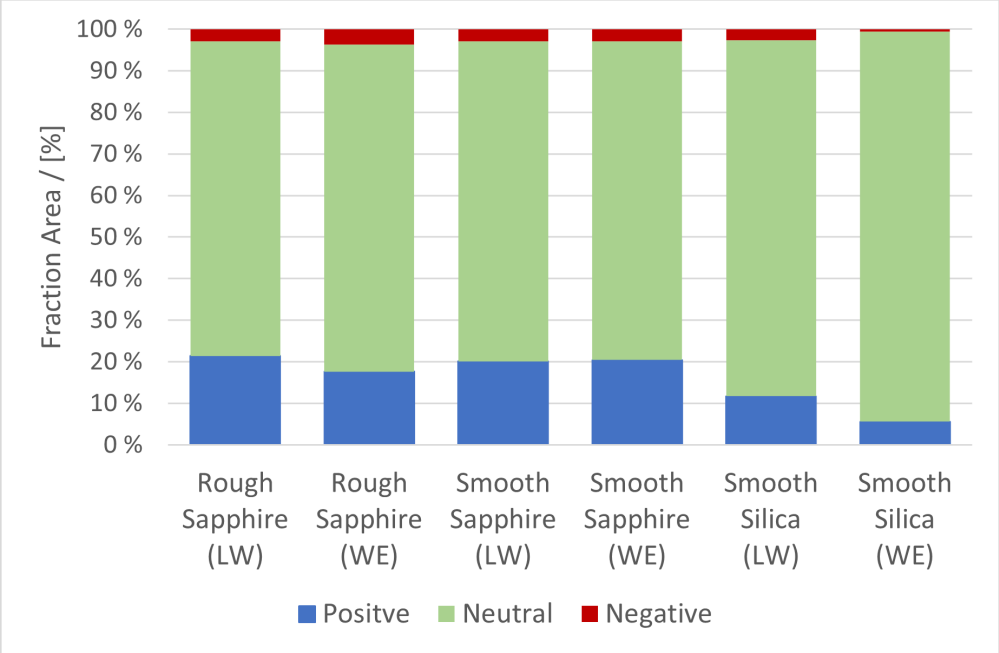

Figure 5.4: Curvature radius distribution for the different surface samples. Positive curvature indicates pits, neutral flat and negative bumps. The fraction area is based on the total amount of measurement points for each surface sample.

As seen in Figure 5.1, 5.2 and 5.3 the AFM images are recorded with different length scales and amounts of pixels. Thus the scale-lengths in between the pixels are at different scales, limited to ($\frac{\text{image scale length}}{\text{number of pixels}}$ = length between measured pixels). This indicates that the distance is around 78 nm for rough sapphire and 20 nm for smooth sapphire (the full table of distances may be found in Appendix A.1. Hence, the question is whether the image resolution is high enough to detect the minor curvatures, especially for the rough sapphire samples, and if the results are comparable.

A 256-pixel image was recorded of rough sapphire of 5 µm, which should be comparable to the smooth sapphire images. Analysing this image reveals an increase in the proportion of curvatures below $10r_c$, thus demonstrating the importance of AFM image resolution in the curvature analysis (see Appendix A.5).

5.1.1 Effect of Sample Preparation

As seen from the AFM examinations, the sample preparation procedure impacts the surface roughness. It is worth noting that even with washing, areas with foreign elements can be found on the surface alongside more pure areas, as seen in the Figures 5.5 beneath. This is valid for both samples washed with isopropanol and the samples with more throughout washing and etching preparation. However, the washing procedure does show a distinct effect on observed cleanliness for smooth sapphire and silica. The images were recorded using Brightfield microscopy, performed on W and WE samples before the freezing onset measurements.

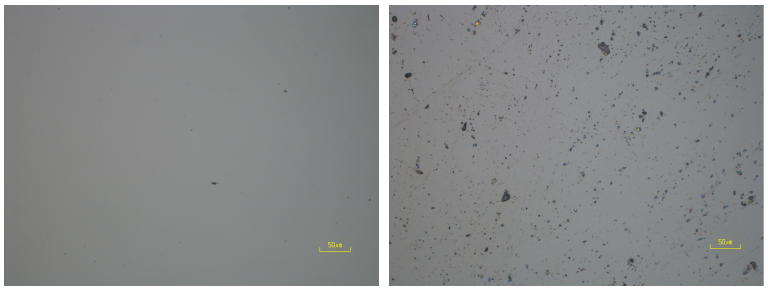

(a) Smooth sapphire (W) (b) Smooth sapphire (W)

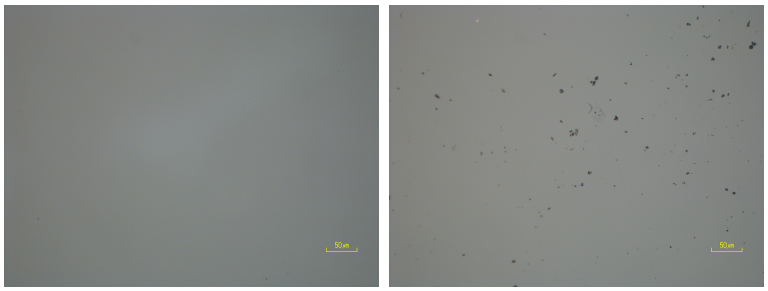

(c) Smooth sapphire (WE) (d) Smooth sapphire (WE)

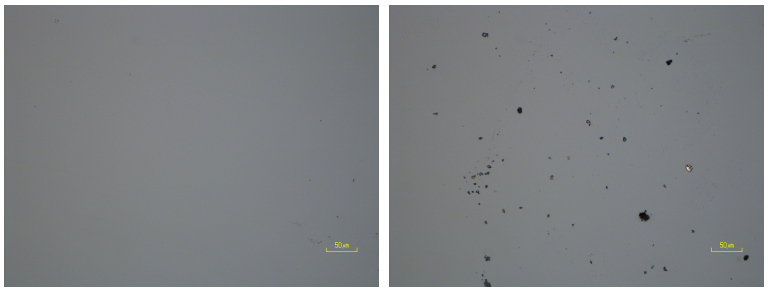

(e) Smooth silica (WE) (f) Smooth silica (WE)

Figure 5.5: Bright-field images of smooth sapphire (a-d) and smooth silica (e-f) with different sample preparation regimes; washed (W) and washed and etched (WE).

5.2 Contact angle measurements

Figure 5.6 and Table 5.3 present the results of the contact angle measurements, including static contact angle before freezing and advancing and receding contact angles as described

in section 4.4.3. These results showed that the average static contact angles for the sapphire samples had a significant uncertainty. As mentioned in Section 4.4.3, the static contact angles are not necessarily reproducible, which was one of the reasons advancing and receding contact angle measurements were performed. However, these measurements had a similar uncertainty as the static contact angle measurements.

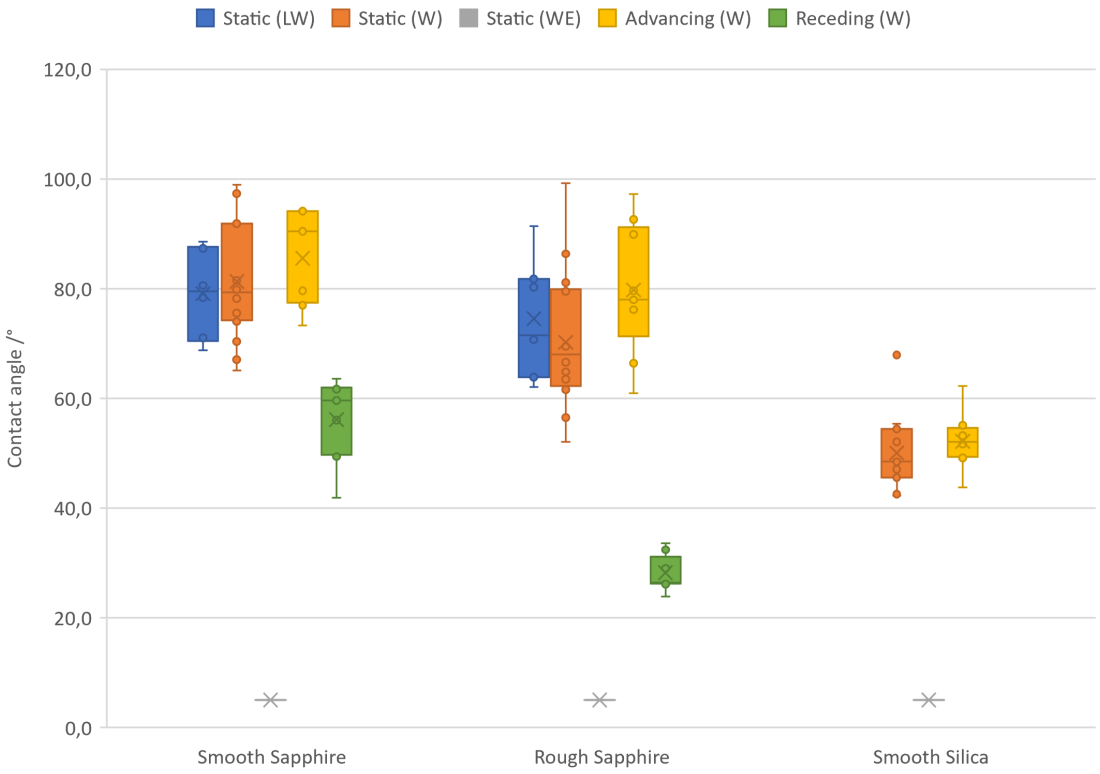

Figure 5.6: A boxplot of water contact angles measured, including static and dynamic contact angles. Single points indicate the contact angle values. Each cross represents the average value, and the middle line is the median value. The lower and upper box borderlines are the first and third quartiles (1Q/3Q), respectively, in which 25% and 75% of the data are within these points. The lower and upper whiskers represent the minimum and maximum values. The minimum value is defined as the difference between 1Q and 1.5 of the box range, and the maximum value as the sum of 3Q and 1.5 of the box range. Single points outside these whiskers are considered to be outliers.

Table 5.3: Contact angle measurement results, with uncertainty, for smooth sapphire, rough sapphire and smooth silica surfaces, including static, advancing and receding contact angles. The table also lists the number of measurements for each sample type, sample preparation and the relative humidity (RH).

	Static contact angle			Dynamic contact angle	
	Loosly washed	washed	washed and etched	ACA	RCA
Smooth sapphire	79° ± 7°	81° ± 10°	<5°	87° ± 8°	56° ± 7°
Measurements	6	19	12	9	9
RH	38%	53-59%	21%	45%	36%
Rough sapphire	74° ± 10°	70° ± 12°	< 5°	80° ± 10°	< 28°
Measurements	7	14	12	9	9
RH	38%	53-59%	21%	45%	36%
Smooth silica	-	50° ± 12°	< 5°	52° ± 4°	-
Measurements	-	12	12	9	-
RH	-	24%	21%	40-44%	-

As can be seen from the results, the contact angles of smooth sapphire are slightly higher than rough sapphire, but both are quite near hydrophobic. This differs from smooth silica, which has a lower contact angle, is hydrophilic and shows a tighter range of measurements, thus with less uncertainty. The washing and etching procedure significantly impacts the wetting properties, making all the surfaces completely hydrophilic (<5°), which can be observed in Figure 5.7. This is consistent with another study presenting the effect of washing procedures on different surfaces, including sapphire [82]. Different studies report various contact angles in the range of 65-84° on flat sapphire [4,83,84], primarily in the c-plane. The different crystal planes induce different mechanical and optical properties [85]. A study measuring contact angle for different crystal planes found that the c-plane had a lower contact angle than the a,m and r-plane. For instance, the r-plane had a contact angle of 86°, whereas the c-plane had 65° measured in 50% RH [84]. However, another book reports the opposite, with 74° on the r-plane and 84° on c-plane [83].

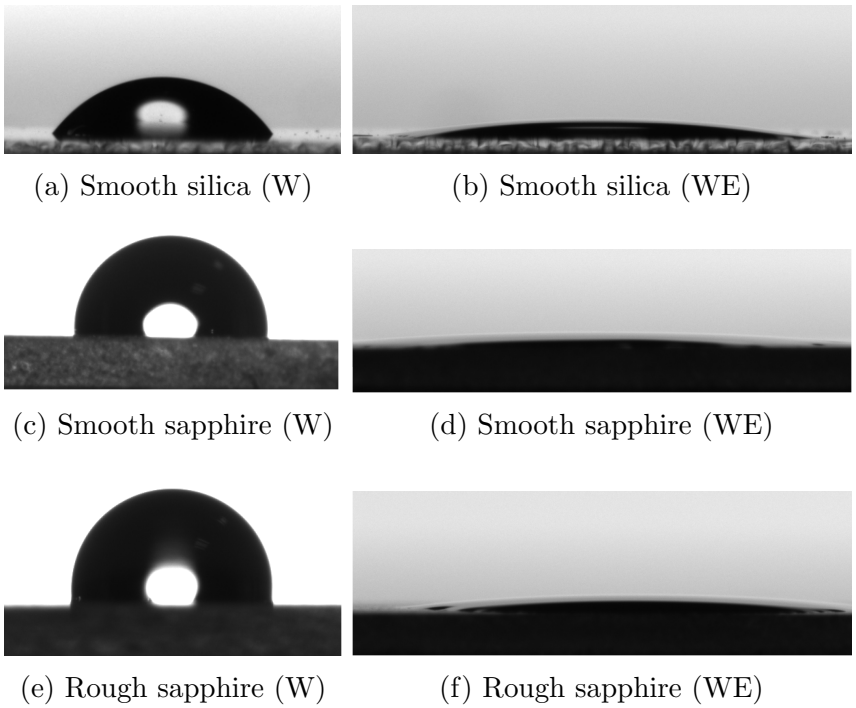

(a) Smooth silica (W) (b) Smooth silica (WE)

(c) Smooth sapphire (W) (d) Smooth sapphire (WE)

(e) Rough sapphire (W) (f) Rough sapphire (WE)

Figure 5.7: Snapshot of static contact angle for $2\mu L$ water droplet on smooth silica (a-b), smooth sapphire (c-d) and rough sapphire (e-f). With sample preparations, washed (W) and washed and etched (WE).

The advancing contact angle measurements are slightly higher compared to the average static contact angles. However, the angle ranges do not show significant differences. The Figure 5.8 below shows the contact angle variations with the droplet baseline. A recurrent problem during the measuring process has been the droplets sliding on the sample surface, resulting in an altered needle position, and thus water not being homogenously added. When this happened, the needle was manually moved back into a centred position, resulting in droplet disturbance. This issue is a probable reason for the inconsistent results seen in Figure 5.8. A possible explanation may be dynamic effects on the droplet caused by an excessive flow rate, as the added water flow rate was approximate twice the recommended rate [35]. Additionally, the variation in humidity and local impurities can not be excluded as a possible impacting factor. In fact, a master thesis documented results of RCA measurements showing a significant impact of humidity variations due to a broken humidity controller in the cleanroom [86]. This was a smaller issue for the smooth silica samples, perhaps due to its hydrophilic properties.

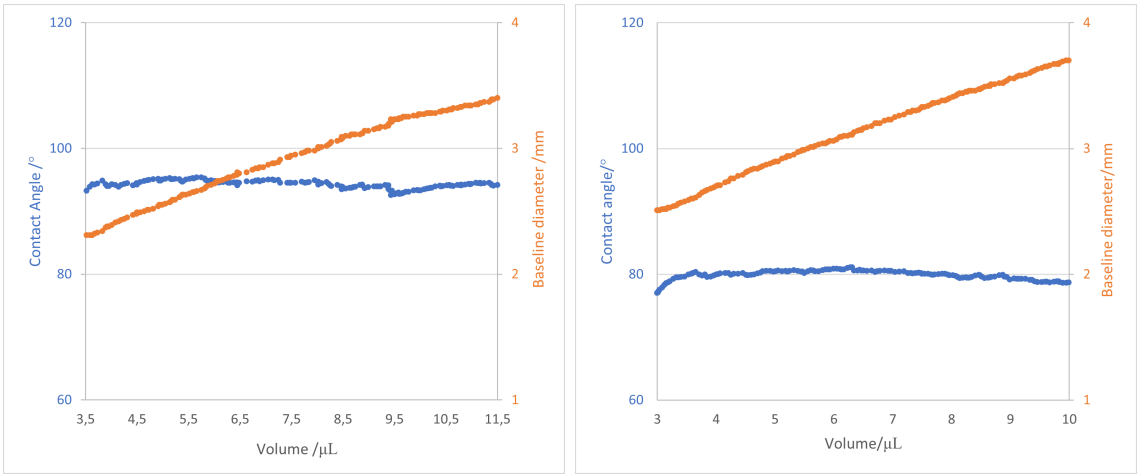

(a) Smooth sapphire (W)

(b) Rough sapphire (W)

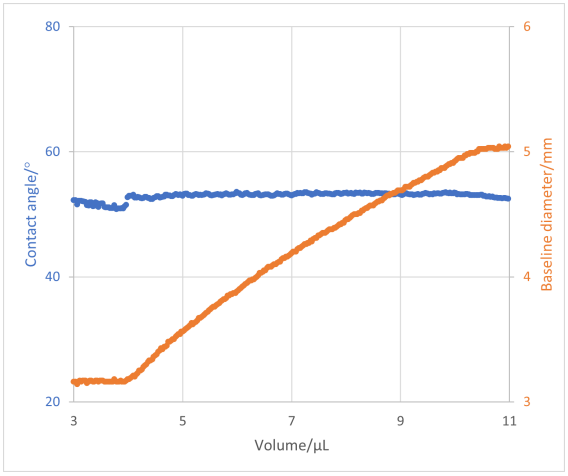

(c) Smooth silica (W)

Figure 5.8: Advancing contact angle (blue line) of water on smooth sapphire (a) and rough sapphire (b) plotted against droplet volume. The right axis is the variations in baseline diameter (orange line) with observed droplet volume.

Receding contact angle measurements were performed for the two sapphire surfaces. The contact angle variations with droplet baseline are shown in Figure 5.9. As explained in Section 4.4.3, the small sample sizes only enabled 30-40 µL water to be applied, which was sufficient for the smooth sapphire sample. However, for the rough sapphire sample, this was substantially less than the required starting volume of approximately 70-100 µL (see Figure 4.13). The receding angles measured for smooth sapphire were adequate, whereas the rough sapphire did not gain enough volume to reach its real value, indicating a receding angle of less than 28°. As explained in theory (see section 2.2.2), the high wetting hysteresis indicates that the rough sapphire sample has Wenzel state wetting properties.

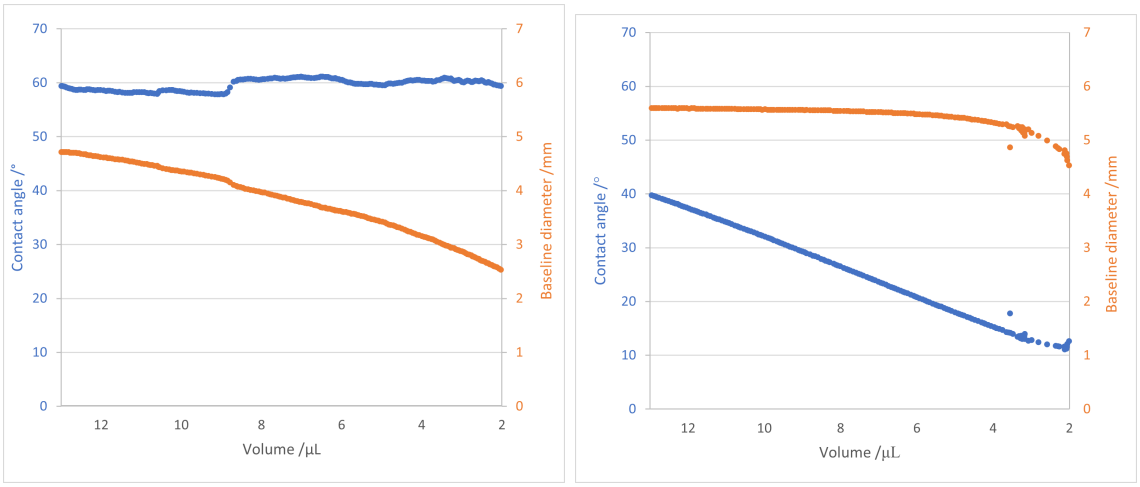

(a) Smooth sapphire (W)

(b) Rough sapphire (W)

Figure 5.9: Receding contact angle (blue line) of water on smooth sapphire (a) and rough sapphire (b) plotted against droplet volume. The right axis is the variations in baseline diameter (orange line) with observed droplet volume.

5.3 NMR-measurements

The NMR spectra presented in this section were recorded and processed as described in section 4.3 and Appendix B.1.2, respectively. All the recorded samples can be regarded as loosely washed (description found in section 4.2). As the intensity of the NMR is widely dependent on the magnetic field, pulse program, parameters and sample volume, the intensity is arbitrary and thus not comparable. Hence, the standard in the field of NMR is to present spectra without an intensity axis. For this reason, only spectra where the intensities are comparable or provide information of interest are presented with an intensity axis. In cases where the intensities are not comparable or provide any necessary information, the spectra are presented without the intensity axis as the standard in the field.

5.3.1 Interfacial Water on different surfaces

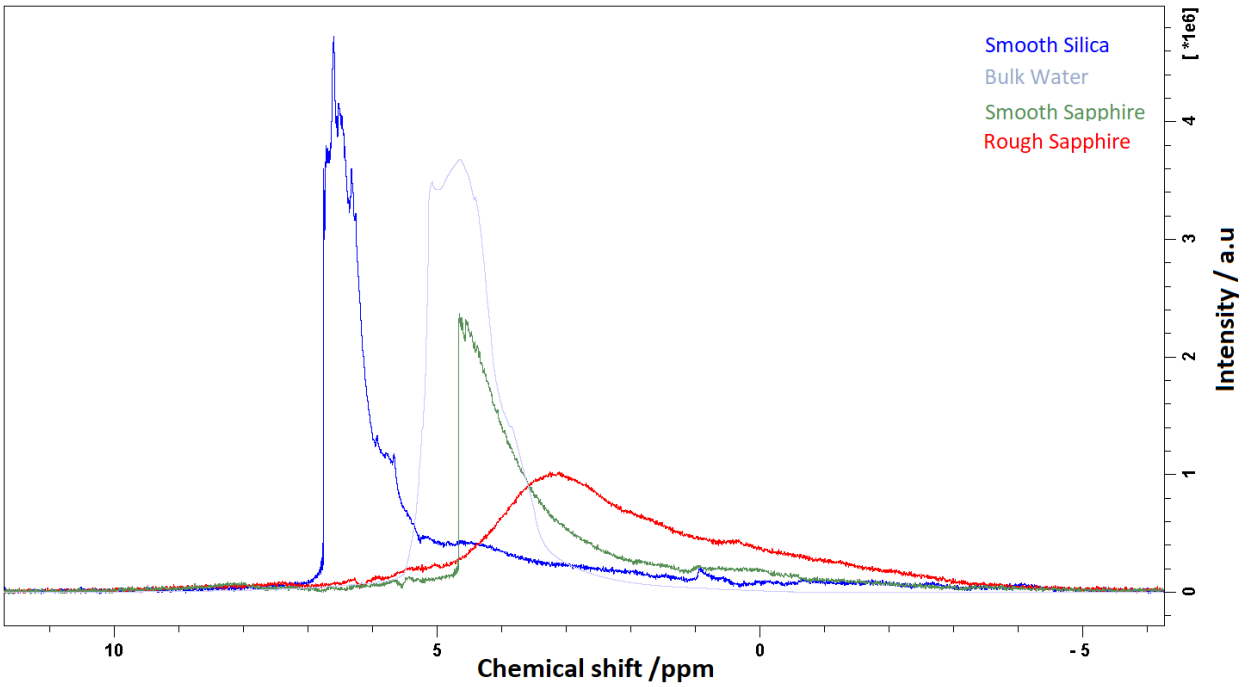

Figure 5.10: Comparison of ^{1}H NMR spectra of interfacial water on the three different surfaces and bulk water sample in quartz container recorded at 295 ± 1 K. Chemical shift at the x-axis given in ppm reflects the protons' absorbed resonance frequency. The y-axis is the intensity of absorption in a relative arbitrary unit (a.u). Bulk water is scaled by factor 11.31 and recorded with different parameters (rg=4.5, ns=1) than listed in 4.1. Thus the bulk water is not comparable in intensity with the other.

Figure 5.10 compares the ^{1}H-NMR spectra of interfacial water on rough and smooth sapphire, smooth silica and regular bulk water at 295 K. The main findings, as observed in the figure, are the differences in chemical shift, shape and width. These observations reflect the differences in the chemical environment for the water protons in contact with the different surfaces and the more homogeneous environment for referenced bulk water. Chemical shift and WHH values are listed in Table 5.4. For reproducibility of the spectra, see Appendix A.5.

Table 5.4: Chemical shift and width at half height (WHH) data for the 295K ± 1K samples of interfacial water on the different surfaces. The WHH and chemical shift of surface water are calculated using average values with standard deviation from manually measured points of six samples for each surface type. The point of chemical shift for the smooth and rough sapphire spectra is determined using the top point. The midpoint of WHH was used for the silica samples and bulk water. The chemical shift of the bulk water is a theoretical value used to calibrate all the axes, and the WHH is an average value with a standard deviation for three bulk water samples. More details on the process for determining chemical shift, WHH and peak integral can be found in Appendix B.2

Surface	Smooth silica	Smooth sapphire	Rough sapphire	Bulk Water
WHH (ppm)	0.6±0.1	0.9±0.1	3.2±0.3	1.07±0.01
Chemical shift (ppm)	6.45±0.06	4.68±0.09	3.1±0.2	4.63
Peak integral (a.u)	$3 \cdot 10^{-6} \pm 40\%$	$3 \cdot 10^{-6} \pm 39\%$	$2.3 \cdot 10^{-6} \pm 24\%$	-

The results in Table 5.4 and Figure 5.10 show a higher chemical shift for water on the silica surfaces than on the sapphire surfaces. As described in section 5.3.4, the appearance of hydrogen bondings has a deshielding effect on the peak, resulting in a higher chemical shift. Thus the results indicate that silica silica is more hydrophilic than the sapphire surface, which corresponds well with the contact angle results. The higher chemical shift is caused by the water molecules being more bound to the silica surface, shifting the HDW/LDW balance towards LDW, which also lowers the water molecule mobility [29]. The chemical shift for water on smooth silica is 6.45 ppm, as seen in the table. This is unexpected, as the chemical shift is significantly higher than 3.20 ppm, reported in similar studies on water adsorption on silica surfaces [28, 29, 87]. However, it is presently not clear what the reason for this is.

The sapphire surfaces have a lower chemical shift, indicating a shift in the HDW/LDW balance towards HDW and fewer water molecules bound to the surface. As seen from the figure, there is a slight difference between the chemical shift for smooth and rough sapphire, indicating that rough sapphire is slightly more hydrophobic with higher mobility of the water molecules. This is the opposite of the findings in the contact angle results (Section 5.2). A potential explanation for these contradictory results may be the differences in micro-environments with a droplet on a surface versus water between sample plates.

Another plausible explanation might be the distinct differences in the shape of the two sapphire peaks. The shape of the smooth surface spectra indicates a more axial symmetry, whereas the rough sapphire show more of a non-axial symmetry. This may be due to the more curvature surface of sapphire, resulting in more directional orientations of the hydrogen bondings than on flat surfaces. The anisotropic and asymmetric peaks, observed especially on smooth sapphire, may show a higher chemical shift than isometric peaks of the same material, as seen in Figure 3.5 and 3.6. Thus the chemical shift differences might be more consequential to the position of the hydrogen atoms on the surface rather than an indication of diffusion.

The molecules' mobility in the sample also affects the width of the observed spectra, where broader peaks indicate lower mobility. As seen in the table, there is a slight difference

in width between silica and smooth sapphire surfaces. However, the rough sapphire surface shows a significantly larger spectrum width, indicating that water molecules are less mobile on the rough surface than on the two smooth surfaces.

A higher degree of roughness means more surface area and thus more water bound to the surface than on a flatter surface, which may explain the lower mobility. However, as explained above, the broad peak could also be due to water molecules bound in more directions than the smooth rather than a mobility effect.

The calculated integral of the peak, found in Table 5.4, may be used to analyse the amount of water in the sample. Smooth sapphire and silica have a relatively similar integral, while rough sapphire has a smaller integral. However, all the samples had extensive uncertainties, ranging from 24-40 % of which a prominent contributor is the variance of the applied water volume, with an uncertainty of 33 %.

As explained in section 5.3.3, several challenges with the NMR setup became apparent during the project, giving rise to sources of errors and uncertainties to be addressed. The sources of error that may have impacted the results include background noise signal, drift in the magnetic field, shimming effect, amount of applied water and parafilm, bulk water calibration, the subtraction process and potential impurities.

5.3.2 Bulk Water Reference Sample

A calibration was performed as a mitigating measure to counteract the effect of magnetic field drift in the spectra. This was done using bulk water as a reference to calibrate the chemical shift (x-axis) with a more realistic chemical shift for water on the surface (further described in Appendix B.1.2). There are some uncertainties in this calibration process, including reproducibility, drift in the magnetic field and the effect of shimming.

The reproducibility of the bulk water calibration is limited, as the calibration was based on one single bulk water sample, thus requiring that this exact sample have a high degree of purity. However, it is worth mentioning that several other bulk water samples were tested early in the project. The results of these bulk water samples correspond well with the shape and chemical shift of the sample used in the calibration, thus strengthening confidence in reproducibility.

The variance in magnetic field drift over time may cause a chemical shift divergence between different NMR recording periods. Thus, ideally, the bulk water reference spectrum would be recorded each day of the NMR recordings. However, this was not achievable due to the time consumption needed and the issues with fragile and expensive sample holders that easily broke. Thus with only one sample recorded in this period, it is not sufficient to decide on the precise values to calibrate chemical shift and thus eliminate the deviations caused by natural drift completely.

To estimate the drift, the background noise spectra recorded in the same period as the interfacial water samples were compared. Thus the deviations in chemical shift could be calculated. The result was a standard deviation of 0.2 ppm and 0.07 ppm if only considering the noise spectra with a similar amount of parafilm as done for the smooth sapphire samples. These results indicate that the natural drift may be a plausible explanation for the observed deviations. As may be seen in Appendix A.1.1 the drift is unpredictable and can move in both directions.

As seen in Figure 5.11, the bulk water significantly impacts the shape and chemical shift with the shim adjustments. The two peaks of the bulk water spectra deviate from the expected single peak of water.

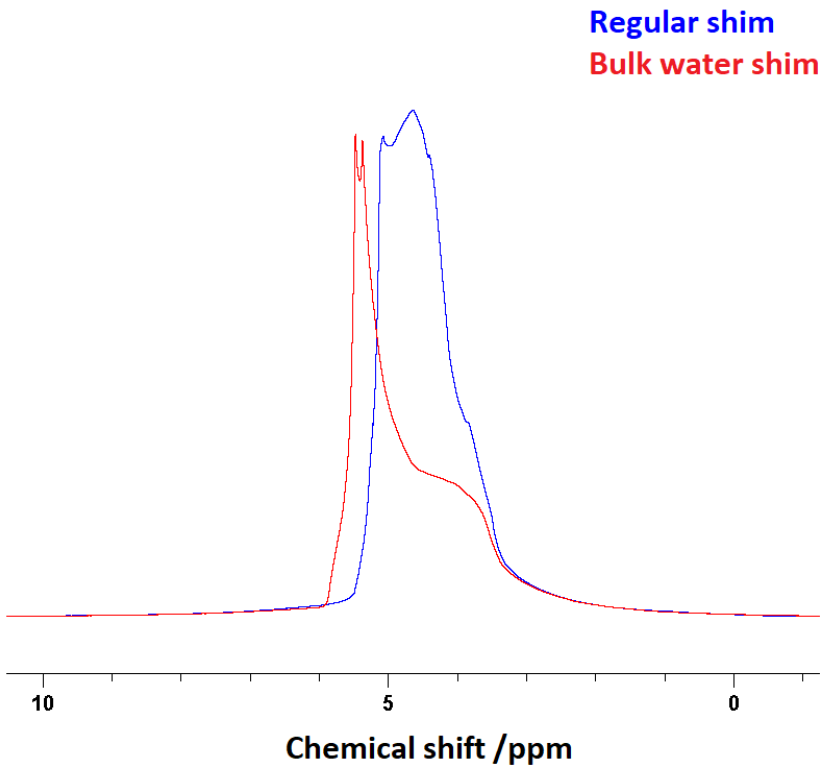

Figure 5.11: Shimming effect on bulk water with bulk water shim (red) and regular sample shim (blue).

5.3.3 Impact of Background Signal

The challenges regarding background noise signals were gradually discovered during the NMR experiments, as explained in section 4.3.7. For instance, the coil was shown to induce a background signal even with the T_2-filter in addition to other contributors, including parafilm, the impact of subtraction and drift in the magnetic field. Thus all the spectra presented in this thesis have been processed with background signal subtraction (see more details in Appendix B.1.2).

Parafilm

The parafilm used in sealing the samples was shown to contribute to the background signal. Thus, it was decided early in the project to use 3D-printed corks to seal the sample holder. However, this introduced new challenges with fragile sample holders that tended to break

and the lack of sufficient sealing. This solution was later abolished in favour of parafilm despite the background noise.

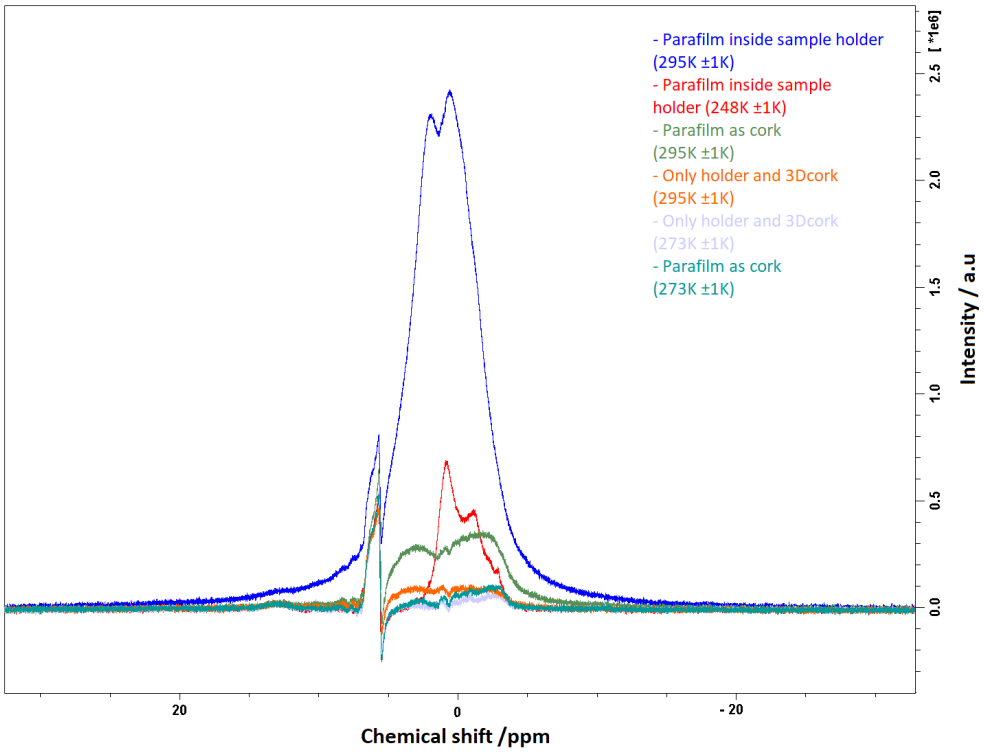

Figure 5.12: Spectra of background signal and parafilm signal with temperature dependence

The spectra of the parafilm proton signal show that the signal intensity decreases significantly already at 273 K. Further decreases in temperature do not lead to any significant changes in signal intensity but do show some minor changes in phase and chemical shift. The signal is present all the way to the lowest measured temperatures of 230 K. A small signal, induced from the used parafilm, can be observed on the shoulder of the coil signal, as it has not been subtracted. The spectrum with only a sample holder also shows a slight temperature component. The parafilm signal at the end also shows a temperature dependency, meaning that the amount used will impact the background signal, both with regards to volume and shape. Thus demonstrating the importance of adding the same amount of parafilm to the sample holder when performing the experiments. As this factor was not discovered until later in the project, it was only considered for the smooth sapphire samples and two of the rough sapphire samples. The rest of the results clarified that the spectra of dry plates, 3D cork and sample holder did not show any contribution to the background signal.

Impact of Subtraction

All the spectra of the water samples presented in this thesis have been processed with background noise subtraction. The accuracy of the measured chemical shift, integral, WHH and

shape will thus be impacted by the quality of this subtraction process. Ideally, all background noise spectra would be eliminated by subtracting a stable and accurate background signal reference recorded at the same temperature, leaving only the signal from the sample left in the spectra. However, it is impossible to perform a perfect subtraction of background noise in the spectra, even if the background noise reference was recorded on the same date. This is because the background noise changes shape over time and varies with temperature and the amount of parafilm used, as discussed earlier. This is especially the case for the smooth silica samples, as these recordings were performed over a more extended period of time. Also, the background noise spectra were insufficient references as the signal was too low in intensity, caused by a lack of magnetic field stabilisation and the deviation in the amount of parafilm. For the rough sapphire samples, the noise spectra were recorded relatively close in time, but the amount of parafilm was not closely controlled at this time, as previously explained. Since there will be slight changes in phase even within the same day of recording, there will thus always be an inaccuracy in the noise subtraction process.

Drift

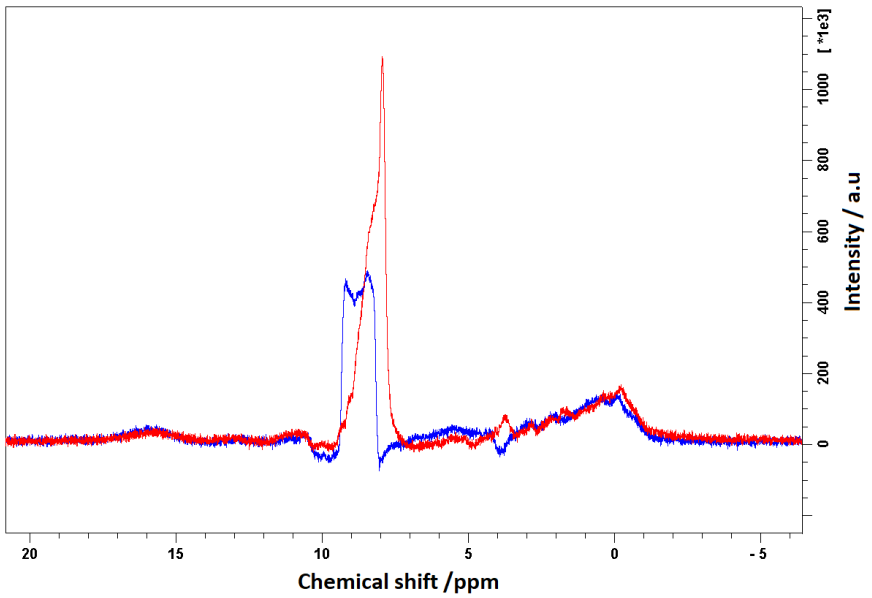

Figure 5.13: Background spectra recorded two months apart. Showing changes in shape, intensity and chemical shift due to drift.

During the project, it became evident that the background noise changed in shape, intensity and chemical shift over time, as seen in Figure 5.13. This might be explained by the drift in magnetic field that naturally occurs in solid-state NMR.

Shimming

Figure 5.14 shows the background noise signal using regular sample shim (blue) and bulk water shim (red). The shimming highly impacts the chemical shift, symmetry and shape

of the signal from the coil and parafilm at low temperatures. It might thus have been a good idea to use the bulk water shim, as it potentially is easier to subtract because of the symmetry and lower chemical shift.

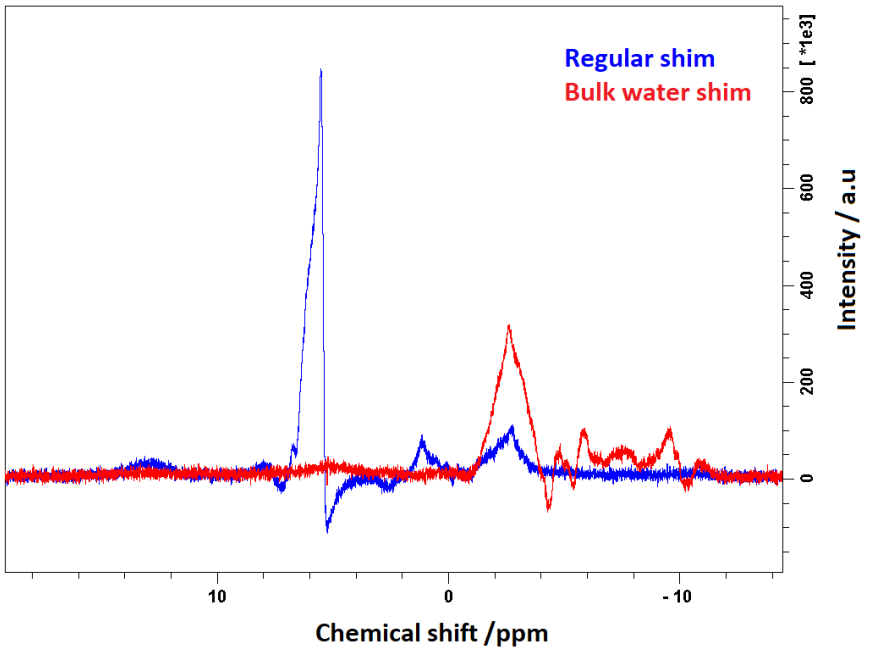

Figure 5.14: Shimming effect on noise. Regular sample shim (blue) and bulk water shim (red).

T_2-filter

As explained in section 4.3.3, the T_2-filter will mute signals according to Equations 3.11 and Equation 3.10. In practical terms, signals from low-mobility molecules are filtered out from the spectra. In addition to the important filtering of background signal, this also introduces the risk of filtering out parts of the actual sample signal. The interfacial water is generally less mobile than regular bulk water. However, the risk is considered minor because of the water molecules' low viscosity. But as there is no reference of a sole sample with 90-pulse without the background signal to compare with, the risk cannot be ruled out with certainty. In addition to the T_2-value, the muting effect is also dependent on the sample water volume and parameters, including number of scans (ns) and receiver gain (rg), making it impossible to accurately determine the effective degree of muting.

5.3.4 Freezing Out Layer by Layer

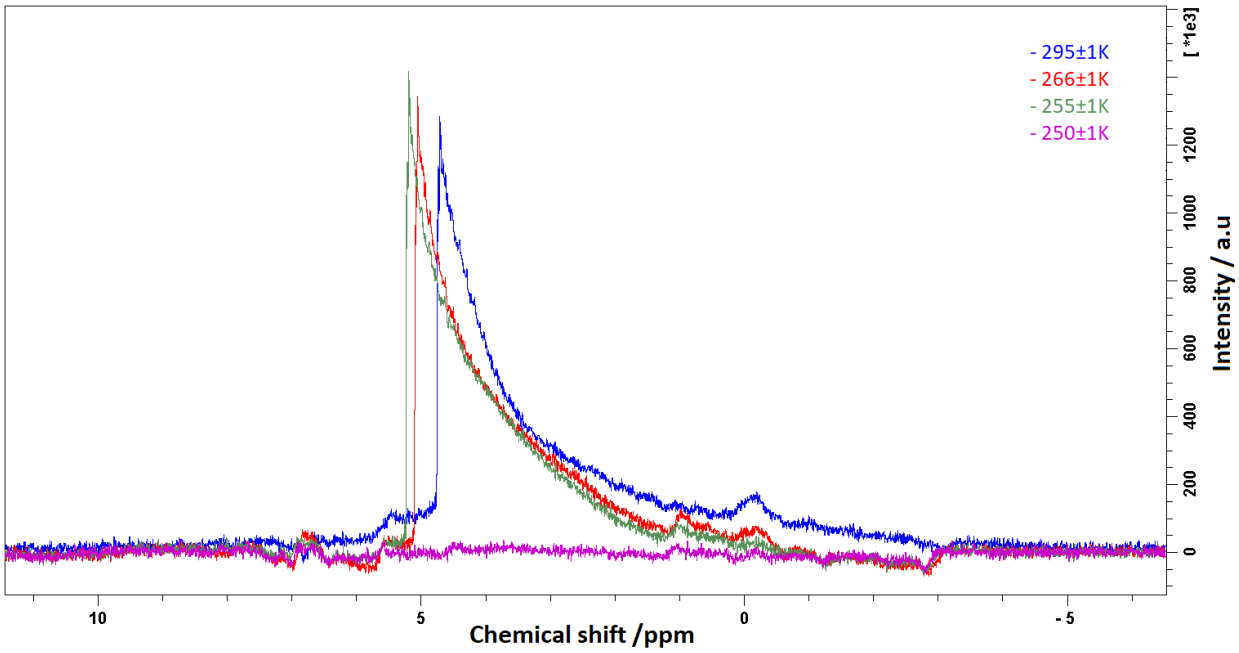

(a) Smooth sapphire

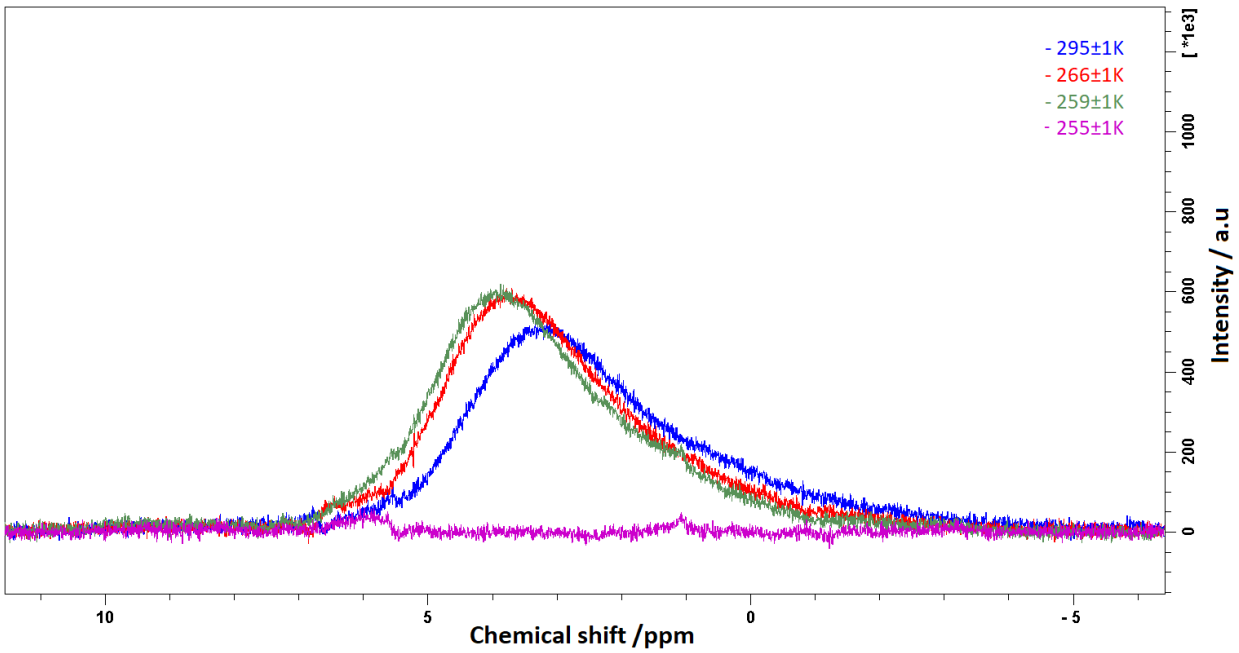

(b) Rough sapphire

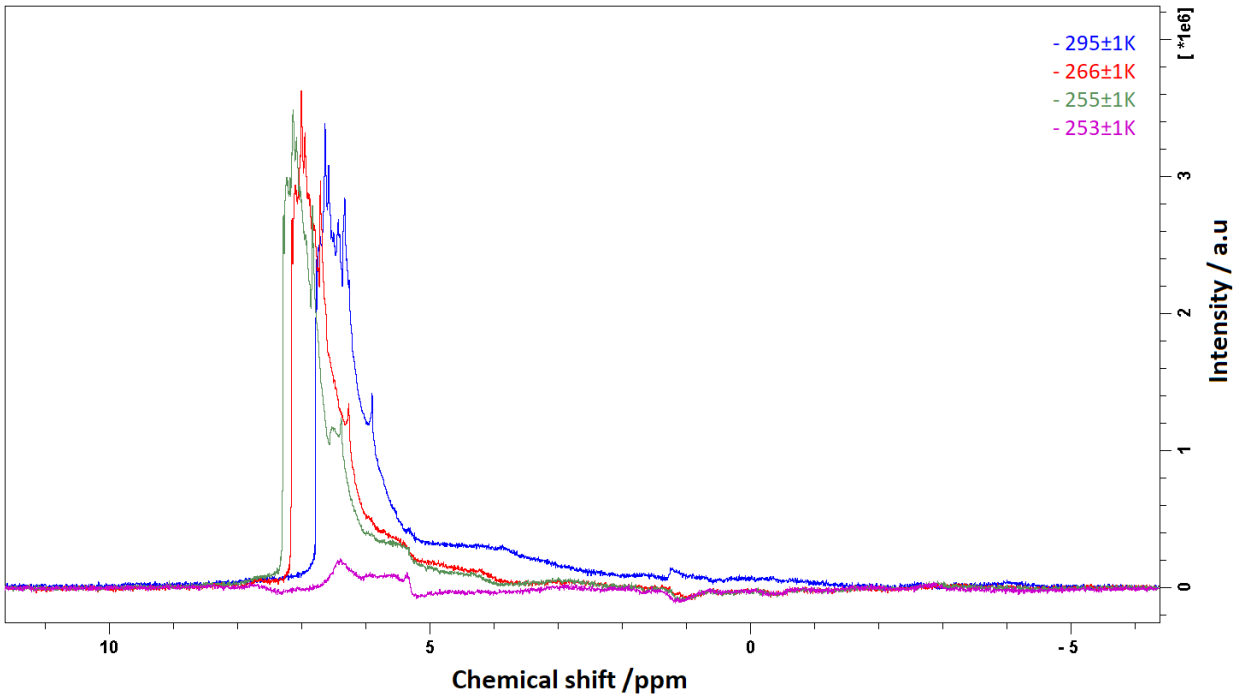

(c) Smooth silica (type 1)

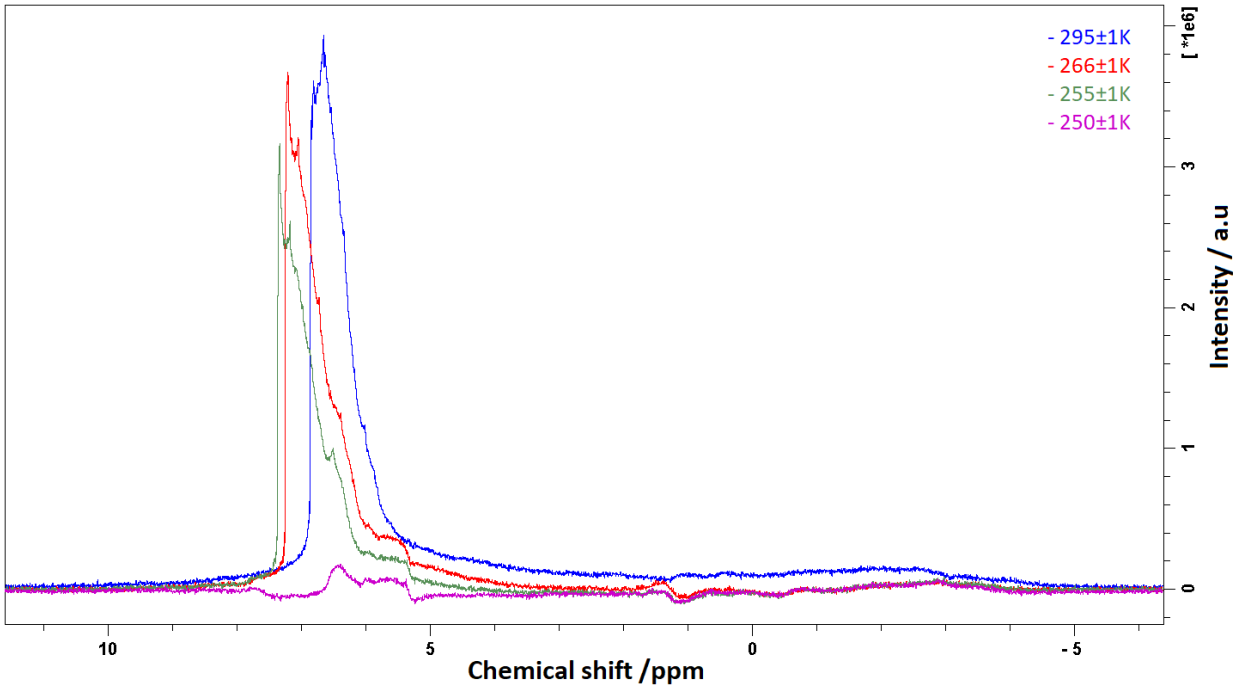

(d) Smooth silica (type 2)

Figure 5.15: Effect of temperature variation for 1H-NMR spectra of interfacial water until freezing on (a) smooth sapphire, (b) rough sapphire, (c) smooth silica (type 1) and (d) smooth silica (type 2) . The plot consist of four selected temperature points, where green is used for the last spectra recorded before freezing and purple for spectra after freezing.

The results of the freezing measurements are presented in Figure 5.15, showing four ^{1}H-NMR spectra at different temperatures of each sample of water on smooth sapphire (a), rough sapphire (b) and two samples for smooth silica (c-d). For reproducibility of the temperature trends, spectra of all the samples are found in Appendix A.6. In all four figures, the blue line show spectra recorded at room temperature, red at 266 K, green the last recorded spectra before freezing and purple recorded after freezing. These figures will thus show the change in signal intensity and chemical shift in the NMR spectra as the temperature was lowered until freezing occurred.

One of the main observations, which seems to be valid across all the surface samples, is that the peak of the spectra in general shifts towards a higher chemical shift with decreasing temperature until freezing. The same trend is found in other studies for bulk water and some studies for interfacial water [29, 68].

Another observation is that for smooth and rough sapphire, all the samples show similar spectra as the samples shown in Figure 5.15a and 5.15b, where the intensity increase with decreasing temperature. On the other hand, the smooth silica surfaces produce two different trend types, as shown in Figure 5.15c and 5.15d. The first, labelled type 1 (c), shows a similar trend as for the smooth sapphire (a), whereas type 2 (d) shows a gradual decrease in intensity with decreasing temperature.

A sudden drop in intensity between the last temperature recorded before and after freezing can also be observed. As mentioned in Section 3.1.2, ice will not be detectable in the ^{1}H-NMR spectra because of the extremely short T_2 value caused by the lack of mobility in the ice structure. As shown, the purple line is not as straight as expected if there were no signal.

Partly Freezing

As mentioned in section 4.3.4, the freezing temperatures were somewhat unpredictable, and the process for each spectrum recording was very time-consuming. Hence, this made it difficult to standardise the temperature intervals and the number of measurements for each sample. The exact temperatures for all the recorded spectra can be found in Appendix A.2, Figure A.4.

Some of these samples were recorded with very short intervals near the actual freezing temperature (sample 2 and 4 for rough sapphire and 3 and 7 for smooth silica in Figure A.4). The spectra of these samples, presented in Figure 5.16a and 5.16b, reveal some interesting trends near the freezing point.

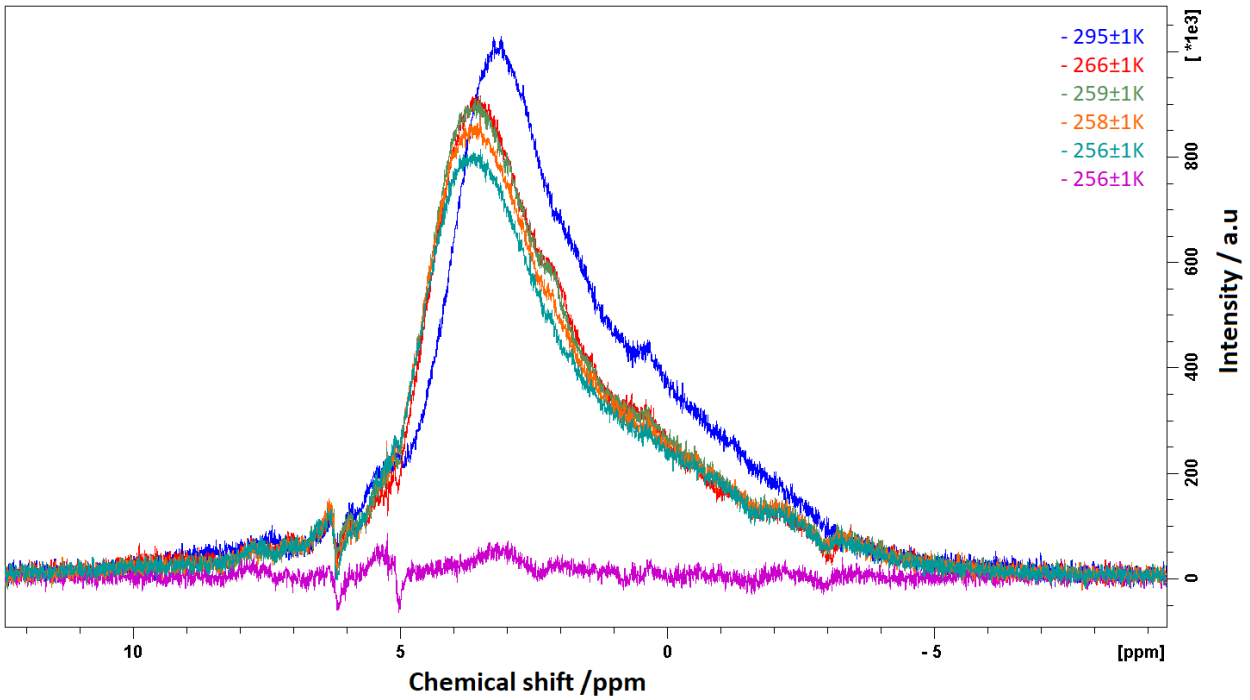

(a) Rough sapphire

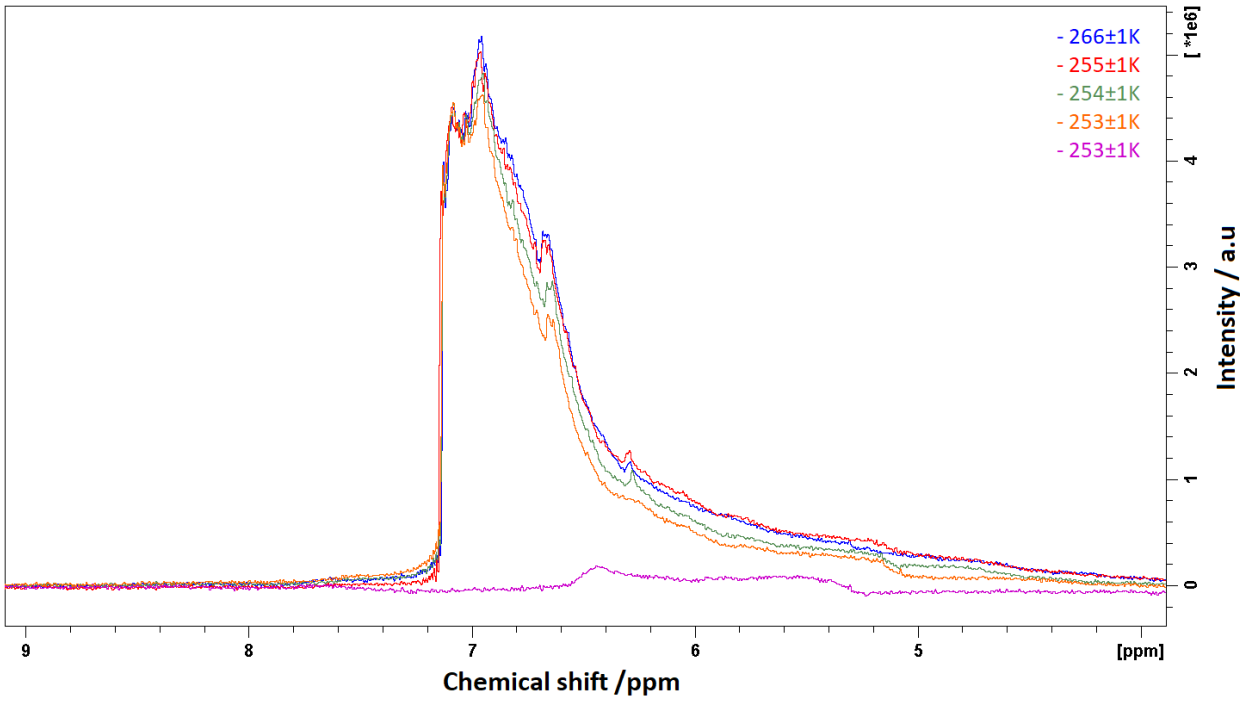

(b) Smooth silica

Figure 5.16: ^{1}H-NMR spectra of interfacial water on (a) rough sapphire and (b) smooth silica (type 1) with tight temperature intervals near the freezing point, showing the partly freezing trends. For smooth silica (b), the spectra have been shifted and placed directly upon each other (disregarding the absolute chemical shift value) to observe trends.

The spectra in Figure 5.16a reveal the tendency of a rapid decrease in signal right before the freezing point. This tendency can also be observed on the smooth silica spectra in Figure 5.16b. This may be interesting to investigate in the context of water properties and the freezing process as it could indicate that the water in this temperature range is undergoing partly freezing where not all of the water freeze simultaneously.

Another observation is that in Figure 5.16a the freezing temperatures are the same as the last recorded spectrum before freezing. Hence, the accuracy of the temperature determination has some factors to be considered. The environment inside the probe head is controlled using temperature-regulated airflow. The smallest temperature interval of the airflow is $\pm$ 0.5 K or 0.4 K after temperature calibration. However, the inaccuracy of the temperature calibration itself was $\pm$ 1 K. Hence the inaccuracy can cause spectra to show both non-frozen and frozen water at the same temperature, despite the latest spectrum recorded with a 0.5 K lower airflow temperature.

Width at Half Height

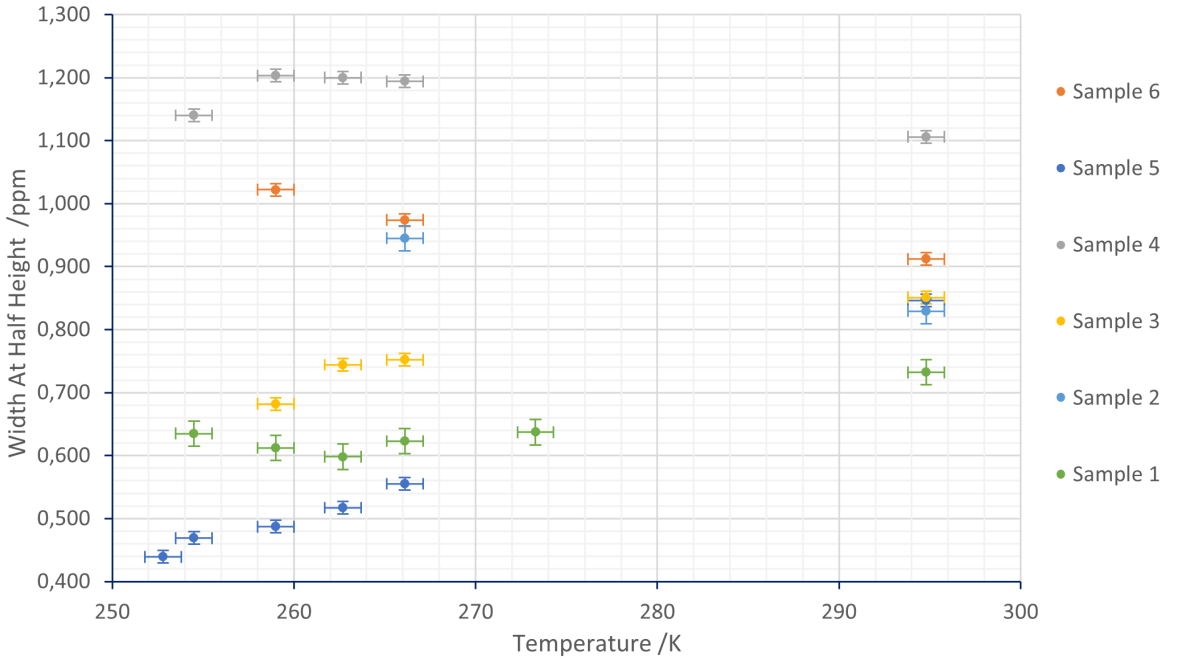

(a) Smooth sapphire

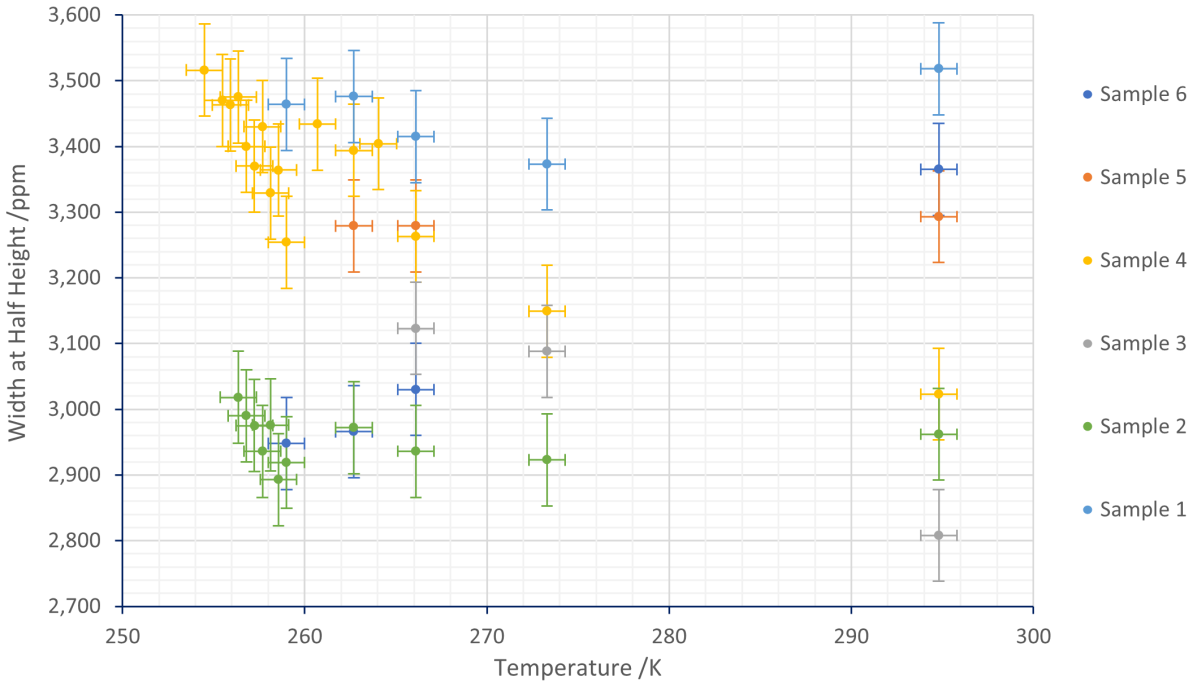

(b) Rough sapphire

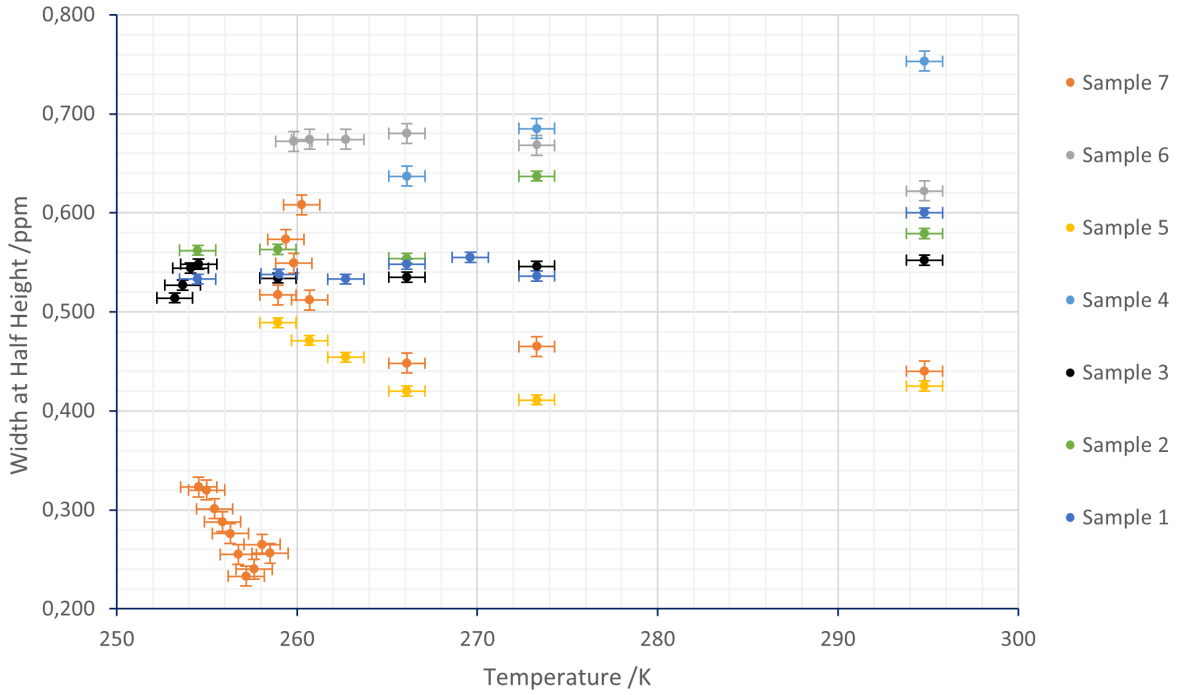

(c) Smooth silica

Figure 5.17: Measured width at half height (WHH) of the water peak in the NMR spectra plotted against temperature at recording for each sample

Figure 5.17a, 5.17b and 5.17c show how the width at half height (WHH) of the spectra varies with temperature. The figures generally show a chaotic picture with no clear significant trends in most series, but with a few interesting exceptions. On rough sapphire in Figure 5.17b (sample 2 and 4), the WHH increases near the freezing point. This is likely explained by the water molecules becoming more structured and less mobile, which supports the assumption of partly freezing. This is also observed in Figure 5.17c for sample 7 for the measurements near freezing point. However, the smooth silica sample 3 in Figure 5.16b shows the opposite effect, probably due to the intensity decline in the right shoulder of the peak.

Integral

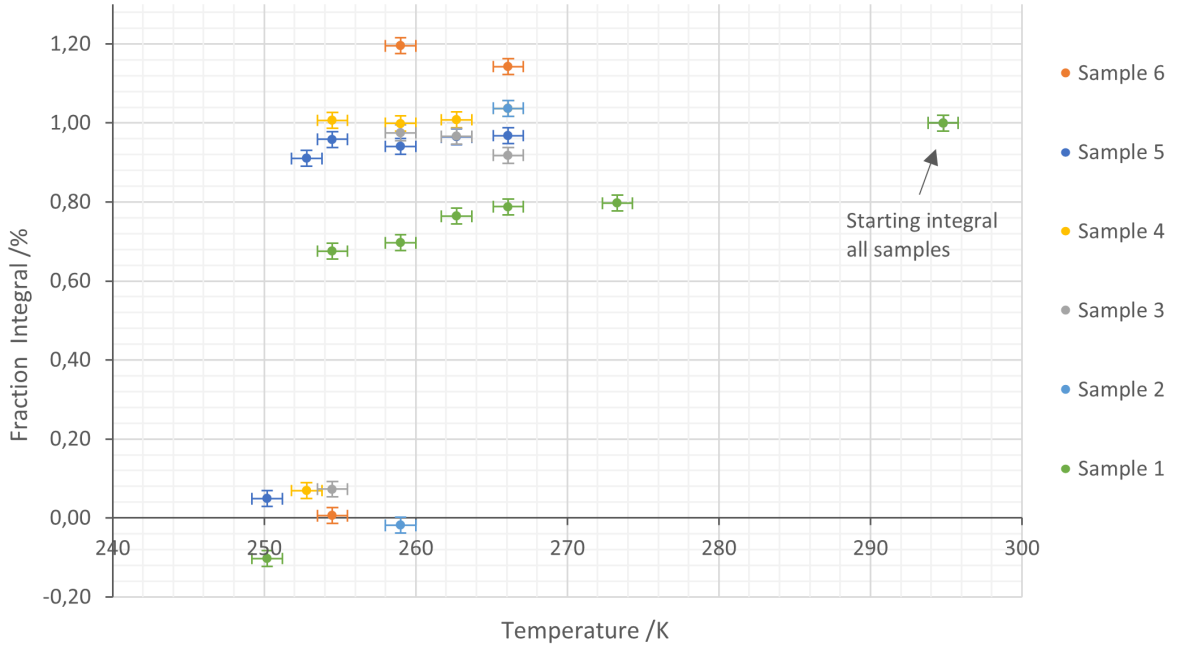

(a) Smooth sapphire

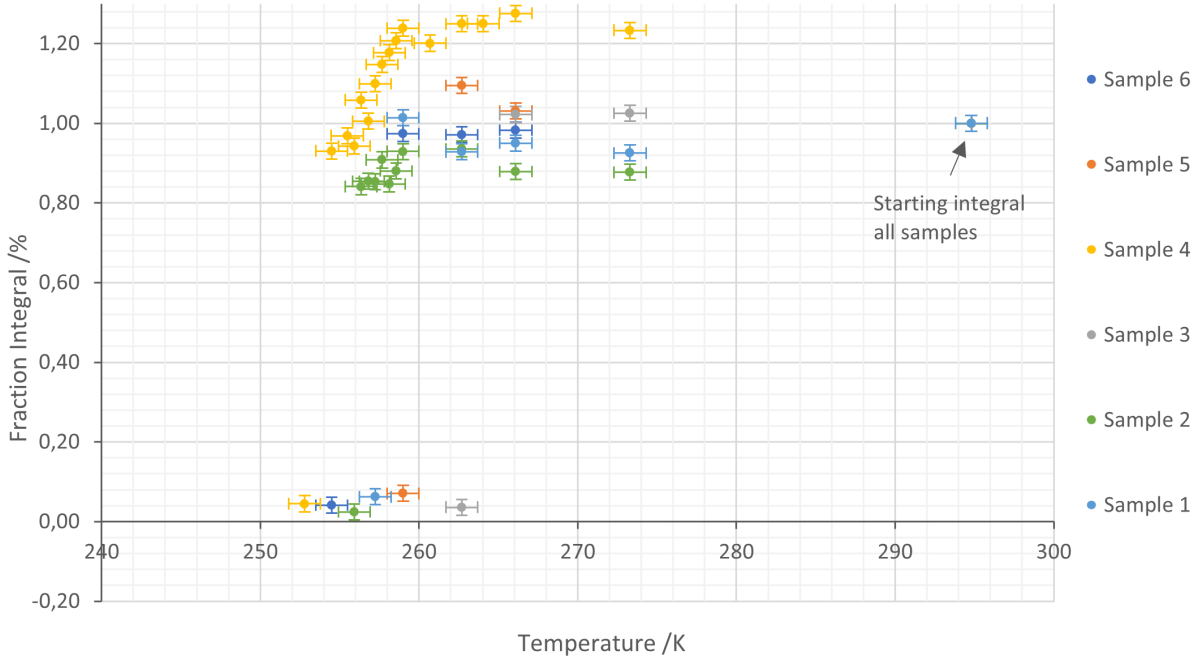

(b) Rough sapphire

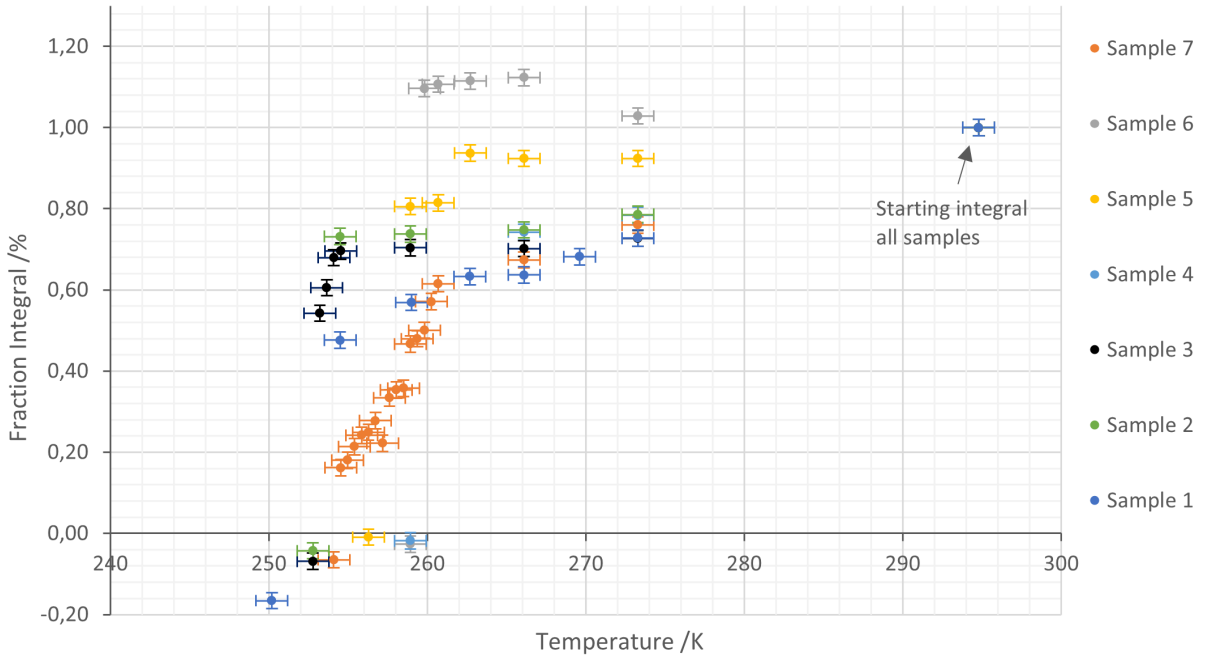

(c) Smooth silica

Figure 5.18: The points show the integral beneath the water peak, recorded at a specific temperature, as a relative fraction integral to its starting point, which is set as 1. These plots show the variation of water volume for each sample when the temperature is lowered.

Figure 5.18a shows the fraction integral beneath the NMR spectra at a specific temperature relative to its starting point. As known from Section 3.1.1 intensity of the spectra reflects the amount of absorbed intensity, indicating that a peak at a particular chemical shift is caused by a higher amount of protons at that exact shift. The relatively broad peaks indicate protons in several environments. Thus changes in the integral can relate to the water volume.

The general observations for the majority of the smooth sapphire samples are the minor changes in fraction integral before a sudden drop at the freezing point. For sample 1, the fraction integral gradually decreases (up to 30 %), which is more in line with trends observed for the silica samples (trend type 2). Whereas sample 6 shows a slight decrease before the sudden drop at the freezing point. The pattern of small changes in integral before a sudden drop corresponds with the observations for rough sapphire and silica. Some of the smooth silica samples also show a gradual decrease in integral. However, the latter must be seen in relation to the lower quality noise subtraction for the silica samples, which may have impacted these trends.

The most interesting observation is that the rough sapphire samples 2 and 4 with tight temperature intervals near the freezing point show a more significant reduction in the fraction integral. This substantiates the observation in the trend in Figure 5.16a, indicating that parts of the water freeze at lower temperatures near the point of total freezing. The same observation is made for some of the smooth silica samples (3 and 7) in Figure 5.18c.

Note that the data points do not lie precisely at zero and even show a slightly nega-

tive fraction integral for some at the freezing point. As seen from the spectra in Figure 5.22, signals in both positive and negative directions are impacted by the background signal subtraction, thus causing a negative integral in some cases.

Comparing the observations with Figure 5.17; the WHH broadens, and the integral decrease near the freezing point for the rough sapphire samples (2 and 4), supporting the assumptions of party freezing. This can also be observed for silica sample 7. Whereas silica sample 3 shows a decrease in both integral and WHH near the freezing point. This is probably due to the volume decrease in the right shoulder of the spectra, as seen in 5.16b.

Chemical Shift

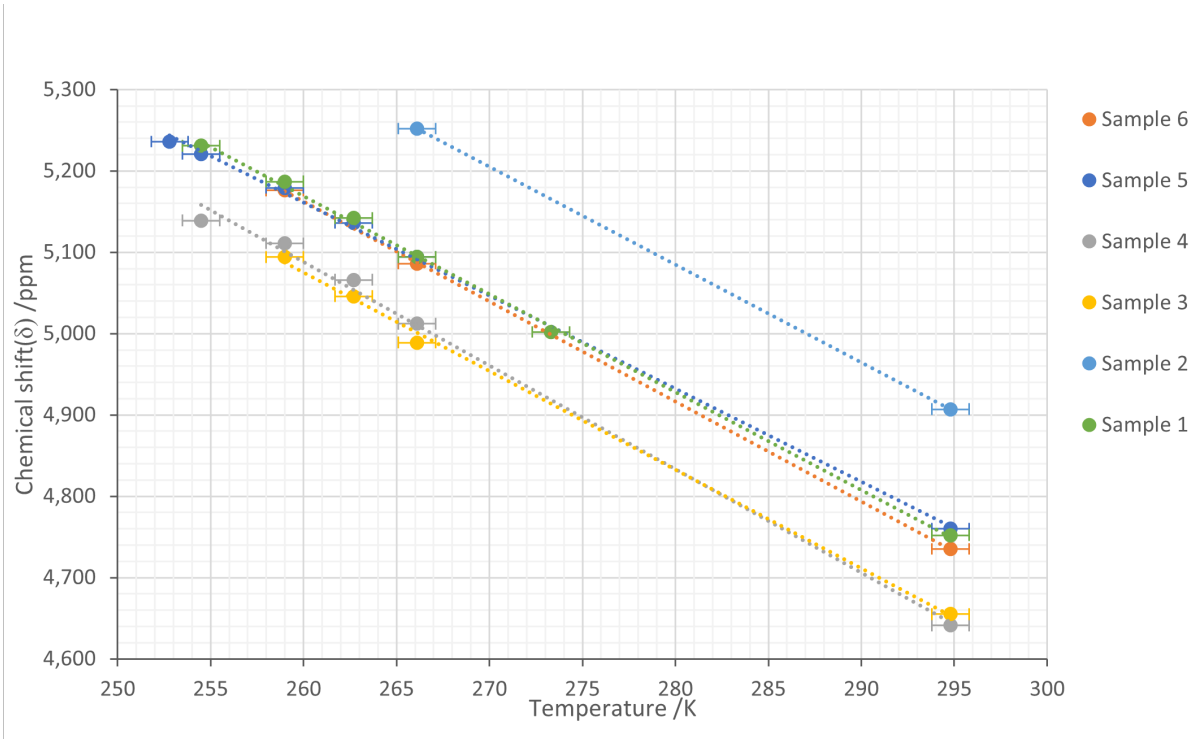

Figure 5.19: Smooth sapphire: Temperature dependence on chemical shift for six samples of water on smooth sapphire. The chemical shift value is determined using the left straight line of the peak to reduce the uncertainty in measurements caused by the fine structure of the spectra (see details in Appendix B.2). The dotted line is a trend line with values listed in Table 5.5

Table 5.5: Linear trends of chemical shift variations of water on smooth sapphire. The trend-line slope with standard deviation and R-squared is calculated by the use of regression analysis (see Appendix B.3).

Date	Trendline	Slope	R^2
Sample 6	y=-0.0123x+8.36	$(-1229 \pm 7) \cdot 10^{-5}$	1.000
Sample 5	y=-0.0115x+8.14	$(-115 \pm 2) \cdot 10^{-4}$	0.999
Sample 4	y=-0.0127x+8.4	$(-127 \pm 5) \cdot 10^{-4}$	0.9961
Sample 3	y=-0.0121x+8.2	$(-121 \pm 4) \cdot 10^{-4}$	0.9982
Sample 2	y=-0.0120x+8.4508	(-0,0120	1.000
Sample 1	y=-0.0120x+8.30	$-0.0120 \pm 4 \cdot 10^{-4}$	0.9991
Average		$-0.0121 \pm 4 \cdot 10^{-4}$	$0.999 \pm 1 \cdot 10^{-3}$

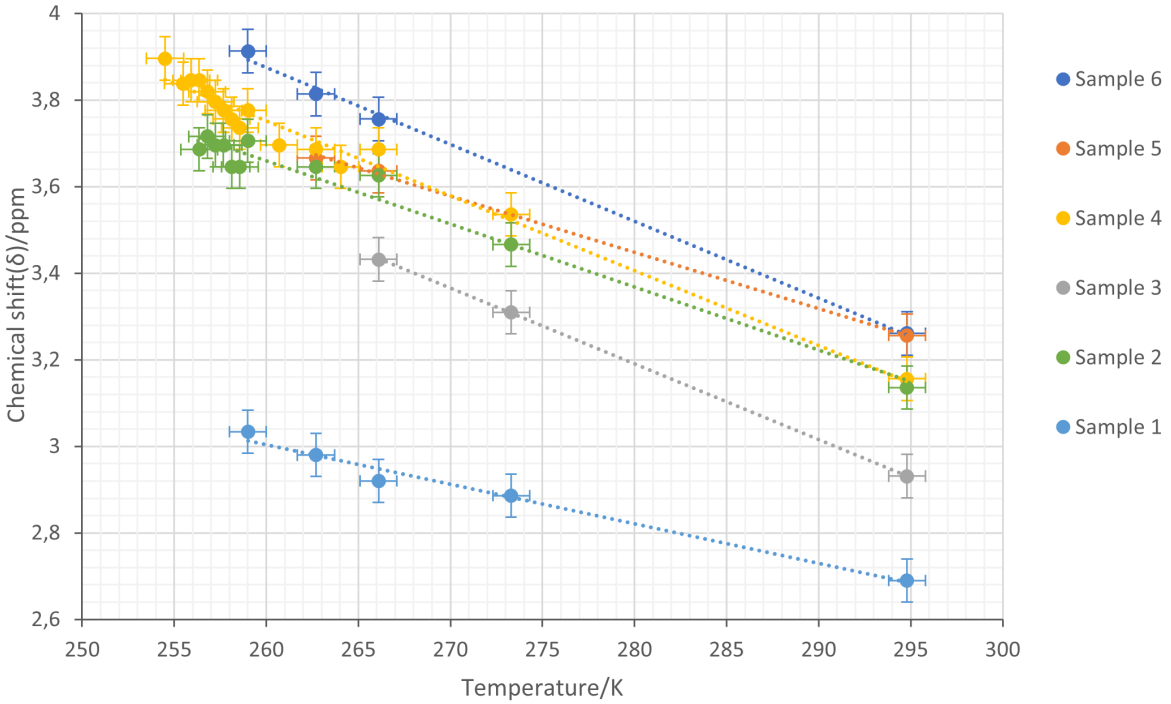

Figure 5.20: Rough sapphire: Temperature dependence on chemical shift for six samples of water on rough sapphire. The top points of the spectra were used to determine the chemical shift, which includes the uncertainty of the top point broadness (see details in Appendix B.2). The dotted line is a trend line with values listed in Table 5.6

Table 5.6: Linear trends of chemical shift variations of water on rough sapphire. The trendline slope with standard deviation and R-squared is calculated by the use of regression analysis (see Appendix B.3).

Date	Trendline	Slope	R^2
Sample 6	y=-0.0177x+8.5	$(-177 \pm 7) \cdot 10^{-4}$	0.9972
Sample 5	y=-0.015x+7.3	$(-15 \pm 2) \cdot 10^{-3}$	0.9808
Sample 4	y=-0.0175x+8.09	$(-175 \pm 1) \cdot 10^{-4}$	0.9999
Sample 3	y=-0.0173x+8.2	$(-173 \pm 8) \cdot 10^{-4}$	0.9733
Sample 2	y=-0.0146x+7.5	$(-146 \pm 9) \cdot 10^{-4}$	0.9700
Sample 1	y=-0.0092x+5.4	$(-92 \pm 7) \cdot 10^{-4}$	0.9817
Average		$(-15 \pm 3) \cdot 10^{-3}$	0.98 ± 0.01

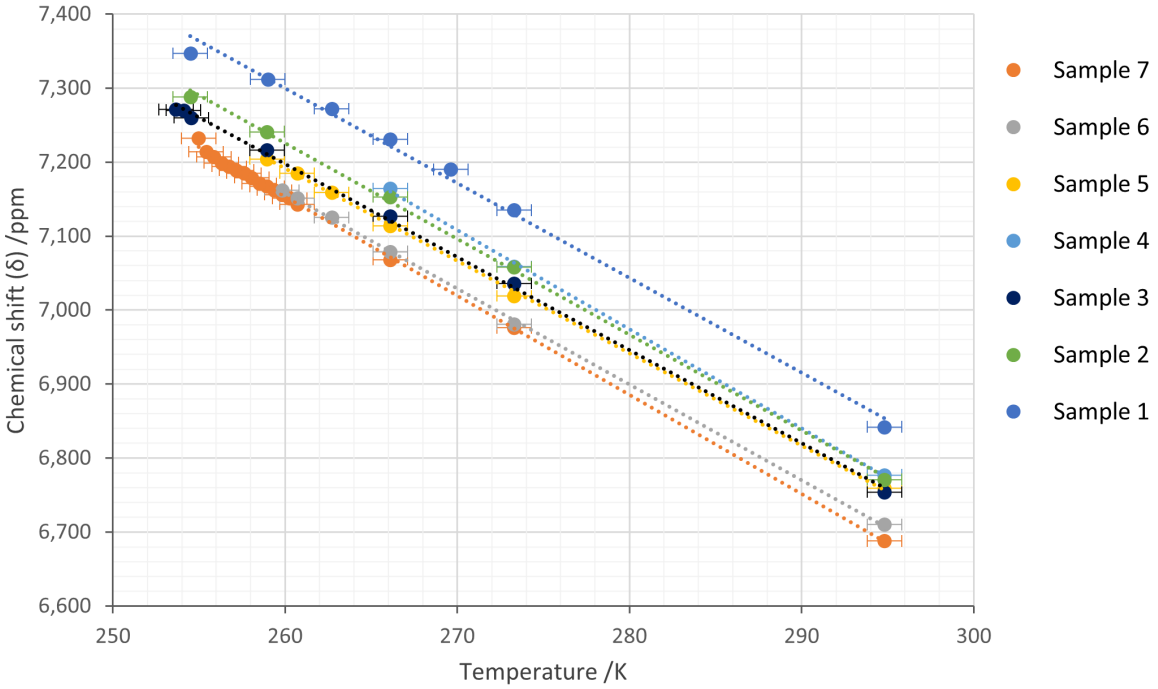

Figure 5.21: Smooth silica: Temperature dependence on chemical shift for seven samples of water on smooth silica. The chemical shift value is determined using the left straight line of the peak to reduce the uncertainty in measurements caused by the fine structure of the spectra (see details in Appendix B.2). The dotted line is a trend line with values listed in Table 5.7

Table 5.7: Linear trends of chemical shift variations of water on smooth silica.The trend-line, slope with standard deviation and R-squared is calculated by the use of regression analysis (see Appendix B.3).

Date	Trendline	Slope	R^2
Sample 7	y=-0.0134 x+10.65	$(-134 \pm 1) \cdot 10^{-4}$	0.9989
Sample 6	y=-0.0129x+10.52	$(-129 \pm 1) \cdot 10^{-4}$	0.9997
Sample 5	y=-0.0125x+10.43	$(-125 \pm 1) \cdot 10^{-4}$	0.9996
Sample 4	y=-0.0134x+10.73	$(-134 \pm 3) \cdot 10^{-4}$	0.9995
Sample 3	y=-0.0125x+10.45	$(-125 \pm 2) \cdot 10^{-4}$	0.999
Sample 2	y=-0.0129x +10.59	$(-129 \pm 2) \cdot 10^{-4}$	0.9991
Sample 1	y=-0.0128x+10.60	$(-128 \pm 4) \cdot 10^{-4}$	0.994
Average		$(-129 \pm 4) \cdot 10^{-4}$	$(999 \pm 2) \cdot 10^{-3}$

The figures 5.19-5.21 above show the chemical shift plotted against the temperature, thus showing the change in chemical shift as the temperature is lowered. For smooth sapphire (Figure 5.19) and smooth silica (Figure 5.21), the change in chemical shift has a high degree of linearity with all the samples having nearly the same slope, but with some varies in starting points. The deviations in starting point may be caused by drift in the magnetic field or impurities, as explained in sections 5.3.1-5.3.3. The silica surface shows a slightly steeper slope than the smooth sapphire surface.

Compared to rough sapphire samples shown in Figure 5.20, the change in chemical shift is less linear. This may be due to the challenge and uncertainty in determining accurate chemical shift values. The average slope of the trend lines, given in table 5.8, reveals a higher average slope than for the smooth surfaces and higher uncertainty.

Table 5.8: The average measured change in chemical shift per Kelvin for water on Smooth silica, Smooth sapphire and Rough sapphire compared to theoretical values for bulk water [67]

Surfacetype	Smooth silica	Smooth Sapphire	Rough sapphire	Bulk Water
$\Delta\delta$/K	$-0.0129 \pm 4 \cdot 10^{-4}$	$-0.0121 \pm 4 \cdot 10^{-4}$	$-0.015 \pm 3 \cdot 10^{-3}$	-0.01 [67]

The results for smooth sapphire and smooth silica coincide well with the behaviour observed for bulk water, with a slope of -0.01 ppm/K. Hence, an LDW structure is favoured for water at lower temperatures. This also aligns with the findings of freezing interfacial water on silica by gunko et.al [29]. However, it contradicts the study by Totland et al. [28], who found the opposite for the same setup as in this thesis, but at higher temperatures (278-313 K). The deviations from Totland et al. [28] might be due to the differences in the temperature range. Generally, supercooled water is predicted to shift higher as the water becomes more rigidly structured, which aligns well with the findings in this thesis. Rough sapphire has a steeper average slope, which may have been caused by the uncertainty in measuring chemical shift.

Quasi Liquid Layer

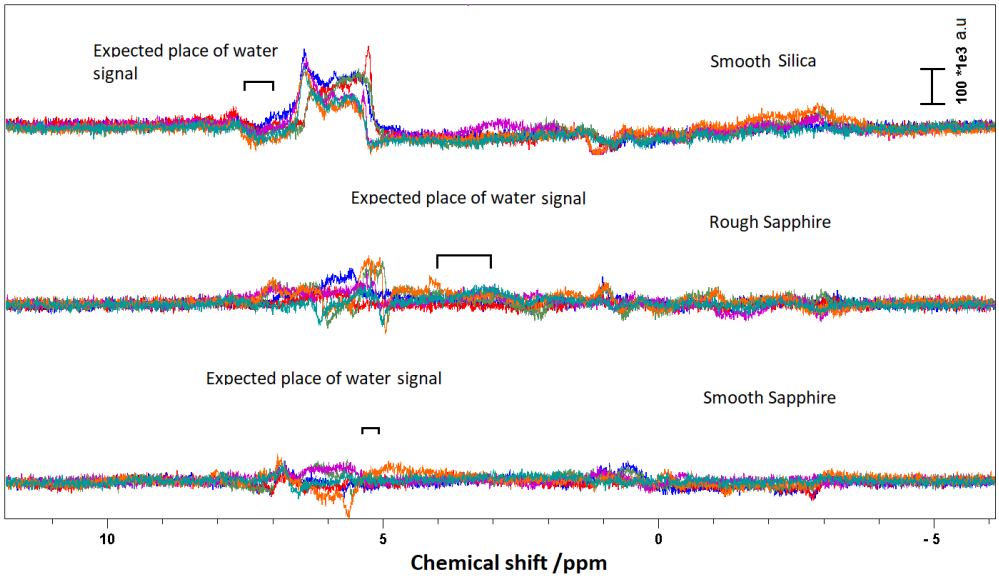

Figure 5.22: Comparison of all freezing spectra with expected range of water signal.

Figure 5.22 shows spectra of frozen water for all the samples recorded laid on top of each other for each of the three different surface types. The original aim of the thesis has been to look for a potential quasi-liquid layer after freezing. The bars present the expected range for where such a water signal would appear. Calculations for the predicted ranges are found by the use of the calculated trend line presented in Table 5.5,5.6 and 5.7.

As seen in the figure, the expected area for the water signal is an area with a significant noise signal. Thus, making it impossible to interpret the appearance of a water signal. Spectra for smooth silica generally have more signal in this area than for the sapphire samples. The difference in signal intensity is due to the silica samples missing the appropriate noise subtraction introduced later for the sapphire samples (see section 4.3.7). Ideally, all background noise would be removed by subtracting a stable reference background signal recorded at the same temperature, leaving only the signal from the sample. However, this is not feasible, as small changes in phase and intensity between spectra occur even within the same day of recording.

It is also worth mentioning that these spectra are recorded using a T_2-filter (section 4.3.3). Thus, the risk of filtering out parts of the actual sample signal can not be ruled out with certainty.

5.4 Macroscopic Freezing Onset Measurements

The macroscopic freezing onset measurements were performed for single and double plate samples, as described in section 4.4.2. Snapshot images of the interfacial water on samples before and after freezing can be seen in Figure 5.23 - 5.25.

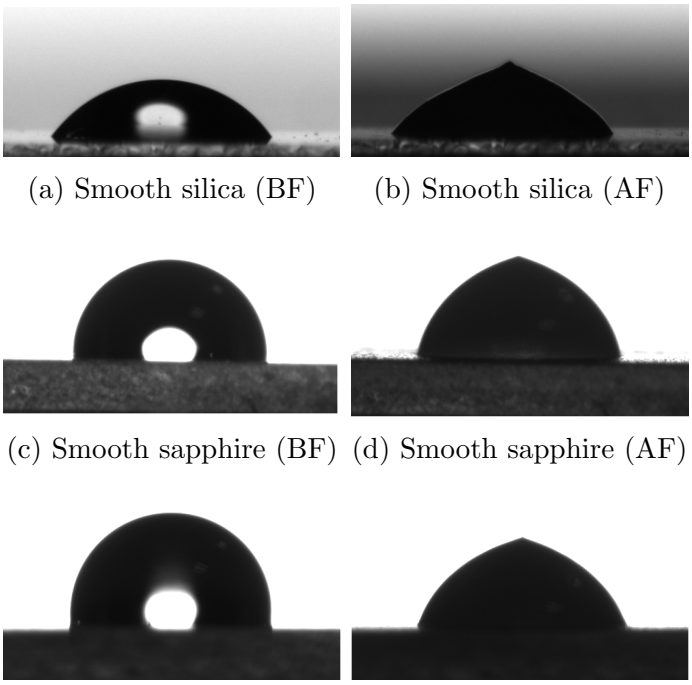

(a) Smooth silica (BF) (b) Smooth silica (AF)

(c) Smooth sapphire (BF) (d) Smooth sapphire (AF)

(e) Rough sapphire (BF) (f) Rough sapphire (AF)

Figure 5.23: Snapshot of $2\mu L$ water droplet on smooth silica (a) and b)), smooth sapphire (c) and d)) and rough sapphire (e) and f)). The left-sided pictures (a,c and e) are recorded before freezing (BF) at 20 °C and the right-sided are recorded after freezing (AF) (at temperatures below freezing point) (b),d) and f). All the surfaces are washed with isopropanol

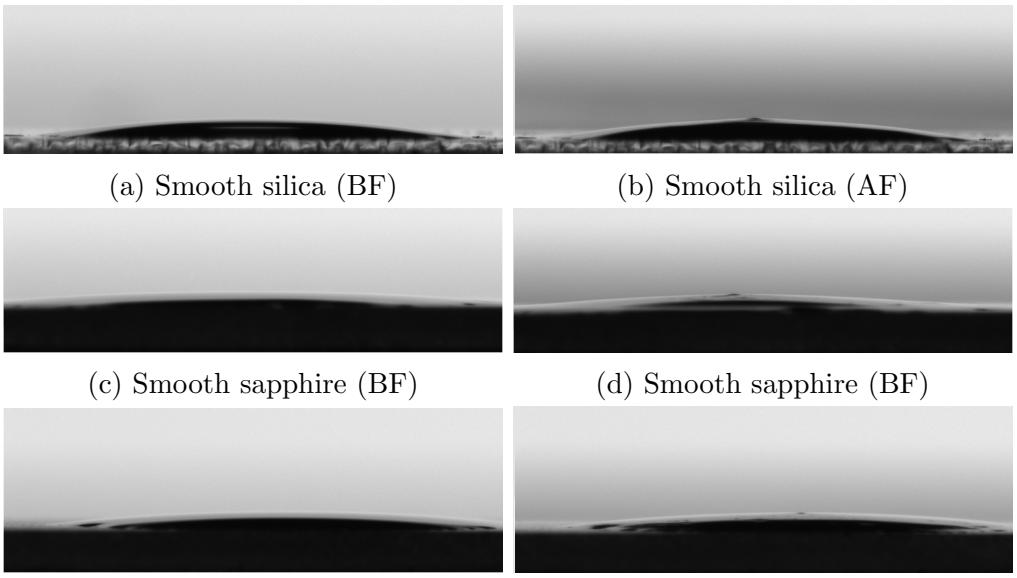

(a) Smooth silica (BF) (b) Smooth silica (AF)

(c) Smooth sapphire (BF) (d) Smooth sapphire (BF)

(e) Rough sapphire (BF) (f) Rough sapphire (AF)

Figure 5.24: Snapshot of $2\mu L$ water droplet on smooth silica (a) and b)), smooth sapphire (c) and d)) and rough sapphire (e) and f)). The left-sided pictures (a,c and e) are recorded before freezing (BF) at 20 °C and the right-sided are recorded at temperatures below freezing point (AF) (b),d) and f). Surfaces are washed and etched.

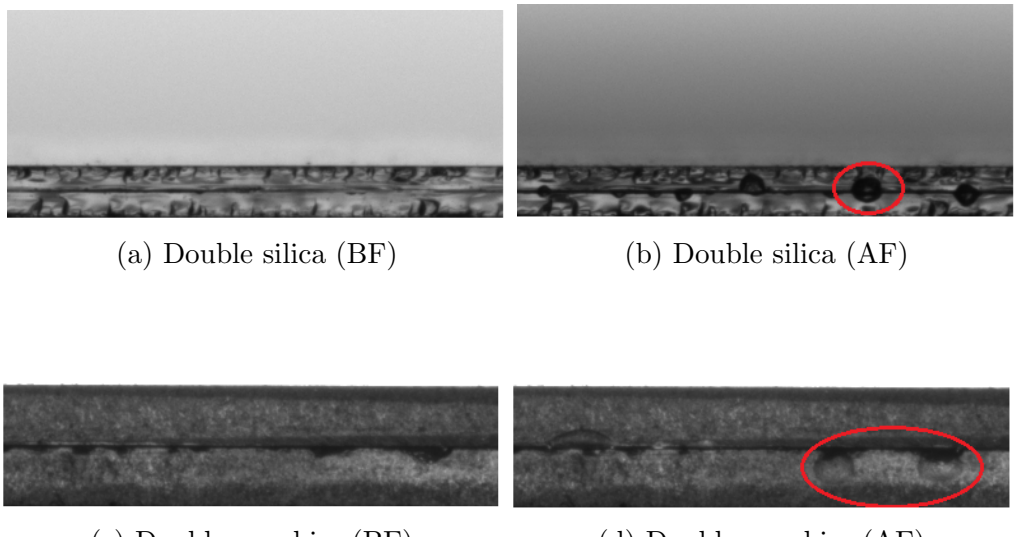

(a) Double silica (BF) (b) Double silica (AF)

(c) Double sapphire (BF) (d) Double sapphire (AF)

Figure 5.25: Freezing of water 1.2 ± 0.4µL between double plates. a) and b) show water between silica plates, c) and d) water between sapphire plates. Left pictures were taken before freezing (BF) at room temperature and c) and d) after freezing (AF). Freezing was observed when water leaked out of samples plates (red circle in b) and d))

Figure 5.26 shows an outline of all the collected freezing onset temperature measurements, presented together with the freezing temperature measurements from the NMR experiments.

The freezing onset measurements were performed 3-4 times on each sample, whereas the NMR measurements were performed one time per sample. The total amounts of temperature measurements are summarised in Table 5.9.

The variations in relative humidity, as shown in Figure 5.26, occurred due to a broken humidifier in the cleanroom and experiments performed on different days. The humidity conditions for the NMR measurements are unknown as there was no humidity detector in the area. Especially the micro-climate in the gap between the two plates used in the experiment was hard to evaluate. As mentioned in section 4.4.1, the first freezing onset measurements on loosely washed sapphire samples were done in the standard lab, whereas the rest were performed in the cleanroom, including freezing onset on smooth silica.

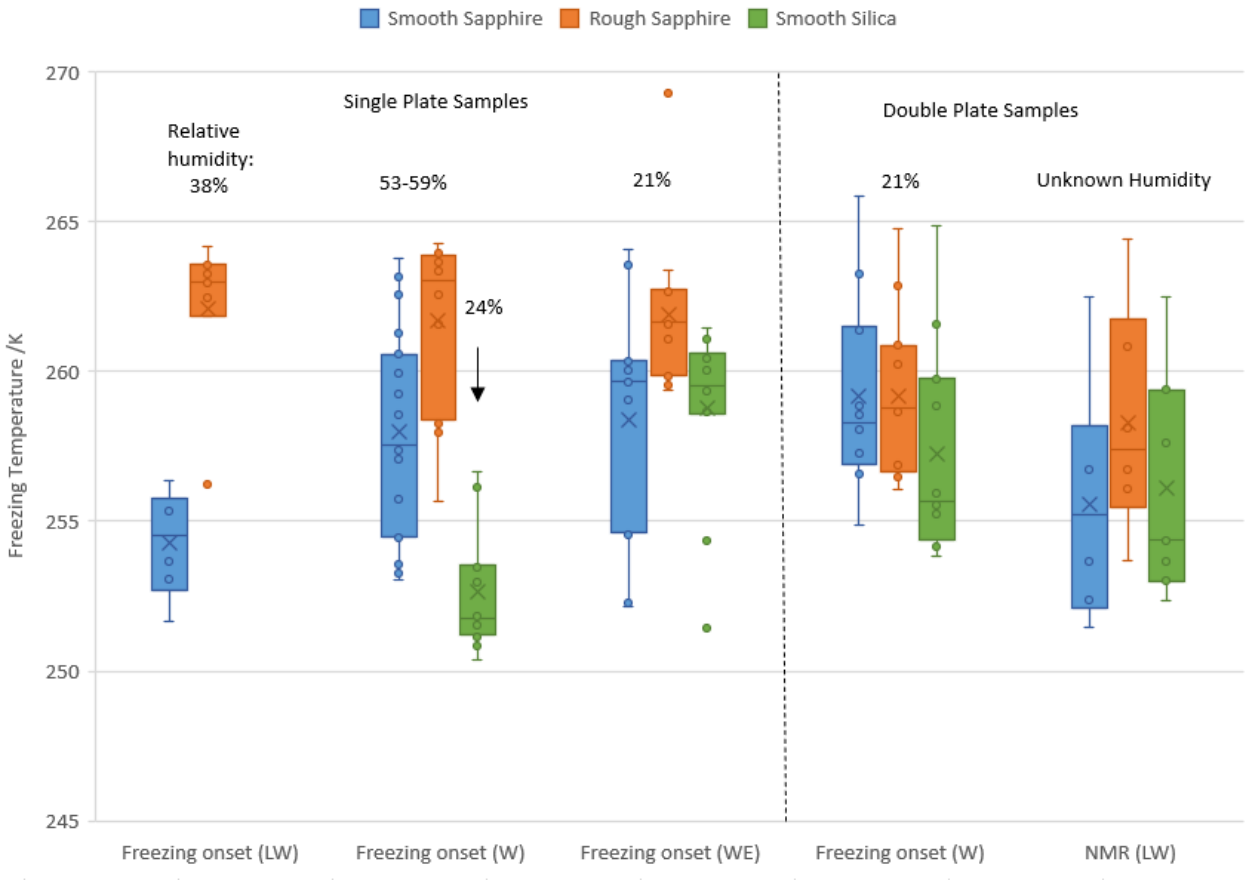

Figure 5.26: A boxplot of the water freezing temperatures on different samples, methods and sample preparations (loosely washed (LW), washed (W) and washed and etched (WE)). Single points indicate the freezing temperature measurement values. Each cross represents the average value, and the middle line is the median. The lower and upper box borderlines are the first and third quartiles (1Q/3Q), respectively, in which 25% and 75% of the data are below these points. The lower and upper whiskers represent the minimum and maximum values. The minimum value is defined as the difference between 1Q and 1.5 of the box range, and the maximum value as the sum of 3Q and 1.5 of the box range. Single points outside these whiskers are considered to be outliers.

Table 5.9: Freezing measurements results for smooth sapphire, rough sapphire and smooth silica surface. Listed is the total number of measurements (No. of meas.), where each sample is measured 3-4 times for freezing onset and one time in NMR. The table also lists relative humidity and average and median freezing temperature. * is calculated with propagation of error, weighted mean and weighted standard deviation (see Appendix B.3)

Surface	Method	No.of meas.	RH (%)	Average (K)	Median (K)
Smooth sapphire	Freezing onset (LW)	6	38	254 ± 2	254.5
	Freezing onset (W)	19	53-59	258 ± 3	257.6
	Freezing onset(WE)	12	21	258 ± 4	259.7
	Freezing onset(W)(Double)	12	21	259 ± 3	258.3
	NMR (LW)*	6	-	254 ± 3	255.2
	NMR (LW)	6	-	256 ± 4	255.2
Rough sapphire	Freezing onset (LW)	7	38	262 ± 3	263.0
	Freezing onset(W)	14	53-59	262 ± 3	263.0
	Freezing onset(WE)	12	24	262 ± 3	261.7
	Freezing onset(W)(Double)	12	21	259 ± 3	258.8
	NMR (LW)*	6	-	257 ± 5	257.4
	NMR(LW)	6	-	258 ± 4	257.4
Smooth silica	Freezing onset(W)	12	24	252 ± 2	251.7
	Freezing onset(WE)	12	21	259 ± 3	259.5
	Freezing onset(W)(Double)	11	21	258 ± 3	255.8
	NMR (LW)*	7	-	255 ± 3	254.4
	NMR(LW)	7	-	256 ± 4	254.4

Single Plate Samples

For the single plate samples in Figure 5.26, it can be observed that the rough sapphire samples generally are more ice promoting than the flat surfaces, regardless of sample preparation and humidity conditions. Rough sapphire also shows a smaller spread in data points than the smooth samples, thus indicating that roughness is a more significant contributor to ice formation than external factors such as humidity and preparation regime. This can also be seen more clearly in the scattered plot of all the data points in Figure A.6. The results show an increase in the temperature range for the washed samples compared to the loosely washed with lower relative humidity. However, this does not change the average and median values and might be a statistical factor due to differences in the number of measurements.

The measurements for smooth sapphire show a more disordered set of data points. The loosely washed samples at 38% relative humidity show low freezing temperatures averaging $254 \pm 2\ K$ with a tight temperature range. The washed samples, recorded at a higher relative humidity range of 53-59%, had a freezing temperature average of $258 \pm 3\ K$ and a greater spread in data points. Which corresponds well with reported freezing onset measurements for flat sapphire of 259±1K at 50-55%RH [4]. The same trend can be observed for the washed and etched samples at low relative humidity (21%), also showing a more clustered set of freezing points than the washed samples (see Figure A.6 in Appendix (A.4)). It is worth

noticing that the difference between these measurements is the sample preparation regime, relative humidity and number of measurements. It is known that higher humidity might have a promoting effect on ice formation [88], and according to CNT, enhanced wettability should have a promoting effect, even though this is still debated [49]. However, this might also be due to statistical factors, as loosely washed samples have fewer measurement points.

The smooth silica measurements are quite similar to the smooth sapphire measurements. The washed sample at 24% relative humidity shows a low freezing point in the same range as for smooth sapphire (LW) with a tight spread. However, since these samples are recorded at different humidity (24% and 38%) they are not directly comparable. The washed and etched samples have a higher freezing temperature and a wider freezing range, similar to the smooth sapphire with the same washing procedure, causing both to be superhydrophilic. This is better observed in the scattered plot in Figure A.6. The differences in freezing point for the silica samples might be explained by the enhanced hydrophilicity, as the relative humidity is nearly the same (21% RH-24%RH) for silica (W) and the silica (WE) samples.

According to CNT, the rough sapphire samples would be expected to have a higher proportion of pits with radius curvature $< 10r_c$. However, the analysis in section 5.1 shows that rough and smooth sapphire have a similar distribution, with most curvatures exceeding this range and having a similar proportion of positive curvatures. Table 5.2 shows that the rough sapphire has a slightly higher distribution of curvature radius below $10r_c$. As only one nucleation site is needed for nucleation to start, it can thus be argued that the probability of contact between a droplet and a potential nucleation site is larger for the rough sapphire sample. However, the washed and etched silica samples had the most significant proportion of pits below $10r_c$, despite having the lowest proportion of pits. This could be due to the much higher resolution of the AFM image for silica. The differences in image resolution thus also imply an uncertainty in how much the rough sapphire curvature analysis can be emphasized (as explained in section 5.1).

Double Plate samples

For the measurements on the double plate samples, the registered freezing temperatures can not be distinguished between smooth and rough sapphire, which is the opposite of observations for single plate samples. Additionally, the smooth silica samples generally show a lower temperature average and median than the sapphire samples. This is contrary to what's expected from CNT as silica is more hydrophilic than sapphire. It should be mentioned that numerous freezing onset measurements had to be performed on the silica samples to achieve a result, as about half of the samples showed no observable freezing. It is also worth mentioning that the double plate sample is in a different environment, as the water layer has a greater contact area with the surface and is significantly less affected by the surrounding air and thus airflow and surrounding humidity conditions. In fact, humidity conditions between the plates are likely to be close to saturation since the water layer measured is clamped between two surfaces. The water layer also has a lower volume, which has been reported to impact the freezing [43]. The silica sample plates are 2 mm longer than the sapphire, which will affect the thickness of the water layer. The samples are therefore not necessarily directly comparable with the single plate samples.

Comparing the freezing temperatures with the NMR results, the NMR measurements

showed a higher freezing temperature for rough sapphire, distinguishing it from both the smooth samples. However, as observed for the single plate samples, all three surface types have a wide range of freezing temperatures. The humidity conditions are not specified as discussed above but can be regarded as saturated as for the double plate freezing onset measurements. The freezing temperature measurements performed in the NMR experiments have significant uncertainty, as seen in Figure A.6 in Appendix (A.4). This uncertainty is partly due to the temperature calibration and partly to potential gaps between actual freezing temperatures and recorded spectra as explained in section 4.3.4. Thus the temperature data may be unsuitable to use as freezing point measurements. However, it is worth mentioning that these freezing points are still within the temperature ranges observed in the freezing onset measurements.

Chapter 6

Discussion

The main aim of this thesis has been to investigate ice formation on surfaces with two very different surface finishes (smooth and rough) and evaluate it according to the modified nucleation theory.

The results showed a difference in freezing temperature for the rough versus the smooth sapphire surface sample. The curvature radius analysis did show a higher proportion of pits with radii below $10r_c$ for rough sapphire compared to smooth sapphire and silica (LW). The scan sizes were in these cases comparable. This follows the trend expected for CNT. However, the curvature radius analysis may have potential sources of errors to be considered, which may reduce the reliability of the analysis, including the resolution of the AFM measurements. Additionally, the amount of radius curvature (belonging pits) below $10r_c$ is only a minor fraction ($< 1\%$) of the total measuring points.

The study by Eberle et al. [16] on surface samples with RMS ranging from 0.17-173 nm, presented two examples of high resolution curvature radius analysis, one with and one without proportion below $10r_c$. These results showed that the proportion $< 10r_c$ did not impact the freezing temperature. The proposed reason for this was that a QLL counteracted the pits. However, the findings in this thesis do not align with Eberle et al. [56] findings but are not necessarily contradictory either. There are many factors to be considered that can potentially impact the freezing process and thus result in diverging results between different studies, some of which will be further discussed below.

Comparing the results with the findings in the Master thesis by Løvås [86] shows relatively similar results as for this thesis for the two diamond samples with RMS 9 nm and 560 nm measured at 40-100 % relative humidity. The freezing measurements in Løvås thesis [86] were also shown to be significantly impacted by the humidity and airflow, factors that are also reported to have an impact by other studies [88, 89].

The results in this thesis diverge from the Løvås thesis [86] for measurements at low relative humidity (20-40 %), with a difference in freezing temperature between rough and smooth samples contrary to the results of Løvås [86]. However, some possible contributing measurement conditions must be taken into consideration. Firstly, the Løvås thesis [86] does not present any radius curvature analysis, which is highly relevant information in the comparison. Secondly, the measurements performed at 21 % RH were on washed and etched samples, which makes the surface superhydrophilic. The CNT states that hydrophilicity can promote ice nucleation due to the lowered Gibbs energy and the enlarged contact area

between water and surface, but some studies show deviating results.

However, roughness is generally considered a more influential factor in ice nucleation than wetting properties. In the article by Eberle et al. [16], the sample wetting properties did not significantly impact the results. The article by Akhtar et al. [4] found the opposite, where the hydrophilicity did show a significant promoting effect on ice nucleation. In this thesis, there are not enough data measured with the same conditions to generally evaluate this aspect for these samples. The samples that were comparable showed deviating results. On the one hand, it can be argued that the silica samples (W and WE) measured at 24% RH and 21% RH, respectively, showed a promoting effect due to the changed wetting properties. While freezing onset of double plate samples showed a tendency for the more hydrophilic silica to freeze at lower temperatures than the sapphire samples.

It is worth noticing that Eberle et al. [16] show a referenced aluminium sample with a significantly higher freezing temperature than the rest of the samples. The aluminium sample is hydrophilic with an RMS value of 150 nm, thus inside the range (0.17-173 nm) of the other samples that did not show differences in freezing temperature. Eberle et al. [16] argues that because other studies have found QLL present on hydrophilic SiO_2 and hydrophobic alkylsilanes, it also has to be present on samples used in this study. Following that argument, the QLL should thus also be present on the aluminium reference sample.

Other studies have shown that the thickness of a QLL is temperature depended, in addition to the wetting properties of the sample material and pore sizes [25, 27]. If the QLL counteracts the pits, the question arises if the broadness of the pits, chemical composition and wetting regimes will impact the counteracting effect of QLL. As there are so many potential contributing factors, it is challenging to accurately determine which of these factors come into effect at this stage. Preferably, a more thorough investigation would be conducted where only one of these factors is varied at a time for different samples with a less complex structure.

One of the aims of this thesis was to investigate the potential existence of a QLL at the ice-surface interface. NMR spectroscopy was chosen as a method because of the possibility of measuring the remaining water in the sample as the ice becomes invisible to the probe head and its ability to investigate water diffusion. The NMR was done by applying the methode by Totland et al. [28] with water between surface plates and using a rare flat coil probe head. The flat coil allowed for larger samples than the regular MAS probe head, and the water between plates allowed for the investigation of surface impact on water with less impact of vapor interface and gas flow. It also allowed for a larger volume of interfacial water than in other NMR studies that used either a few monolayers of water or bulk water, which can be hard to distinguish from interfacial water. However, some complicating factors using this method were less control of the micro climate, unknown pressure between plates and possible increased magnetic field inhomogeneities due to the plates or water layer. Thus, it would have been interesting to test droplet signals on a single plate with more familiar conditions and thus more comparable with the freezing onset measurements. One sample was tested this way, confirming that this method should work, but unfortunately, there was no time for more extensive investigations.

The unexpected appearance of background noise and the numerous issues related to the mitigation attempts resulted in inconclusive results concerning the investigation of QLL. As explained above, the method used is presumably a suitable application in investigating

QLL, but with a prerequisite of sufficiently eliminating the background noise, which was not achieved in this thesis. It could be an idea to test and compare other suitable methods used in studies that have found traces of interfacial water, including X-ray diffraction [21] and reflectivity [20,90], Differential Scanning Calorimetry (DSC) [91] and total internal reflection (TIR) Raman spectroscopy [92].

Despite the inconclusive results in the QLL investigations due to all the mentioned challenges, the NMR measurements did show interesting results related to the freezing process and water mobility. The silica samples were shown to be more hydrophilic than the sapphire sample, which was confirmed by the contact angle measurements. Furthermore, the NMR spectra showed differences in shape and broadness of the water peak for the rough sapphire samples versus the smooth samples. This may be due to the interfacial water being more bound to the rough sapphire surface, resulting in less water mobility.

The freezing measurements showed that the water gets gradually more structured with increases in the chemical shift when lowering the temperature, indicating a shift towards LDW structure. Especially interesting are the four samples of rough sapphire and smooth silica that showed partly freezing near the freezing point. This was substantiated by the gradual drop in integral, indicating the amount of water transitioning to ice and by the increase in WHH, indicating less mobile water molecules. The partly freezing suggests that there are local variations within the interfacial water affected by the surface, freezing at different stages. A study by Totland et al. [28] showed that the effect of surface forces on the interfacial water between silica plates were in the order of micrometres. And as mentioned in section 2.1, it is believed that the forces will cause a cascade effect that will reorient the successive layers of water molecules [24].

As mentioned in section4.4.2, the nucleation of a droplet occurs very fast, almost instantly. However, the partly freezing found in the NMR experiments happened in an extended period of time, with around 30 minutes between each recording. Unfortunately, no appropriate studies were found for comparison. There are freezing-out layer-by-layer NMR studies that show freezing in several stages. However, these are either only a few monolayers thick water layer [29, 87] or in a bulk water environment [23, 24]. Additionally, the results only show freezing out in larger temperature gaps (typically 5 K) [23, 24] and not in the incremental temperature steps (0.5 K) near the freezing points as done in this thesis.

Chapter 7

Conclusion and Further Work

This thesis aimed to investigate ice formation on smooth and rough sapphire surfaces that allude to the proposed modified nucleation theory by investigating the potential presence of a QLL. This was done macroscopically with freezing onset and contact angle measurements and microscopically by NMR-spectroscopy and AFM.

The macroscopic freezing onset measurements of a sessile droplet on the sample surfaces showed a promoting freezing effect for the rough sapphire (RMS 120-180 nm) versus the nanostructured smooth sapphire (RMS 0.13-0.57) and smooth silica (RMS 0.59-4.3) at a relative humidity range of 20-60 %, across different washing regimes. The results also show that the smooth samples' freezing temperature is more affected by environmental conditions such as humidity, gas flow, and sample preparation than rough sapphire.

The proportions of pits are relatively similar for the rough and smooth samples, with the vast majority of curvature radii beyond $10r_c$. The rough sapphire shows a slightly higher proportion of curvature radii below $10r_c$ for comparable results, which could be in accordance with the expected freezing behaviour from the CNT. However, due to the significant uncertainties in the analysis, these results cannot be concluded to be either in accordance or contradictory to the CNT. And as the results show differences in freezing temperatures between the rough and smooth sapphire samples, the results of this thesis cannot substantiate the modified nucleation theory.

The investigation of the potential existence of QLL did not show any conclusive results due to the significant challenges with the background noise signal from the flat coil probe head. Thus, these results also could not substantiate the modified nucleation theory. However, the NMR results did show gradual freezing of water nearby the freezing point of water on rough sapphire and smooth silica, indicating water in different chemical environments.

7.1 Suggestions to Further Work

To expand the understanding of the surface freezing process and how the surface properties influence nucleation, the suggestion is to conduct several more freezing onset measurements combined with surface characterisation using AFM and curvature radius analysis. It is also recommended to further test and refine the curvature radius analysis, including enlarging the AFM image resolution, to ensure a more accurate and comparable analysis.

In this thesis, the sample surfaces consisted of two very smooth and one very rough sample. In retrospect, it would be recommended to have some ideally fabricated structured samples to enhance the characterisation accuracy and to eliminate some of the uncertainties, which could be used as a comparison. Another recommendation is to use more familiar crystallisations for better comparability with other studies in this field, as there are few studies on the potential effect of crystal orientation.

There are still many uncertainties regarding which factors affect the freezing temperature at this stage. To get control of the system and to increase the understanding of these factors, a suggestion would be to attempt to eliminate contributing factors one by one. More specifically by performing freezing onset measurements for samples of different compositions, roughness, sample preparations and wetting properties and in different external conditions, including humidity, gas flow, outer temperature, droplet positioning and with and without nitrogen.

In the investigations on the potential QLL, the flat coil probe head would only be recommended with a prerequisite of having adequate control of the background signal. The NMR investigations can also be tested using other probe heads, such as Magnetic Resonance Imaging (MRI) or MAS, though the latter only if a suitable sample can be created. Alternatively, investigate using other suitable techniques such as DSC, X-ray and Raman spectroscopy.

Bibliography

[1] M. Fitzner, P. Pedevilla, and A. Michaelides, "Predicting heterogeneous ice nucleation with a data-driven approach," *Nature Communications*, vol. 11, no. 1, pp. 1–9, 2020.

[2] Q. Li and Z. Guo, "Fundamentals of icing and common strategies for designing biomimetic anti-icing surfaces," *Journal of Materials Chemistry A*, vol. 6, no. 28, pp. 13549–13581, 2018.

[3] J. Lv, Y. Song, L. Jiang, and J. Wang, "Bio-inspired strategies for anti-icing," *ACS Nano*, vol. 8, no. 4, pp. 3152–3169, 2014. PMID: 24592934.

[4] N. Akhtar, G. Anemone, D. Farias, and B. Holst, "Fluorinated graphene provides long lasting ice inhibition in high humidity," *Carbon*, vol. 141, pp. 451–456, 2019.

[5] A. J. Meuler, J. D. Smith, K. K. Varanasi, J. M. Mabry, G. H. McKinley, and R. E. Cohen, "Relationships between water wettability and ice adhesion," *ACS Applied Materials and Interfaces*, vol. 2, no. 11, pp. 3100–3110, 2010.

[6] J. Laforte, M. Allaire, and J. Laflamme, "State-of-the-art on power line de-icing," *Atmospheric Research*, vol. 46, no. 1, pp. 143–158, 1998.

[7] M. I. Jamil, A. Ali, F. Haq, Q. Zhang, X. Zhan, and F. Chen, "Icephobic Strategies and Materials with Superwettability: Design Principles and Mechanism," *Langmuir*, vol. 34, no. 50, pp. 15425–15444, 2018.

[8] E. COMMISSION, "Communication from the commission to the european parliament, the council, the european economic and social committee and the committee of the regions." `https://ec.europa.eu/environment/pdf/chemicals/2020/10/Strategy.pdf`, 2020. Last accessed 16 September 2021.

[9] C. Li, R. Tao, S. Luo, X. Gao, K. Zhang, and Z. Li, "Enhancing and Impeding Heterogeneous Ice Nucleation through Nanogrooves," *Journal of Physical Chemistry C*, vol. 122, no. 45, pp. 25992–25998, 2018.

[10] S. A. Kulinich, S. Farhadi, K. Nose, and X. W. Du, "Superhydrophobic surfaces: Are they really ice-repellent?," *Langmuir*, vol. 27, no. 1, pp. 25–29, 2011.

[11] A. P. Esser-Kahn, V. Trang, and M. B. Francis, "Incorporation of antifreeze proteins into polymer coatings using site-selective bioconjugation," *Journal of the American Chemical Society*, vol. 132, no. 38, pp. 13264–13269, 2010.

[12] P. W. Wilson, W. Lu, H. Xu, P. Kim, M. J. Kreder, J. Alvarenga, and J. Aizenberg, "Inhibition of ice nucleation by slippery liquid-infused porous surfaces (SLIPS)," *Physical Chemistry Chemical Physics*, vol. 15, no. 2, pp. 581–585, 2013.

[13] J. Chen, R. Dou, D. Cui, Q. Zhang, Y. Zhang, F. Xu, X. Zhou, J. Wang, Y. Song, and L. Jiang, "Robust Prototypical Anti-icing Coatings with a Self-lubricating Liquid Water Layer between Ice and Substrate," *ACS Applied Materials & Interfaces*, vol. 5, no. 10, pp. 4026–4030, 2013.

[14] P. Irajizad, M. Hasnain, N. Farokhnia, S. M. Sajadi, and H. Ghasemi, "Magnetic slippery extreme icephobic surfaces," *Nature Communications*, vol. 7, no. May, pp. 1–7, 2016.

[15] S. Jung, M. Dorrestijn, D. Raps, A. Das, C. M. Megaridis, and D. Poulikakos, "Are superhydrophobic surfaces best for icephobicity?," *Langmuir*, vol. 27, no. 6, pp. 3059–3066, 2011.

[16] P. Eberle, M. K. Tiwari, T. Maitra, and D. Poulikakos, "Rational nanostructuring of surfaces for extraordinary icephobicity," *Nanoscale*, vol. 6, no. 9, pp. 4874–4881, 2014.

[17] G. Heydari, E. Thormann, M. Järn, E. Tyrode, and P. M. Claesson, "Hydrophobic surfaces: Topography effects on wetting by supercooled water and freezing delay," *Journal of Physical Chemistry C*, vol. 117, no. 42, pp. 21752–21762, 2013.

[18] H. H. Jellinek, "Liquid-like (transition) layer on ice," *Journal of Colloid And Interface Science*, vol. 25, no. 2, pp. 192–205, 1967.

[19] R. R. Gilpin, "A model of the "liquid-like" layer between ice and a substrate with applications to wire regelation and particle migration," *Journal of Colloid And Interface Science*, vol. 68, no. 2, pp. 235–251, 1979.

[20] S. Engemann, H. Reichert, H. Dosch, J. Bilgram, V. Honkimäki, and A. Snigirev, "Interfacial Melting of Ice in Contact with SiO_2," *Phys. Rev. Lett.*, vol. 92, p. 205701, 2004.

[21] K. Morishige, "Influence of Pore Wall Hydrophobicity on Freezing and Melting of Confined Water," *Journal of Physical Chemistry C*, vol. 122, no. 9, pp. 5013–5019, 2018.

[22] V. F. Petrenko, "Study of the surface of ice, ice/solid and ice/liquid interfaces with scanning force microscopy," *Journal of Physical Chemistry B*, vol. 101, no. 32, pp. 6276–6281, 1997.

[23] D. Chen, M. D. Gelenter, M. Hong, R. E. Cohen, and G. H. McKinley, "Icephobic surfaces induced by interfacial nonfrozen water," *ACS Applied Materials and Interfaces*, vol. 9, no. 4, pp. 4202–4214, 2017.

[24] C. Totland, S. Steinkopf, A. M. Blokhus, and W. Nerdal, "Water structure and dynamics at a silica surface: Pake doublets in 1H NMR spectra," *Langmuir*, vol. 27, no. 8, pp. 4690–4699, 2011.

[25] Q. Zeng and K. Li, "Quasi-liquid layer on ice and its effect on the confined freezing of porous materials," *Crystals*, vol. 9, no. 5, 2019.

[26] H. Chen, Y. Wu, H. Xia, Z. Zhang, and T. Yuan, "Anti-freezing asphalt concrete: ice-adhesion performance," *Journal of Materials Science*, vol. 53, no. 7, pp. 4781–4795, 2018.

[27] K. A. Emelyanenko, A. M. Emelyanenko, and L. B. Boinovich, "Water and ice adhesion to solid surfaces: Common and specific, the impact of temperature and surface wettability," *Coatings*, vol. 10, no. 7, 2020.

[28] C. Totland, R. T. Lewis, and W. Nerdal, "Long-Range Surface-Induced Water Structures and the Effect of 1-Butanol Studied by 1H Nuclear Magnetic Resonance," *Langmuir*, vol. 29, no. 35, pp. 11055–11061, 2013.

[29] V. M. Gun'ko, V. V. Turov, V. M. Bogatyrev, V. I. Zarko, R. Leboda, E. V. Goncharuk, A. A. Novza, A. V. Turov, and A. A. Chuiko, "Unusual properties of water at hydrophilic/hydrophobic interfaces," *Advances in Colloid and Interface Science*, vol. 118, no. 1-3, pp. 125–172, 2005.

[30] C. Totland, "Vannets struktur: En av vitenskapens store uløste gåter," *Naturen*, vol. 142, no. 05, pp. 206–211, 2018.

[31] P. Wiggins, "Life depends upon two kinds of water," *PLOS ONE*, vol. 3, no. 1, pp. 1–16, 2008.

[32] P. McConville and J. M. Pope, "1H NMR T2 relaxation in contact lens hydrogels as a probe of water mobility," *Polymer*, vol. 42, no. 8, pp. 3559–3568, 2001.

[33] K. Y. Law and H. Zhao, *Surface wetting: Characterization, contact angle, and fundamentals*. Springer, 2015.

[34] T. Young, "Iii. an essay on the cohesion of fluids," *Philosophical Transactions of the Royal Society of London*, vol. 95, pp. 65–87, 1805.

[35] T. Huhtamäki, X. Tian, J. T. Korhonen, and R. H. Ras, "Surface-wetting characterization using contact-angle measurements," *Nature Protocols*, vol. 13, no. 7, pp. 1521–1538, 2018.

[36] B. Krasovitski and A. Marmur, "Drops down the hill: Theoretical study of limiting contact angles and the hysteresis range on a tilted plate," *Langmuir*, vol. 21, no. 9, pp. 3881–3885, 2005.

[37] R. N. Wenzel, "Resistance of solid surfaces to wetting by water," *Industrial & Engineering Chemistry*, vol. 28, no. 8, pp. 988–994, 1936.

[38] A. B. D. Cassie and S. Baxter, "Wettability of porous surfaces," *Trans. Faraday Soc.*, vol. 40, pp. 546–551, 1944.

[39] C. Ishino and K. Okumura, "Wetting transitions on textured hydrophilic surfaces," *The European physical journal. E, Soft matter*, vol. 25, pp. 415–24, 05 2008.

[40] L. Wang, W. Kong, F. Wang, and H. Liu, "Temperature-gradient effects on heterogeneous ice nucleation from supercooled water," *AIP Advances*, vol. 9, no. 12, p. 125122, 2019.

[41] T. M. Schutzius, S. Jung, T. Maitra, P. Eberle, C. Antonini, C. Stamatopoulos, and D. Poulikakos, "Physics of icing and rational design of surfaces with extraordinary icephobicity," *Langmuir*, vol. 31, no. 17, pp. 4807–4821, 2015.

[42] N. H. Fletcher, "Size effect in heterogeneous nucleation," *The Journal of Chemical Physics*, vol. 29, no. 3, pp. 572–576, 1958.

[43] L. Ickes, A. Welti, C. Hoose, and U. Lohmanna, "Classical Nucleation Theory of homogeneous freezing of water: Thermodynamic and kinetic parameters," *Physical Chemistry Chemical Physics*, vol. 17, no. 8, pp. 5514–5537, 2015.

[44] J. Gilmour, *Microphysics of Clouds and Precipitation*, vol. 18. Springer, 1980.

[45] P. Irajizad, S. Nazifi, and H. Ghasemi, "Icephobic surfaces: Definition and figures of merit," *Advances in Colloid and Interface Science*, vol. 269, pp. 203–218, 2019.

[46] A. Amirfazli and C. Antonini, "Chapter 11 fundamentals of anti-icing surfaces," in *Non-wettable Surfaces: Theory, Preparation and Applications*, pp. 319–346, The Royal Society of Chemistry, 2017.

[47] X. Y. Liu, "Heterogeneous nucleation or homogeneous nucleation?," *Journal of Chemical Physics*, vol. 112, no. 22, pp. 9949–9955, 2000.

[48] J. M. Campbell, F. C. Meldrum, and H. K. Christenson, "Is ice nucleation from supercooled water insensitive to surface roughness?," *Journal of Physical Chemistry C*, vol. 119, no. 2, pp. 1164–1169, 2015.

[49] L. Lupi and V. Molinero, "Does hydrophilicity of carbon particles improve their ice nucleation ability?," *Journal of Physical Chemistry A*, vol. 118, no. 35, pp. 7330–7337, 2014.

[50] Y. Zhang, E. Anim-Danso, S. Bekele, and A. Dhinojwala, "Effect of Surface Energy on Freezing Temperature of Water," *ACS Applied Materials and Interfaces*, vol. 8, no. 27, pp. 17583–17590, 2016.

[51] M. Faraday, "On certain condations of freezing water," *Athenaeum*, no. 1181, pp. 640–641, 1850.

[52] W. Weyl, "Surface structures of water and some of its physical and chemical manifestations," *J.Colloid Sci.*, vol. 6, no. 5, pp. 389–405, 1851.

[53] K. Overloop and L. Vangerven, "Freezing Phenomena in Adsorbed Water as Studied by NMR," *Journal of Magnetic Resonance, Series A*, vol. 101, no. 2, pp. 179–187, 1993.

[54] H. Friebolin, *Basic One- and Two-Dimensional NMR Spectroscopy*, ch. 1, pp. 1–16. Weinheim: Wiley-VCH, 5th completely rev. and enl. ed., 2011.

[55] H. Günther, *NMR Spectroscopy: Basic Principles, Concepts, and Applications in Chemistry*, ch. 2, pp. 13–27. Weinheim: Wiley-VCH, 3rd., completely rev. and updated ed., 2013.

[56] R. R. Ernst and W. A. Anderson, "Application of fourier transform spectroscopy to magnetic resonance," *Review of Scientific Instruments*, vol. 37, no. 1, pp. 93–102, 1966.

[57] H. Friebolin, *Basic One- and Two-Dimensional NMR Spectroscopy*, ch. 7, pp. 167–170. Weinheim: Wiley-VCH, 5th completely rev. and enl. ed., 2011.

[58] H. Friebolin, *Basic One- and Two-Dimensional NMR Spectroscopy*, ch. 7, pp. 174–184. Weinheim: Wiley-VCH, 5th completely rev. and enl. ed., 2011.

[59] P. M. Walker, C. Balmer, S. Ablett, and R. A. Lerski, "A test material for tissue characterisation and system calibration in MRI," *Physics in Medicine and Biology*, vol. 34, no. 1, pp. 5–22, 1989.

[60] P. Check, "Pulsed Nuclear Magnetic Resonance: Spin Echoes," *MIT Department of Physics*, no. 3, pp. 1–14, 2017.

[61] H. Y. Carr and E. M. Purcell, "Effects of diffusion on free precession in nuclear magnetic resonance experiments," *Physical Review*, vol. 94, no. 3, pp. 630–638, 1954.

[62] H. Friebolin, *Basic One- and Two-Dimensional NMR Spectroscopy*, ch. 1, pp. 22–25. Weinheim: Wiley-VCH, 5th completely rev. and enl. ed., 2011.

[63] LibreTexts, "Chemical shift (shielding)." `https://chem.libretexts.org/Bookshelves/Physical_and_Theoretical_Chemistry_Textbook_Maps/Supplemental_Modules_(Physical_and_Theoretical_Chemistry)/Spectroscopy/Magnetic_Resonance_Spectroscopies/Nuclear_Magnetic_Resonance/NMR_-_Theory/NMR_Interactions/Chemical_Shift_(Shielding)`, 2022. Last accessed 06 June 2022.

[64] M. J. Duer, *Solid-State NMR Spectroscopy Principles and Applications*, ch. 1, pp. 1–72. John Wiley & Sons, Ltd, 2001.

[65] H. Günther, *NMR Spectroscopy: Basic Principles, Concepts, and Applications in Chemistry*, ch. 5, p. 117. Weinheim: Wiley-VCH, 3rd., completely rev. and updated ed., 2013.

[66] W. Schneider, H. Bernstein, and J. Pople, "Proton Magnetic Resonance Chemical Shift of Free (Gaseous) and Associated (Liquid) Hydride Molecules," *The Journal of Chemical Physics*, vol. 28, no. 4, pp. 601–607, 1958.

[67] J. C. Hlndman, "Proton resonance shift of water in the gas and liquid states," *The Journal of Chemical Physics*, vol. 44, no. 12, pp. 4582–4592, 1966.

[68] Y. Ishihara, A. Calderon, H. Watanabe, K. Okamoto, Y. Suzuki, K. Kuroda, and Y. Suzuki, "A precise and fast temperature mapping using water proton chemical shift," *Magnetic Resonance in Medicine*, vol. 34, no. 6, pp. 814–823, 1995.

[69] C. M. Widdifield and R. W. Schurko, "Understanding chemical shielding tensors using group theory, MO analysis, and modern density-functional theory," *Concepts in Magnetic Resonance Part A: Bridging Education and Research*, vol. 34, no. 2, pp. 91–123, 2009.

[70] F. Nardelli, S. Borsacchi, L. Calucci, E. Carignani, F. Martini, and M. Geppi, "Anisotropy and NMR spectroscopy," *Rendiconti Lincei*, vol. 31, no. 4, pp. 999–1010, 2020.

[71] H. Günther, *NMR Spectroscopy: Basic Principles, Concepts, and Applications in Chemistry*, ch. 3, pp. 29–35. Weinheim: Wiley-VCH, 3rd., completely rev. and updated ed., 2013.

[72] H. Günther, *NMR Spectroscopy: Basic Principles, Concepts, and Applications in Chemistry*, ch. 14, pp. 570–572. Weinheim: Wiley-VCH, 3rd., completely rev. and updated ed., 2013.

[73] S. Ashbrook, "The Power of Solid-State NMR." `http://www.tcm.phy.cam.ac.uk/castep/oxford/power_nmr.pdf`, 2009. Last accessed 06 June 2022.

[74] Y. Liao, "Alpha (α) - Alumina (sapphire)- Practical Electron Microscopy and Database." `https://www.globalsino.com/EM/page2591.html`, 2007. Last accessed 19 June 2022.

[75] J. C. Guerrero, "NMR spectrometers at UiB." `https://www.uib.no/en/rg/nmrspectro/94587/nmr-spektrometers-uib`, 09.06.2022. Last accessed 19 June 2022.

[76] N. Rankin, D. Preiss, P. Welsh, K. Burgess, S. Nelson, D. Lawlor, and N. Sattar, "The emergence of proton nuclear magnetic resonance metabolomics in the cardiovascular arena as viewed from a clinical perspective," *Atherosclerosis*, vol. 237, p. 287–300, 11 2014.

[77] T. Parella, *Pulse Program Catalogue: I. 1D & 3D NMR Experiments*. Bruker Biospinn.

[78] D. Instruments, "Schematic assembly of the oca models." `https://www.dataphysics-instruments.com/products/oca/`, 2022. Last accessed 16 January 2022.

[79] T. Huhtamäki, X. Tian, J. T. Korhonen, and R. H. A. Ras, "Surface-wetting characterization using contact-angle measurements," *Nature Protocols*, vol. 13, no. 7, pp. 1521–1538, 2018.

[80] S. S. Ray, "4 - techniques for characterizing the structure and properties of polymer nanocomposites," in *Environmentally Friendly Polymer Nanocomposites* (S. S. Ray, ed.), Woodhead Publishing Series in Composites Science and Engineering, pp. 74–88, Woodhead Publishing, 2013.

[81] B. Voigtländer, *Atomic force microscopy designs*. Springer, 2019.

[82] D. Zhang, Y. Wang, and Y. Gan, "Characterization of critically cleaned sapphire single-crystal substrates by atomic force microscopy, XPS and contact angle measurements," *Applied Surface Science*, vol. 274, pp. 405–417, 2013.

[83] V. Pishchik, L. A. Lytvynov, and E. R. Dobrovinskaya, *Sapphire*. Springer New York, 1 ed., 2009.

[84] C. He, T. Liu, L. Tian, Y. Xiao, S. Yuan, and Q. Wang, "Effect of crystal orientation on droplet wetting behavior on single-crystal Al2O3substrates: An experimental study," *Physics of Fluids*, vol. 32, no. 12, 2020.

[85] L. Cao, X. Zhang, J. Yuan, L. Guo, T. Hong, W. Hang, and Y. Ma, "Study on the influence of sapphire crystal orientation on its chemical mechanical polishing," *Applied Sciences (Switzerland)*, vol. 10, no. 22, pp. 1–10, 2020.

[86] I. P. Løvås, "Anti-Icing Properties of Diamond Surfaces," Master's thesis, University of Bergen, 2022.

[87] V. M. Gun'ko and V. V. Turov, "Structure of hydrogen bonds and 1H NMR spectra of water at the interface of oxides," *Langmuir*, vol. 15, no. 19, pp. 6405–6415, 1999.

[88] J. L. Perez-Diaz, M. A. Alvarez-Valenzuela, J. Sanchez-Garcia-Casarrubios, and S. Jimenez-Lopez, "Ice Surface Entropy Induction by Humidity or How Humidity Prompts Freezing," *Journal of Colloid and Interface Science*, vol. 3, pp. 1–5, 2015.

[89] S. Jung, M. K. Tiwari, N. V. Doan, and D. Poulikakos, "Mechanism of supercooled droplet freezing on surfaces," *Nature Communications*, vol. 3, 2012.

[90] M. Mezger, S. Schöder, H. Reichert, H. Schröder, J. Okasinski, V. Honkimäki, J. Ralston, J. Bilgram, R. Roth, and H. Dosch, "Water and ice in contact with octadecyltrichlorosilane functionalized surfaces: A high resolution x-ray reflectivity study," *Journal of Chemical Physics*, vol. 128, no. 24, 2008.

[91] G. H. Findenegg, S. Jähnert, D. Akcakayiran, and A. Schreiber, "Freezing and melting of water confined in silica nanopores," *ChemPhysChem*, vol. 9, no. 18, pp. 2651–2659, 2008.

[92] J. F. D. Liljeblad, I. Furó, and E. C. Tyrode, "The premolten layer of ice next to a hydrophilic solid surface: correlating adhesion with molecular properties," *Physical Chemistry Chemical Physics*, vol. 19, no. 1, pp. 305–317, 2017.

[93] G. Heydari, E. Thormann, M. Järn, E. Tyrode, and P. M. Claesson, "Hydrophobic surfaces: Topography effects on wetting by supercooled water and freezing delay, (Suppl. Mat.)," *Journal of Physical Chemistry C*, vol. 117, no. 42, pp. 21752–21762, 2013.

Appendix A

Background Results

A.1 Background Noise

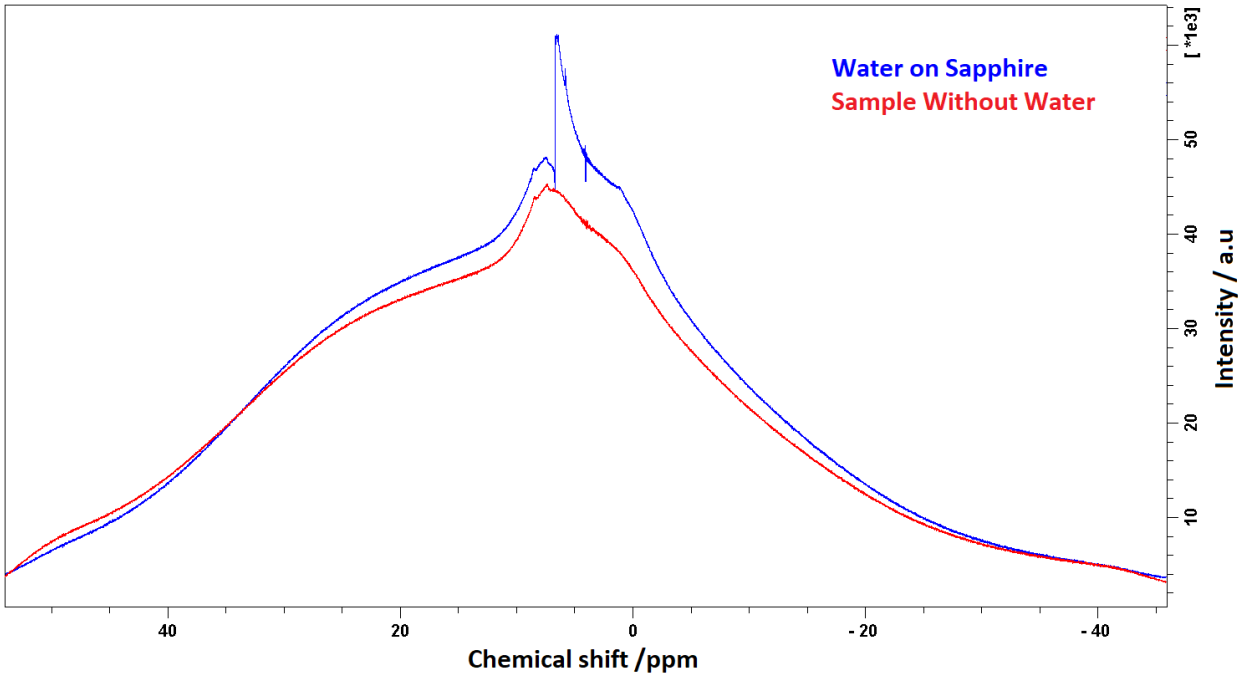

Figure A.1: Two one-pulse NMR-spectra; One with water on smooth sapphire (blue) and the other is a spectrum of sample holder and sapphire plates without any water (red), show a substantial background signal. These spectra are recorded with different parameters (ns=1, rg=4 and TD=9994) than the others presented in this thesis (listed in Table 4.1). Thus the intensity is not comparable with the other spectra presented.

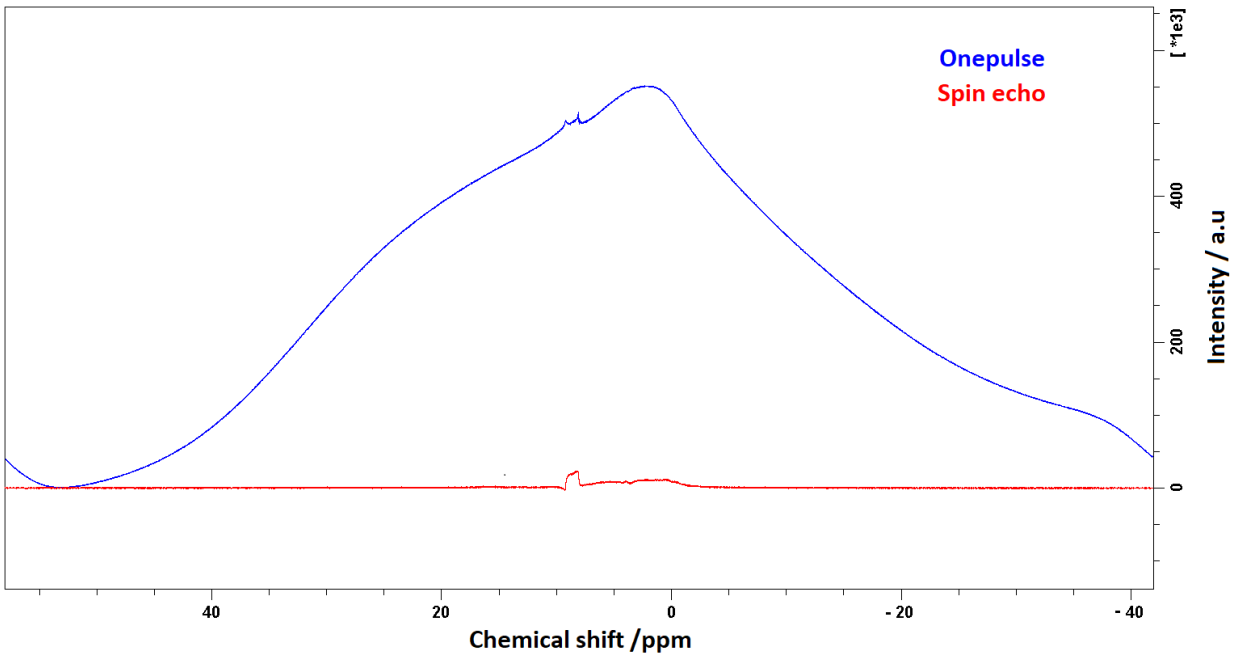

Figure A.2: Comparison of two background spectra recorded with one pulse (blue line) and spin echo (red line). The one pulse spectrum is recorded with rg=3.2 which differs from spin echo spectrum recorded with rg=203 (4.1). This affects the intensity of the spectrum, which is why the red line scales down to 0.6. Hence, this is not directly comparable but provides an impression of the difference.

A.1.1 Drift

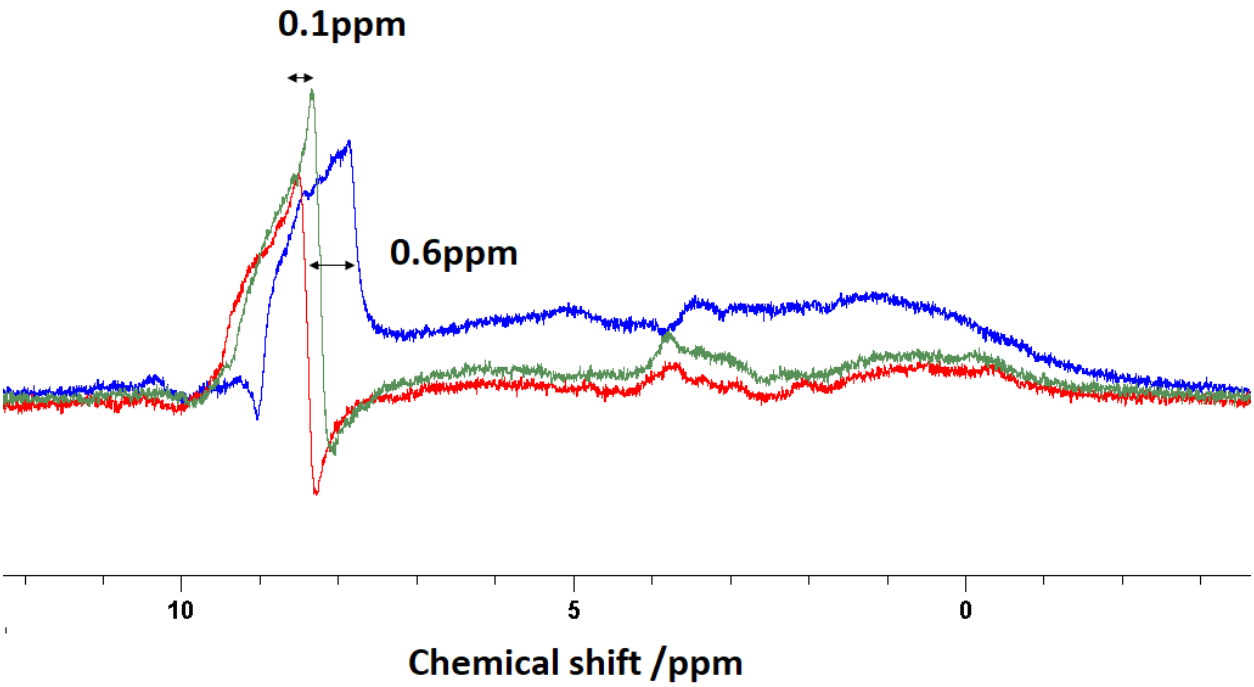

Figure A.3: Showing how changes in drift over time affect the chemical shift and phase. Blue is recorded one month before red, followed by green a week later. (Note that blue had slightly more parafilm than red and green).

A.2 Recorded Data Overview

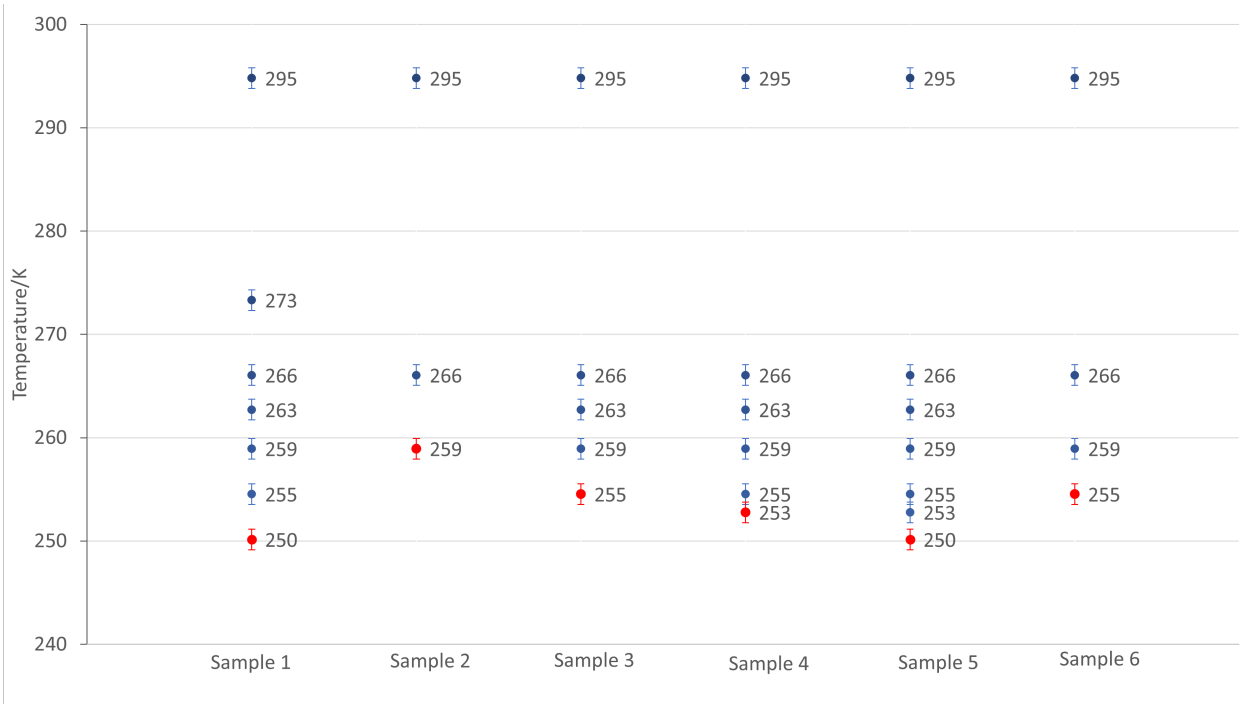

(a) Smooth sapphire

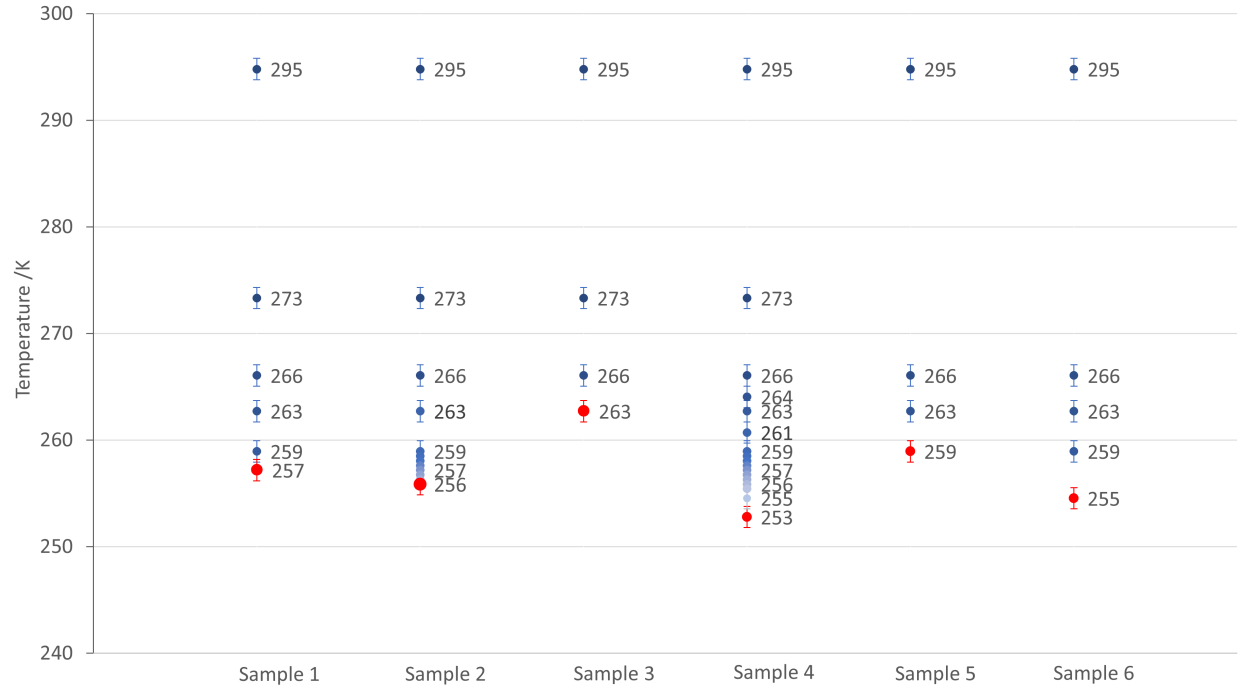

(b) Rough sapphire

Figure A.4: Figure shows an overview of the freezing points (red) and exact temperature steps (black) for all the recorded NMR-spectra per sample and surface type.

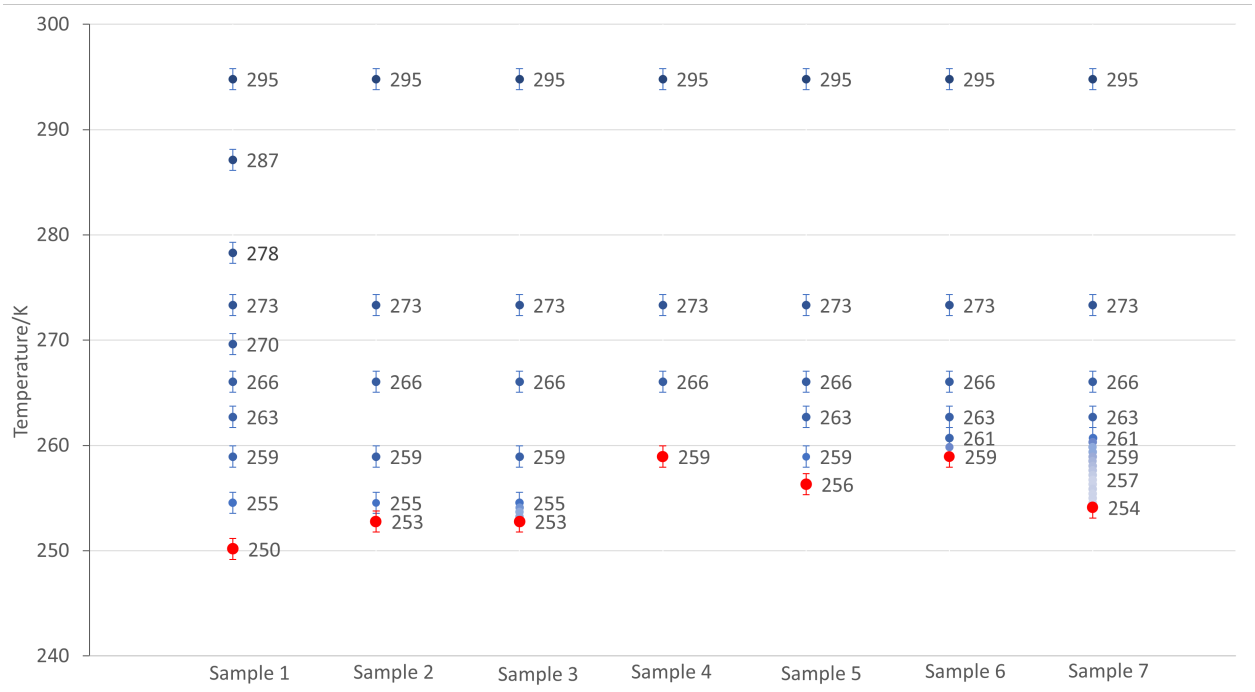

(c) Smooth silica

Figure A.4: Figure shows an overview of the freezing points (red) and exact temperature steps (black) for all the recorded NMR-spectra per sample and surface type.

A.3 Extra material - Curvature analysis

Table A.1: Data overview of scale length between each pixel of the AFM images presented in Figure 5.1 (a-b), 5.2 (a-b) and 5.3 (a-b)

	Rough sapphire		Smooth sapphire		Smooth silica	
	LW	WE	LW	WE	LW	WE
Scan size(nm)	20000	20000	5000	5000	5000	2500
Pixel	256	256	512	256	256	256
Fraction (nm)	78	78	10	20	20	10

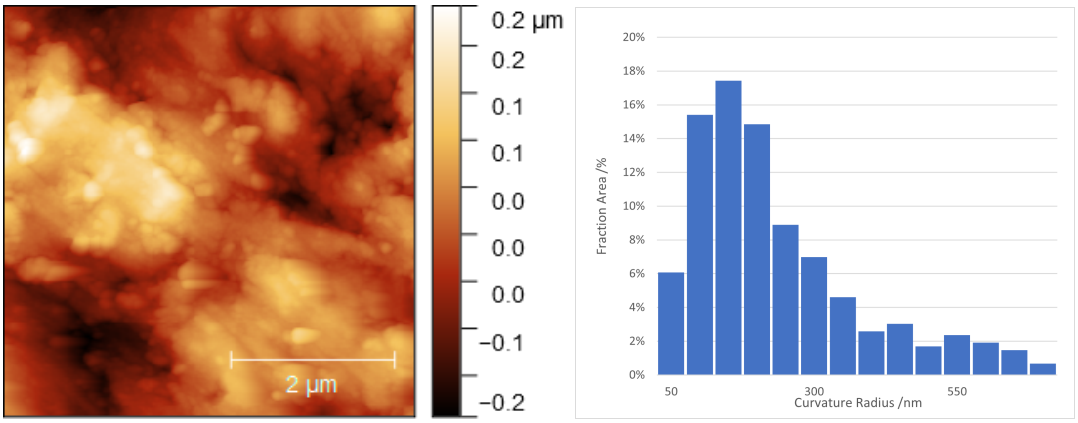

(a) AFM-image (LW) (b) Curvature radius (LW)

Figure A.5: Rough sapphire (LW): (a) show topography 5 µm AFM images of loosely washed (LW) and washed and etched (WE) rough sapphire. (b) show the distribution of curvature radius for pits is found in by curvature analysis. The fraction area is the percentage of measurements with positive curvature radius which is 17% in this case

Table A.2: Listed below is information about the AFM image and curvature distribution belonging to Figure A.5

Scale			Curv. distribution (%)			$R < 10r_{c,263K}$	
scan size (nm)	Pixel	fraction (nm)	pos.	neg.	neu.	% pos.	% tot.
5000	256	20	17	4	79	4.9	0.8

A.4 Raw Data Freezing Temperature

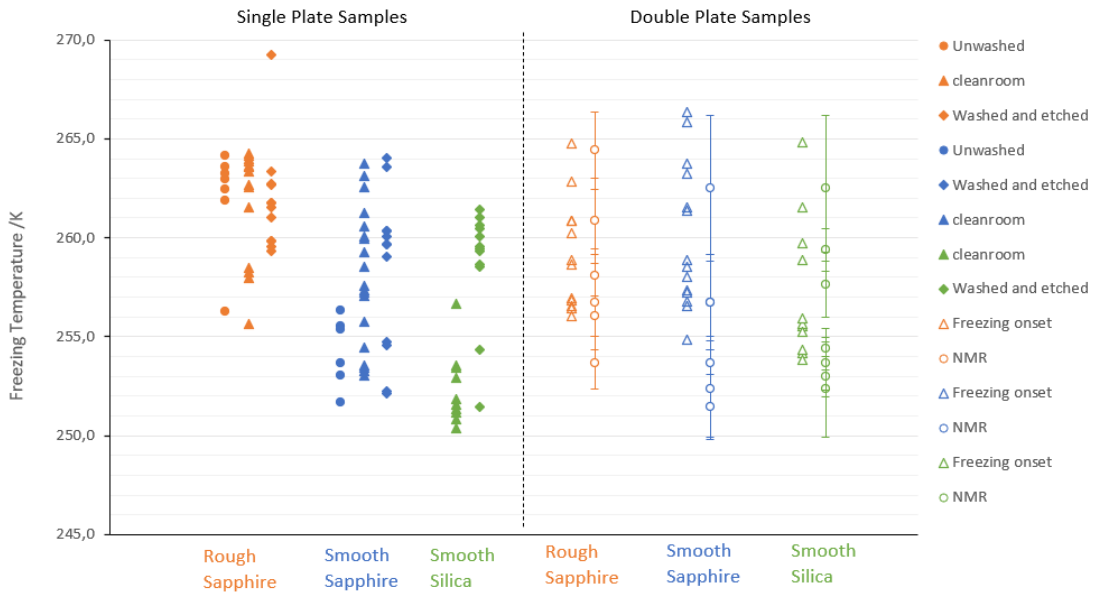

Figure A.6: Scattered plot of all freezing temperature measurements. The uncertainty bars for the NMR measurements are calculated by Equation B.6 (propagation of uncertainties) and is based on the uncertainties from temperature calibrations (see section 4.3.6) and the temperature range between freezing spectra and the spectra before (see Figure A.4)

A.5 Reproducibility of NMR spectra

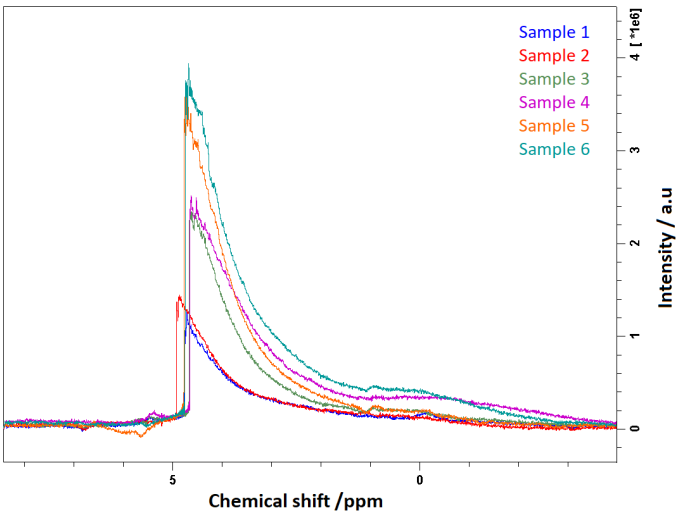

(a) Smooth sapphire

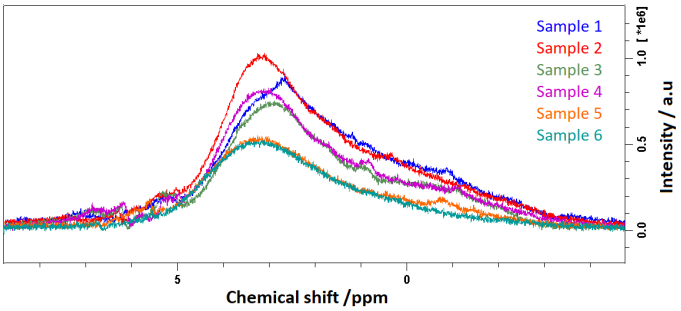

(b) Rough Sapphire

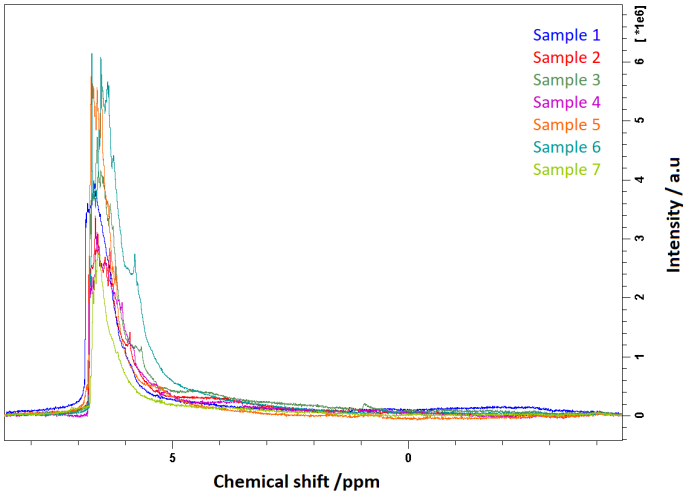

(c) Smooth silica

Figure A.7: Comparison of spectra recorded at 295K ± 1K for all the samples. Smooth Silica sample 6, is scaled to 0.7 of its value.

A.6 All Freezing measurements

Smooth Sapphire

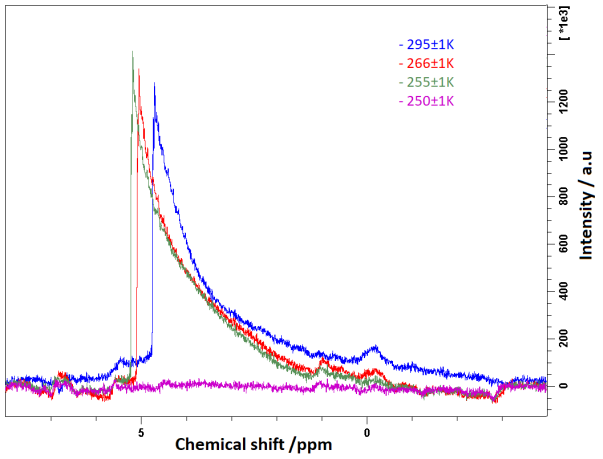

(a) Sample 1

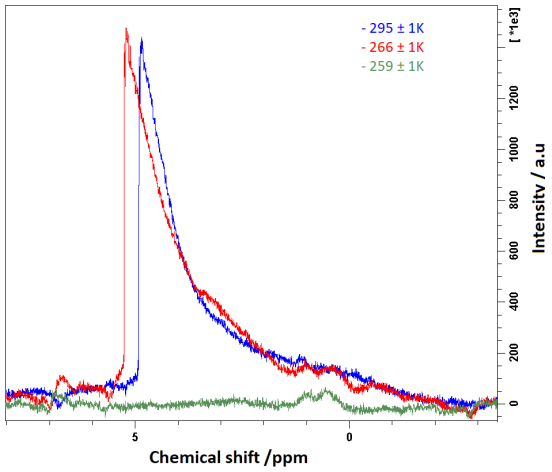

(b) Sample 2

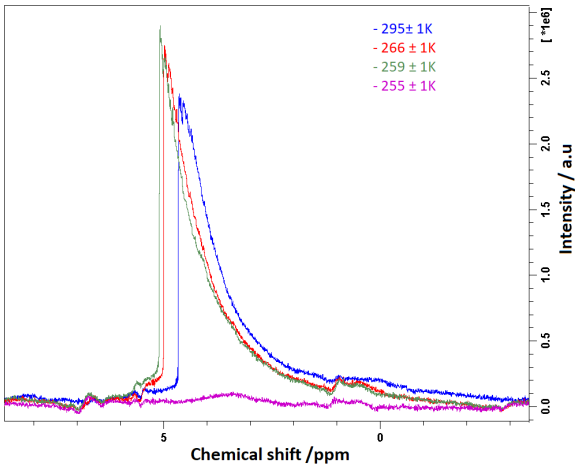

(c) Sample 3

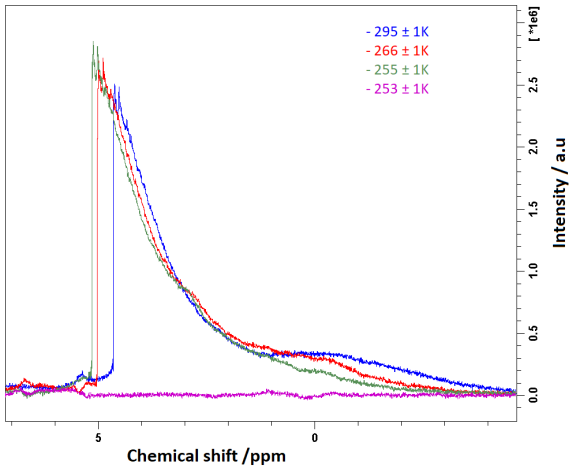

(d) Sample 4

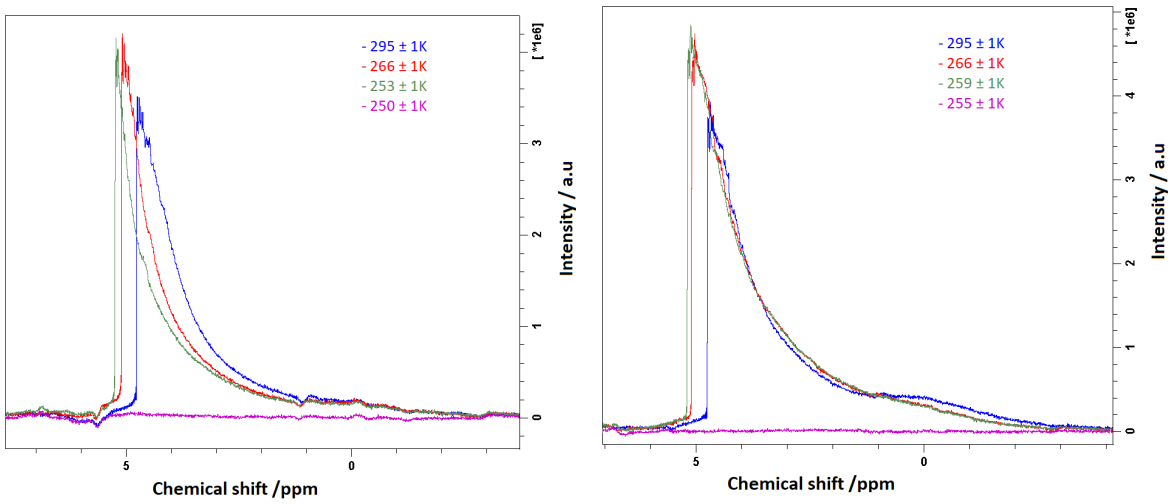

(e) Sample 5 (f) Sample 6

Figure A.8: Effect of temperature variation for 1H-NMR spectra of interfacial water until freezing for six smooth sapphire samples (a)-(f). The plot consist of four selected temperature points, where green is used for the last spectra recorded before freezing and purple for spectra after freezing.

Rough Sapphire

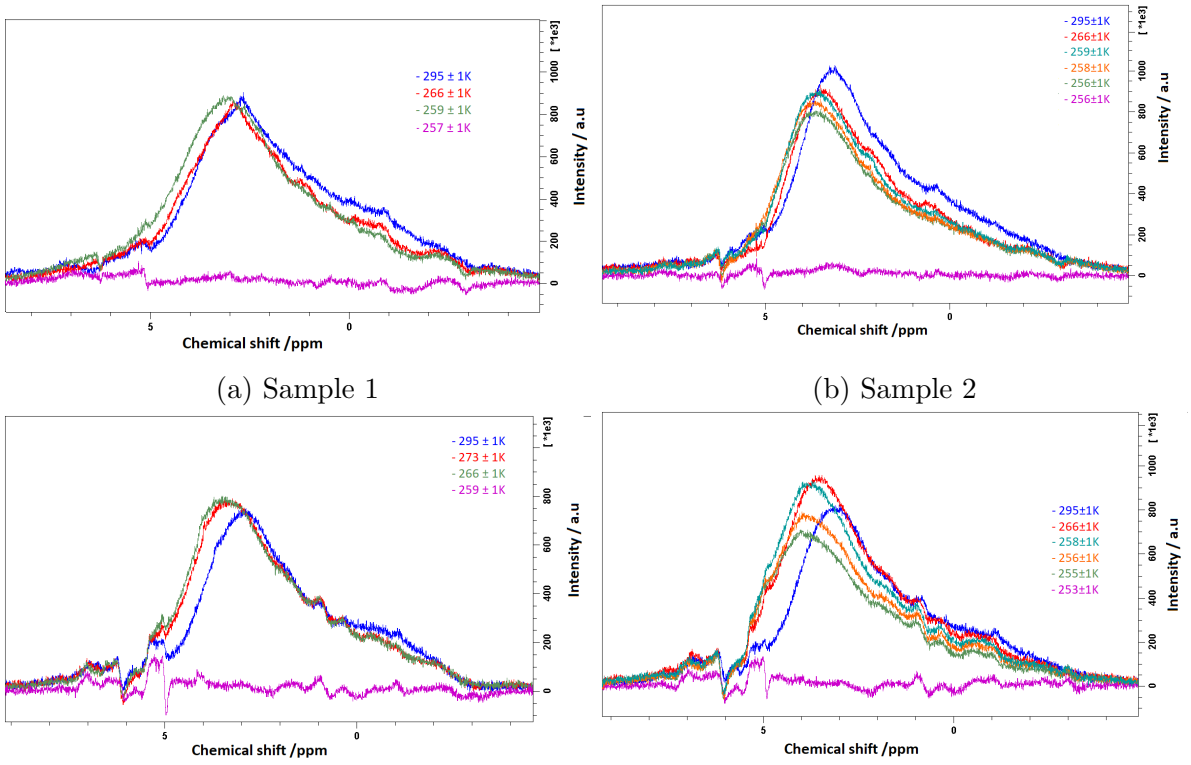

(a) Sample 1 (b) Sample 2

(c) Sample 3 (d) Sample 4

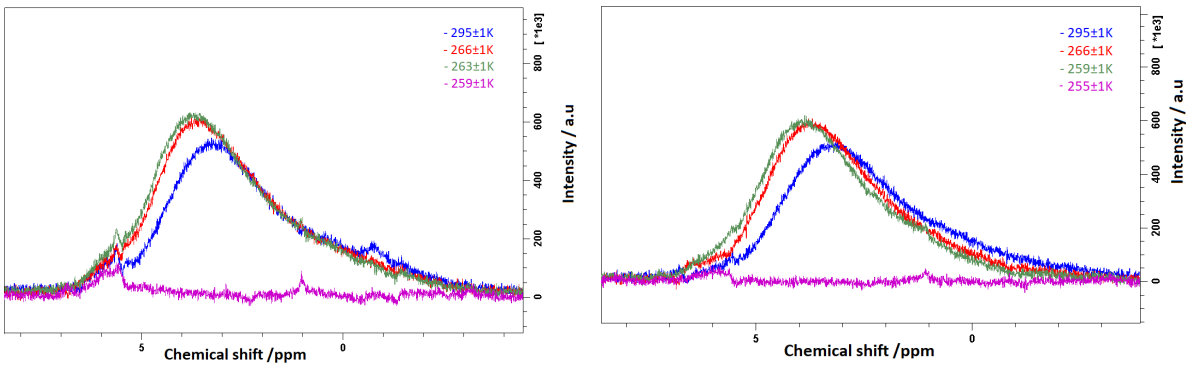

(e) Sample 5

(f) Sample 6

Figure A.9: Effect of temperature variation for 1H-NMR spectra of interfacial water until freezing for six rough sapphire samples (a)-(f). The plot consist of four selected temperature points, where green is used for the last spectra recorded before freezing and purple for spectra after freezing.

Smooth silica

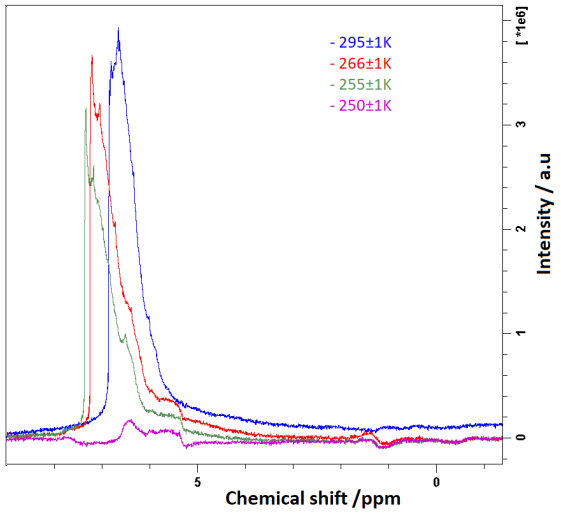

(a) Sample 1

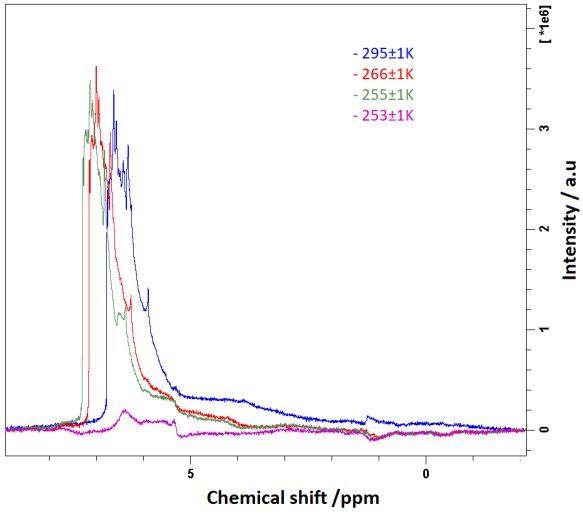

(b) Sample 2

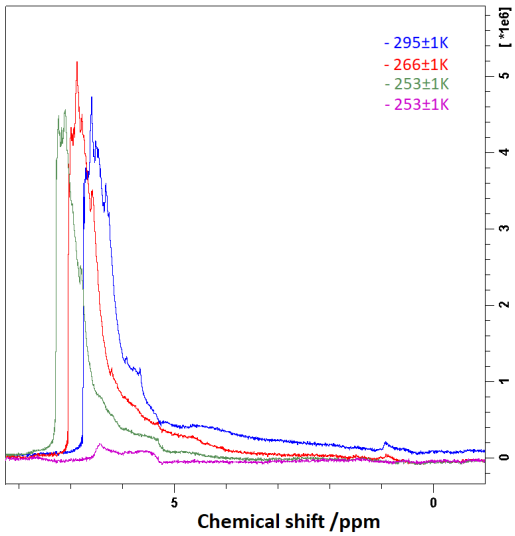

(c) Sample 3

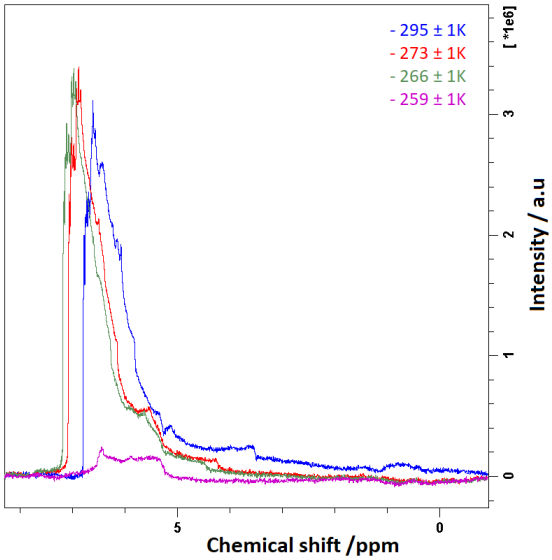

(d) Sample 4

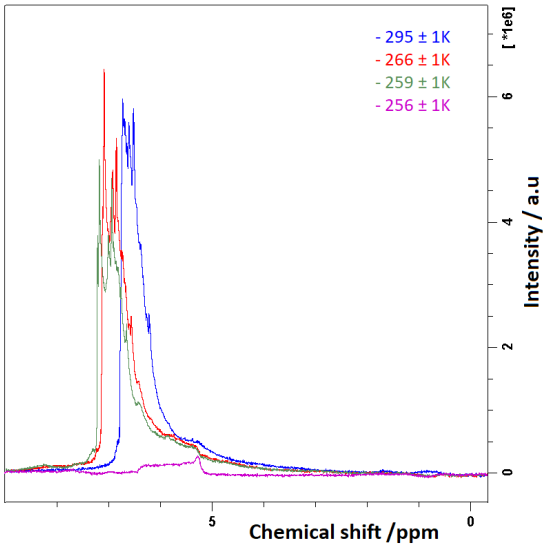

(e) Sample 5

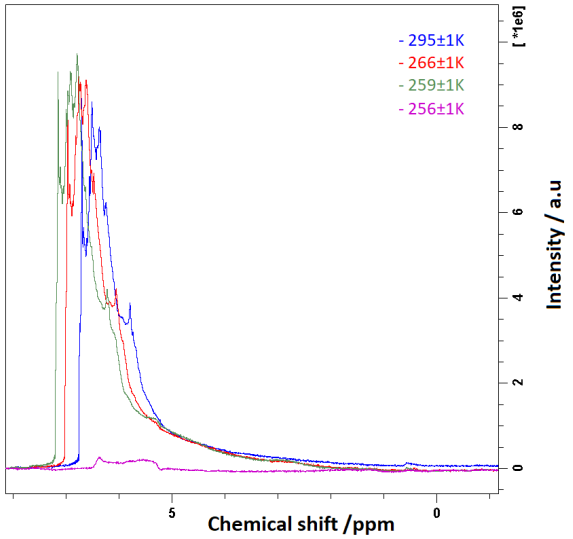

(f) Sample 6

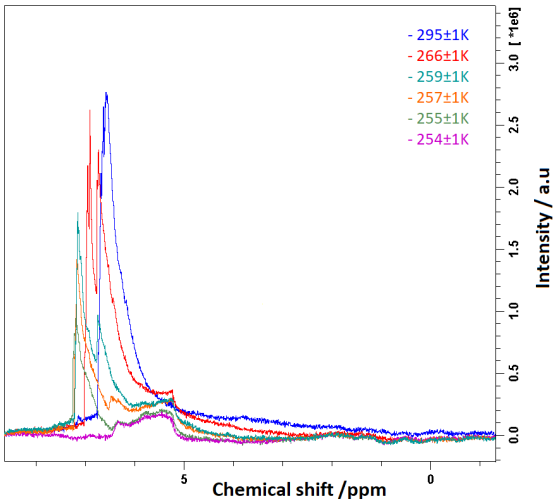

(g) Sample 7

Figure A.10: Effect of temperature variation for 1H-NMR spectra of interfacial water until freezing for six smooth silica samples (a)-(f). The plot consist of four selected temperature points, where green is used for the last spectra recorded before freezing and purple for spectra after freezing.

Appendix B

Image Processing and Calculations

B.1 Processing

B.1.1 AFM-results

AFM image processing

The AFM images used in this thesis (see Figure 5.1, 5.2, 5.3). have been processed in the Gwwyddion software. All images have been cut and levelled by plane, and the mean values are used as zero values. For the smooth sapphire and silica, additional processes of images polynomial background subtracting (2 degrees) and/or baseline correction (align rows) have been utilized.

Statistical analysis

RMS values are determined by the statistical Quantities tool, and one-dimensional roughness parameters functions are used for determining the high and low frequency components. Curvature radius is found using two functions: Mark by segmentation (with barrier level:100) and grain distribution, which is used to collect and export data for curvature 1 (κ_1) curvature 2 (κ_2). Curvature Radius is found as $\frac{1}{\kappa_1+\kappa_2}$ and plotted in histograms.

B.1.2 NMR-spectra processing

Phasing

A Fourier transformation must be done to process the FID signal into a spectrum. This is executed by typing the command "FT" in Topspin, followed by phase adjustment with the command "APK" and an additional manual phase correction where needed to secure a levelled baseline and symmetry of peak.

Calibrating Chemical Shift Axis

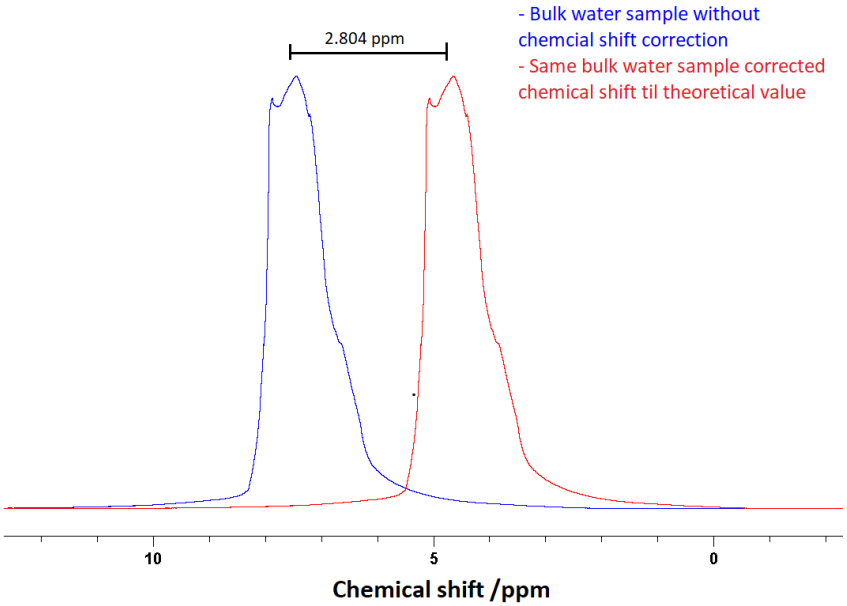

Figure B.1: Calibration of water peak as a reference

As bulk water has a known theoretical chemical shift value of 4.63 ppm at 295 K (relative to TMS), it is used as a reference for calibration of the x-axis. The bulk water sample used for calibration had the same parameters and shim as the interfacial water spectra. The difference between the experimentally found and the theoretical chemical shift is then used to calibrate all the samples.

Background Subtraction

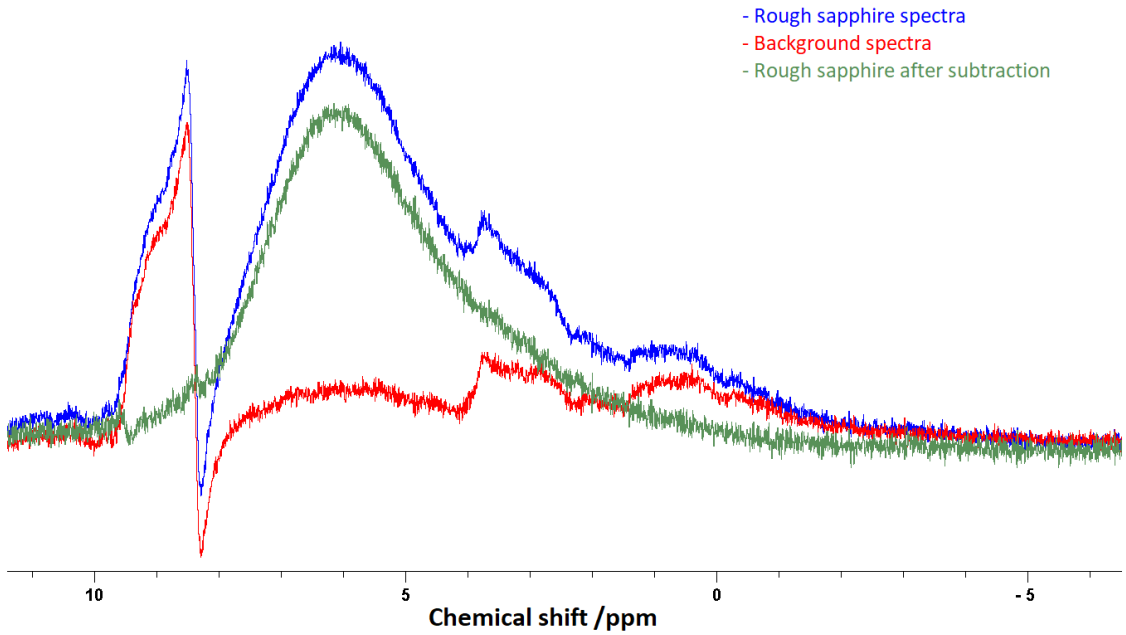

Figure B.2: Before background noise subtraction (blue line), background spectrum (red line) and after subtraction (green line) indicate the water peak

The signal assigned as background noise in the recorded water on double plate samples was removed by subtracting a reference spectrum of background noise using the subtraction functionality in TopSpin. Figure B.2 shows an example of this. For accuracy, every reference spectrum is adjusted by chemical shift and phase correction so that the signals lay as direct upon each other as possible to prevent artefacts.

B.2 Determination of Chemical Shift and Inaccuracy

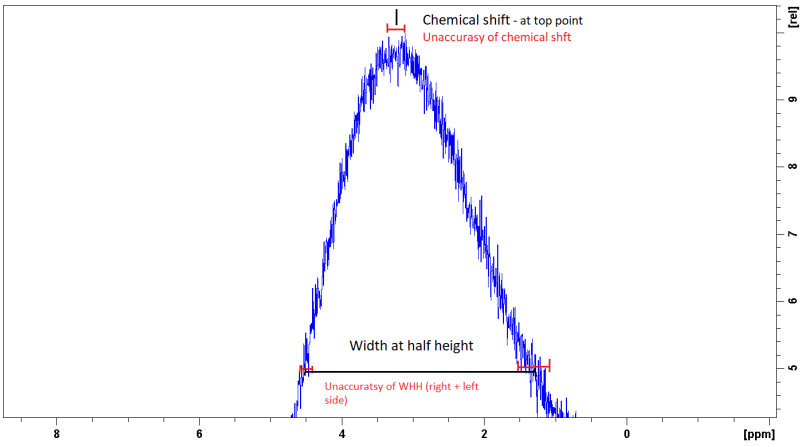

(a) Rough Sapphire

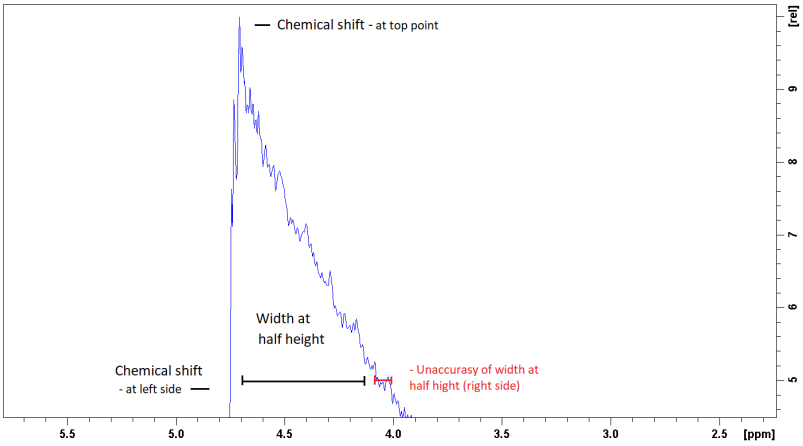

(b) Smooth Sapphire

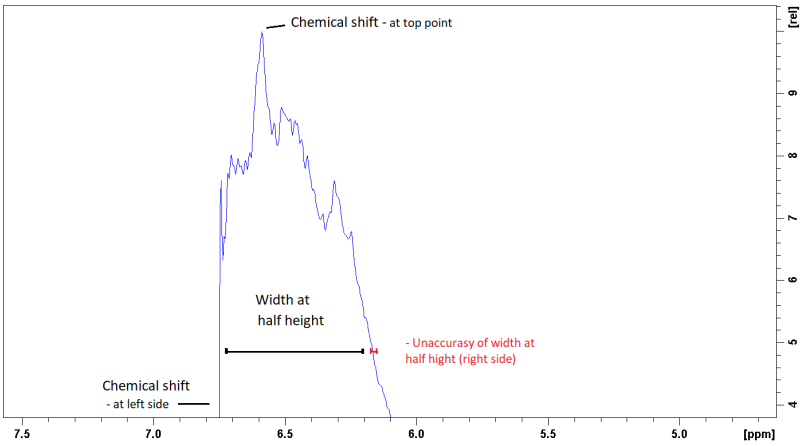

(c) Smooth silica

Figure B.3: Illustrations of how the chemical shift value is determined (measured at the top point and left sideline) and width at half height (WHH), with uncertainties. Chemical shift (ppm) on x-axis, and relative intensity (a.u) on y-axis.

The determination of chemical shift, width at half height (WHH) and accuracy is done by a manual reading of values, shown in Figure B.3. This process is performed for all the spectra after phasing, chemical shift calibration and noise subtraction to avoid potential impact on the chemical shift values. The width at half height is the difference in chemical shift at the half height of the peak, as shown in the figure. The chemical shift is generally determined by reading the value of the spectrum at the top of the peak. However, as these peaks are extra wide, differing from fine structures, alternative methods have been used to determine these values. For the spectra of smooth and rough sapphire at room temperature (295K), the chemical shift is read at the top point. However, as the peaks for the rough sapphire samples are relatively broad, the middle point of the broad peak has been used to determine chemical shift. The smooth silica samples have significant fine structure variations, making it hard to predict the exact peak, as seen in Figure B.3b. Therefore the chemical shift is read as the middle point of the WHH for the silica samples.

In the plot of observed changes in chemical shifts with temperature dependence (Figure 5.21,5.19 and 5.20) the top point for rough sapphire is still used to read the chemical shift. However, for smooth sapphire and silica, the left side straight peak (interfacial water) are used to determine the chemical values, as seen in Figure B.3. This method makes it easier and more accurate to compare the relative change in chemical shift for each temperature, excluding other possible effects including variations in fine structure with temperature change.

B.3 Calculations

B.3.1 Statistics

Statistical formulas used in this thesis are listed below:

Arithmetic mean value:

$$\overline{x} = \frac{1}{n}\sum_{i=1}^{n} x_i \tag{B.1}$$

Here, n = number of measurements and x_i is the measurement points.

Weighted mean value:

$$\overline{x}_w = \frac{\sum_{i=1}^{n} w_i x_i}{\sum_{i=1}^{n} w_i} \tag{B.2}$$

Here, n is number of measurements, x_i is the measurement points and the weights w_i are the reciprocal squares of the corresponding uncertainties:

$$w_i = \frac{1}{\sigma^2} \tag{B.3}$$

Uncertainty of weighted mean:

$$\sigma_{x_w} = \frac{1}{\sqrt{\sum_{i=1}^{n} w_i}} \tag{B.4}$$

Here σ_{x_w} is the uncertainty of the weighted mean $\overline{x}_w$, n is the number of measurements and w_i the reciprocal squares of the corresponding uncertainties.

Weighted standard deviation:

$$sd_w = \sqrt{\frac{\sum_{i=1}^{n} w_i(x_i - x_w)^2}{\frac{M-1}{M}\sum_{i=1}^{n} w_i}} \tag{B.5}$$

Here sd_w is the weighted standard deviation, w_i is the weights, M is the number of non-zero weights, $\overline{x_w}$ is the weighted mean, n is the number of measurements

Propagation of uncertainties regarding addition/subtraction

$$\delta z = \sqrt{(\delta x)^2 + (\delta y)^2} \tag{B.6}$$

Here, δz is the propagation of uncertainties, δx and δy is the uncertainties of x and y, respectively.

Standard deviation

$$\sigma = \sqrt{\frac{1}{n}\sum_{i=1}^{n} x_i} \tag{B.7}$$

Here, σ is the standard deviation, n = number of measurements and x_i is the measurement points.

Standard deviation mean value:

$$\sigma_{mean} = \frac{\sigma}{\sqrt{n}} \tag{B.8}$$

Here σ_{mean} is the standard deviation mean value, σ is standard deviation and n is the number of measurements

Linear Regression analysis

Linear Regression line is given by the formula:

$$y = mx + b \tag{B.9}$$

Here, m is the slope, b is a contactant/intercept. x is the explanatory variable, and y is the dependent variable. Slope m is given by:

$$m = \frac{\sum_{i=1}^{n}(x_i - \overline{x})(y_i - \overline{y})}{\sum_{i=1}^{n}(x_i - \overline{x})} \tag{B.10}$$

Here x_i and y_i is the measuring points for n measurments and $\overline{x}$ and $\overline{y}$ represents the mean of the values. Constant b on the trendline is calculated by:

$$b = \overline{y} - m\overline{x} \tag{B.11}$$

Goodness of fit measurements is calculated by R-squared:

$$R^2 = 1 - \frac{\sum_{i=1}^{n}(\hat{y}_i - \overline{y})^2}{\sum_{i=1}^{n}(y_i - \overline{y})^2} \tag{B.12}$$

$\hat{y}$ represent a the point on the trend-line, $\overline{y}$ represent the mean of all the values and y_i is the measuring points.

Roughness Root Mean Square

$$R_{RMS} = \sqrt{\frac{1}{N}\sum_{i=1}^{N}(h_i(x,y) - \overline{h})^2} \tag{B.13}$$

Here N is the total number of pixels in the AFM image and $\overline{h}$ is the average height of the surface.

B.3.2 Critical Radius of Ice-embryo

The calculation of critical radius is done using Equation 2.9 with necessary values calculated in the equations below, results of calculations are listed in Table B.1

Interfacial tension γ_{IW} between supercooled water and ice is given as [93]:

$$\gamma_{IW} = 28.0 + 0.25(T - T_m) \tag{B.14}$$

Here, $T_m = 273.15K$ is the ice melting point at 1 atm and T is the super cooling temperature.

ΔG_v is determined using the Gibbs-Helmholtz equation:

$$\Delta G_v = \Delta H_v \frac{T_m - T}{T_m} \tag{B.15}$$

Where the volumetric enthalpy ΔH_v is given as:

$$\Delta H_v = \frac{\Delta H_m + \int_{T_m}^{T}(C_{pi} - C_{pw})dT}{v} \tag{B.16}$$

Here, $\Delta H_m = -6000 Jmol^{-1}$ [93] is the molar enthalpy of fusion at the T_m, $v \approx 1.8 \cdot 10^{-5} m^3 mol^{-1}$ is the water molar volume and the heat capacities of ice and water at T are C_{pi} and C_{pw} given as [93]:

$$\begin{aligned}
&C_{pi} = 37.0 + 0.312(T - T_m)\\
&C_{pw} = 75.4\sum_{n=0}^{4} a_n (T - T_m)^n\\
&a_0 = 1.000938, a_1 = -2.7052 \cdot 10^{-3}, a_2 = -2.3235 \cdot 10^{-5},\\
&a_3 = 4.3778 \cdot 10^{-6}, a_4 = 2.7136 \cdot 10^{-7}
\end{aligned} \tag{B.17}$$

Table B.1: Critical radius at given temperatures

Temperature (K)	263	253
Critical radius (nm)	4.5	2.2